

**MODELING OF MICROSTRUCTURAL EVOLUTIONS IN
MACHINING OF DUAL PHASE ALLOYS**

A Dissertation
Presented to
The Academic Faculty

by

Seyed Ali Tabei

In Partial Fulfillment
of the Requirements for the Degree
Doctor of Philosophy in the
George W. Woodruff School of Mechanical Engineering

Georgia Institute of Technology
May 2015

Copyright© 2015 by Seyed Ali Tabei

MODELING OF MICROSTRUCTURAL EVOLUTIONS IN MACHINING OF DUAL PHASE ALLOYS

Approved by:

Dr. Steven Y. Liang, Co-Advisor
School of Mechanical Engineering
Georgia Institute of Technology

Dr. Antonia Antoniou
School of Mechanical Engineering
Georgia Institute of Technology

Dr. Karl I. Jacob
School of Mechanical Engineering
Georgia Institute of Technology

Dr. Hamid Garmestani, Co-Advisor
School of Materials Science and
Engineering
Georgia Institute of Technology

Dr. Saïd Ahzi
School of Materials Science and
Engineering
Georgia Institute of Technology

Dr. Guillermo Goldsztein
School of Mathematics
Georgia Institute of Technology

Date Approved: March 9, 2015

*To my dear wife, **Razieh** and my parents, **Mousa** and **Zohreh**,
for their endless love, support, encouragement and sacrifices*

ACKNOWLEDGEMENTS

I express my deep thankfulness to my advisors, Dr. Hamid Garmestani and Dr. Steven Y. Liang; for their guidance, support and teachings. This dissertation would have not been feasible without their directions and leadership.

Also, I would like to thank my other committee members, Dr. Saïd Ahzi, Dr. Antonia Antoniou, Dr. Karl I. Jacob and Dr. Guillermo Goldsztein for their valuable inputs and feedbacks to this dissertation.

I deeply appreciate Dr. Dongsheng Li, for his sincere helps and fruitful discussions during all my Ph.D. years. Dr. Guozheng Quan is also appreciated for his assistance and cooperation in several steps of this dissertation. Furthermore, I thank David Tavakoli, John Ho and Jordan Weaver for their valued helps in many aspects of the project. I am very grateful to my friend, Vahid Tari for his great assistance in texture evolution modeling.

The G.W. Woodruff school machine shop engineers, Mr. Steven Sheffield and Mr. Brandon Royal, are deeply appreciated for their wonderful cooperation and flexibility in helping me with machining. Mr. O. Fergani is appreciated for procurement of the raw materials.

I am very grateful to G.W. Woodruff School's faculty and staff, especially Dr. Wayne Whiteman and Ms. Glenda Johnson for their flexibility, friendliness, understanding and cooperations during the past year.

I should express my thankfulness to my beloved wife Razieh, who made this journey possible by her never-ending love, support and encouragement. I also deeply

thank my parents, for their enormous sacrifices, support and love. I sincerely thank my friends for all the sweet and memorable moments I spent with them during the past years.

Finally, I deeply thank the Boeing Company for financial sponsorship of the project through their University Strategic Partnership Program.

Table of Contents

ACKNOWLEDGEMENTS	iv
LIST OF TABLES.....	viii
LIST OF FIGURES.....	ix
SUMMARY	xvii
1. INTRODUCTION.....	1
1.1 Motivation	1
1.2 Objectives and scope	5
1.3 Organization of the dissertation.....	7
2. BACKGROUND AND LITERATURE REVIEW.....	10
2-1 Microstructural phenomena in metals	10
2-2 Microstructural phenomena in aluminum alloy 707	17
2-2-1 General characteristics of AA 7075	17
2-2-2 Recovery and recrystallization in AA7075.....	19
2-2-3 Texture evolution in AA7075	22
2-2-4 Heat treatment and precipitation hardening in AA7075	22
2-3 Summary	25
3. THERMO-MECHANICS OF CUTTING	27
3-1 Forces in Orthogonal Cutting	27
3-2 Temperature rise in orthogonal cutting.....	32
3-3 Turning.....	34
3-4 Temperature rise in turning.....	38
3-5 Experimental plan	40
3-6 Finite element analysis	44
3-7 Summary	46
4. CRYSTALLOGRAPHIC TEXTURE EVOLUTION	48

4-1 Crystallographic Texture and Anisotropy	48
4-2 Representation of texture	50
4-3 Modeling of texture evolution	62
4-4 Micro-texture evolution in machining of AA7075.....	66
4-5 Conclusions and Future Trends.....	82
5. RECRYSTALLIZATION AND GRAIN GROWTH	85
5-1 Grain evolution phenomena in machining of AA7075.....	85
5-2 Kinetics of recrystallization and grain growth	95
5-3 Modeling recrystallization and growth in machining of AA7075.....	97
5-4 Conclusions and future trends	100
6. PROCESS PATH FUNCTIONS.....	102
6-1 Generalized spherical harmonic expansion of ODF	102
6-2 ODF coefficients evolution in machining of AA7075	103
6-3 Determination of process path functions	105
6-4 Conclusions and future trends	114
7. MODELING THE EVOLUTION OF SECONDARY PHASES.....	116
7-1 The significance of precipitate refinement modeling.....	116
7-2 Continuum-Mechanical approach towards determination of stress fields in secondary phase	117
7-3 FEA Verification	125
7-4 Conclusions and future trends	127
8. CONCLUDING REMARKS AND OUTLOOK	130
REFERENCES	134

LIST OF TABLES

Table 2-1 Chemical composition of commercial AA7075 in weight percent (Wt%)[36]	18
Table 2-2 Mechanical Properties changes in T6 tempering of AA7075[36]	24
Table 3-1 Properties of the as-received AA7075[69]	42
Table 3-2 Dimensions of the insert and the holder used in experiments. The symbols are defined in Fig. 3.13 and the unit is millimeter[68]	43
Table 3-3 The changeable process parameters and the chosen low and high levels	43
Table 4-1. Frequently observed texture componets in rolling of Al and Al alloys[84]. The Euler angles are expressed in degrees.	60
Table 4-2. Most common FCC texture fibers with start and end Euler angles in degrees	61
Table 4-3 The 12 slip systems of FCC crystal	62
Table 4-4 Material parameters for AA7075 reported by[70]	66

LIST OF FIGURES

Fig. 1-1 Mallock's drawing of shearing of "layers" of hardened steel in cutting[1].....	1
Fig. 1-2 Schematic illustration of the materials-affected manufacturing concept[2]	3
Fig. 2-1 Dependence of the rate of recovery to the loading condition[22]	11
Fig. 2-2. EBSD image of recrystallized AISI1045 steel due to machining[24]	13
Fig. 2-3. TEM micrographs of (a) as-received AA1100 and (b) machined surface[25]. ...	13
Fig. 2-4 Recrystallization below the machined surface of Inconel 718 at different machining conditions[26]	14
Fig. 2-5 Recrystallization occurring below the machined surface of AISI 304L stainless steel[27]	14
Fig. 2-6, in TEM images showing an increases from (a) 214 to (b) 260 nm in the average grain size of OFHC copper due to machining[32]	15
Fig. 2-7 Machining of AA7075 creates a deformed layer below the machined surface shown by a white arrow[33]	16
Fig. 2-8 Texture evolution at the machined surface of OFHC copper in orthogonal cutting[34]	16
Fig. 2-9 comparison of the amount of the β phase in (a) as-received and (b) machined Ti64[35].....	17
Fig. 2-10 Increase in ductility (i.e. increase in reduction area) in tension of AA7075 by electrochemically induced recovery[41]	21
Fig. 2-11 (a) As-received and (b) recrystallized AA7075 obtained by high temperature tension tests[40]	21
Fig. 2-12 Grains orientation in AA7075 after (a) 1 pass and (b) 6 passes of accumulative roll bonding. (c) shows the legend of grain orientation[42]	22
Fig. 2-13 Pole figures showing texture characteristics of (a) as-received and (b) friction stir processed AA7075[43].....	22

Fig. 3-1 (a) Orthogonal cutting and (b) Oblique cutting geometry[6]	27
Fig. 3-2. The deformation zones in the cross-sectional view of orthogonal cutting. α_r and ϕ_c are the rake and shear angles respectively.	28
Fig. 3-3. Deformation diagram in orthogonal cutting[6].....	29
Fig. 3-4. Cutting force in AISI1040 steel as a function of rake angle γ [53]	31
Fig. 3-5. (a) the cutting force and (b) the thrust force in orthogonal cutting of AA7075[54].....	32
Fig. 3-6. Measurement of temperature profile in orthogonal cutting of Ti64[61].....	34
Fig. 3-7 Peak temperature prediction validated by experiments in orthogonal cutting of AA7075[33].....	34
Fig. 3-8. A close view of turning process[62]	35
Fig. 3-9. A schematic diagram of turning process with notation of forces and other parameters[6]	35
Fig. 3-10. Schematic of the geometry the insert in turning[6]	36
Fig. 3-11. (a) Notation of axes of coordinates and (b) schematic of standard chip formation in turning[6]	37
Fig. 3-12. Temperature measurement and analytical prediction in turning of AISI 5200 steel[67]	40
Fig. 3-13 Geometrical sketch of (a) Kennametal CNMA432-K68 insert and (b) Kennametal MCGNR-164D holder used in the turning experiments[68].....	42
Fig. 3-14. (a) The schematic geometry of the turning experiments. The area hatched by the red color is the cross-section normal to the axis of the cylindrical sample. (b) The top view of the normal cross-section. The machined surface (gray color) and the region investigated by characterization tool are schematically demarcated.....	44
Fig. 3-15. Schematic demonstration of the insert, the uncut surface and the analysis domain; the image taken from [71]. A 45° arc of the 25.4 mm diameter piece was analyzed in this research.....	46

Fig. 3-16 (a) the insert (blue) and the simulated arc in turning of the AA7075 (yellow); the mesh size variation is also shown. (b) the insert (gray) in cutting action.....	46
Fig. 4-1 The change in Young's modulus of Al single crystal as a function of rotation of axis of loading with respect to the single crystal orientation[76].....	49
Fig. 4-2 Plane strain compression curves of Al-4wt%Cu single crystal along different crystallographic orientations [77].....	49
Fig. 4-3. Schematic illustration of Euler angles defined by Bunge's notation. Image taken from[80].....	51
Fig. 4-4. (111) pole of figure of rolled AA7075[81]. The normal direction (ND) is the center of the pole figure.....	52
Fig. 4-5. A schematic of complete inverse pole figure of cubic materials. Each pole belongs to the certain plane labeled. Image taken from[82].....	53
Fig. 4-6. The inverse pole figure (IPF) of the as-received AA7075 material.....	55
Fig. 4-7 (a) the grain and (b) the image quality (IQ) maps of the as-received AA7075. The average confidence index (CI) of the scan was 0.42.....	55
Fig. 4-8 A 3D representation of the ODF of a hypothetical material[83].	57
Fig. 4-9 Constant φ 2cross-sections at 5° intervals of the ODF of the as-received AA7075	59
Fig. 4-10. Schematic illustration of α and β fibers[87].....	60
Fig. 4-11 (a) α , (b) β and (c) τ fibers of the as-received material	61
Fig. 4-12 Schematic illustration of crystal rotation in (a) uniaxial tension and (b) uniaxial compression. b denotes the slip direction[93]	63
Fig. 4-13. (a) effective strain and (b) effective strain rate obtained by FEM for simulating machining at $D = 1 \text{ mm}$, $F = 0.01 \text{ mm/rev}$ and $V = 500 \text{ rpm}$	67
Fig. 4-14. The points in the workpiece chosen for extracting mechanical data necessary for running the VPSC code.....	67

Fig. 4-15. FEA simulation results of (a) equivalent strain and (b) strain rate for machining under $D=1\text{ mm}$, $F=0.01\text{ mm/rev}$ and $V=5000\text{ rpm}$. The 10 points are demarcated in Fig. 4-15.	68
Fig. 4-16 The full velocity gradient tensor for average of points 4, 5 and 6 of Fig. 4-15. The red arrow shows the time steps that these point experience non-zero velocity gradient	69
Fig. 4-17 (a) The diagonal components of the average velocity gradient tensor for points 4, 5 and 6 of Fig. 4-15 under $D=1\text{ mm}$, $F=0.01\text{ mm/rev}$ and $V=5000\text{ rpm}$. (b) Checking the incompressibility conditions.	70
Fig. 4-18 (a) Experimental and (b) computational IPF for machining at $D=1\text{ mm}$, $F=0.01\text{ mm/rev}$ and $V=5000\text{ rpm}$	71
Fig. 4-19 (a) Experimental and (b) computational ODF for machining at $D=1\text{ mm}$, $F=0.01\text{ mm/rev}$ and $V=5000\text{ rpm}$	71
Fig. 4-20. Comparison of (a) α , (b) β and (c) τ fibers for machining and simulations under $D=1\text{ mm}$, $F=0.01\text{ mm/rev}$ and $V=5000\text{ rpm}$	72
Fig. 4-21 Comparison of (a) equivalent strain and (b) equivalent strain rate for 1 and 3 mm depths of cut. F and V were respectively 0.01 mm/rev and 5000 rpm for both of the cases.	73
Fig. 4-22 (a) Experimental and (b) computational IPF for machining at $D=3\text{ mm}$, $F=0.01\text{ mm/rev}$ and $V=5000\text{ rpm}$	74
Fig. 4-23 (a) Experimental and (b) computational IPF for machining at $D=3\text{ mm}$, $F=0.01\text{ mm/rev}$ and $V=5000\text{ rpm}$	74
Fig. 4-24 Comparison of (a) α , (b) β and (c) τ fibers for machining and simulations under $D=3\text{ mm}$, $F=0.01\text{ mm/rev}$ and $V=5000\text{ rpm}$	75
Fig. 4-25. Comparison of (a) equivalent strain and (b) equivalent strain rate for 0.01 mm/rev and 0.8 mm/rev feed rates. D and V were respectively 1 mm and 5000 rpm for both of the cases.	76

Fig. 4-26 (a) Experimental and (b) computational IPF for machining at $D=1\text{ mm}$, $F=0.08\text{ mm/rev}$ and $V=5000\text{ rpm}$	77
Fig. 4-27. 4-28 (a) Experimental and (b) computational ODF for machining at $D=1\text{ mm}$, $F=0.08\text{ mm/rev}$ and $V=5000\text{ rpm}$	77
Fig. 4-29. Comparison of (a) α , (b) β and (c) τ fibers for machining and simulations under $D=1\text{ mm}$, $F=0.08\text{ mm/rev}$ and $V=5000\text{ rpm}$	77
Fig. 4-30 FEA results of equivalent strain and strain rate in (a) 200 and (b) 5000 rpm spindle speed. $D=3\text{ mm}$ and $F=0.8\text{ mm/rev}$ for both the cases.	78
Fig. 4-31 (a) Experimental and (b) computational IPF for machining at $D=3\text{ mm}$, $F=0.08\text{ mm/rev}$ and $V=200\text{ rpm}$	79
Fig. 4-32. (a) Experimental and (b) computational ODF for machining at $D=3\text{ mm}$, $F=0.08\text{ mm/rev}$ and $V=200\text{ rpm}$	80
Fig. 4-33. Comparison of (a) α , (b) β and (c) τ fibers for machining and simulations under $D=3\text{ mm}$, $F=0.08\text{ mm/rev}$ and $V=200\text{ rpm}$	80
Fig. 4-34. (a) Experimental and (b) computational IPF for machining at $D=3\text{ mm}$, $F=0.08\text{ mm/rev}$ and $V=5000\text{ rpm}$	81
Fig. 4-35 (a) Experimental and (b) computational ODF for machining at $D=3\text{ mm}$, $F=0.08\text{ mm/rev}$ and $V=5000\text{ rpm}$	81
Fig. 4-36. Comparison of (a) α , (b) β and (c) τ fibers for machining and simulations under $D=3\text{ mm}$, $F=0.08\text{ mm/rev}$ and $V=5000\text{ rpm}$	81
Fig. 4-37 comparison of texture fibers predicted by the computer model	83
Fig. 5-1 The grain size distribution of the as-received material. The average grain size is $31.6\text{ }\mu\text{m}$ and the standard deviation is $23.1\text{ }\mu\text{m}$	86
Fig. 5-2. (a) The IPF-overlaid grain map and (b) the image quality map for the sample machined at $D=1\text{ mm}$, $F=0.01\text{ mm/rev}$ and $V=5000\text{ rpm}$. The average CI of the image is 0.31.	86

Fig. 5-3. Grain size distribution the sample machined at $D= 1\text{ mm}$, $F = 0.01\text{ mm/rev}$ and $V=5000\text{ rpm}$. The average grain size is $44\text{ }\mu\text{m}$ and the standard deviation is $25.65\text{ }\mu\text{m}$...	87
Fig. 5-4 Depth of penetration of (a) temperature and (b) maximal strains and strain rates in the sample machined at $D= 1\text{ mm}$, $F = 0.01\text{ mm/rev}$ and $V=5000\text{ rpm}$	88
Fig. 5-5(a) The IPF-overlaid grain map and (b) the image quality map for the sample machined at $D= 3\text{ mm}$, $F = 0.01\text{ mm/rev}$ and $V=5000\text{ rpm}$. The average CI of the image is 0.26	89
Fig. 5-6. Grain size distribution the sample machined at $D= 3\text{ mm}$, $F = 0.01\text{ mm/rev}$ and $V=5000\text{ rpm}$. The average grain size is $19.6\text{ }\mu\text{m}$ and the standard deviation is $18.12\text{ }\mu\text{m}$	89
Fig. 5-7(a) The IPF-overlaid grain map and (b) the image quality map for the sample machined at $D= 1\text{ mm}$, $F = 0.8\text{ mm/rev}$ and $V=5000\text{ rpm}$. The average CI is 0.46.....	91
Fig. 5-8 Grain size distribution the sample machined at $D= 1\text{ mm}$, $F = 0.8\text{ mm/rev}$ and $V=5000\text{ rpm}$. The average grain size is $42.5\text{ }\mu\text{m}$ and the standard deviation is $18.4\text{ }\mu\text{m}$..	91
Fig. 5-9 Maximum temperature of the workpiece below machined surface predicted by FEA.....	92
Fig. 5-10 (a) The IPF-overlaid grain map and (b) the image quality map for the sample machined at $D= 3\text{ mm}$, $F = 0.8\text{ mm/rev}$ and $V=200\text{ rpm}$. The average CI is 0.26.....	92
Fig. 5-11 Grain size distribution the sample machined at $D= 3\text{ mm}$, $F = 0.8\text{ mm/rev}$ and $V=200\text{ rpm}$. The average grain size is $23.8\text{ }\mu\text{m}$ and the standard deviation is $15.8\text{ }\mu\text{m}$	93
Fig. 5-12 The IPF-overlaid grain map and (b) the image quality map for the sample machined at $D= 3\text{ mm}$, $F = 0.8\text{ mm/rev}$ and $V=5000\text{ rpm}$. The average CI is 0.25.....	94
Fig. 5-13 Grain size distribution the sample machined at $D= 3\text{ mm}$, $F = 0.8\text{ mm/rev}$ and $V=5000\text{ rpm}$. The average grain size is $24.2\text{ }\mu\text{m}$ and the standard deviation is $22.7\text{ }\mu\text{m}$..	94
Fig. 5-14. Predicted change in the average grain size in machining at $D= 1\text{ mm}$, $F = 0.01\text{ mm/rev}$ and $V=5000\text{ rpm}$. The average grain size is $39\text{ }\mu\text{m}$	98
Fig. 5-15 Predicted change in the average grain size in machining at $D= 3\text{ mm}$, $F = 0.01\text{ mm/rev}$ and $V=5000\text{ rpm}$. The average grain size is $23\text{ }\mu\text{m}$	98

Fig. 5-16 Predicted change in the average grain size in machining at $D= 1\text{ mm}$, $F = 0.8\text{ mm/rev}$ and $V=5000\text{ rpm}$. The average grain size is $38\text{ }\mu\text{m}$	99
Fig. 5-17 Predicted change in the average grain size in machining at $D= 3\text{ mm}$, $F = 0.8\text{ mm/rev}$ and $V=200\text{ rpm}$. The average grain size is $27\text{ }\mu\text{m}$	100
Fig. 5-18 Predicted change in the average grain size in machining at $D= 3\text{ mm}$, $F = 0.8\text{ mm/rev}$ and $V=5000\text{ rpm}$. The average grain size is $40\text{ }\mu\text{m}$	100
Fig. 6-1 Changes in GSH coefficients of the experimental and computational ODF with imposed by increasing the depth of cut	104
Fig. 6-2 Changes in GSH coefficients of the experimental and computational ODF with respect to the change in feed rate	105
Fig. 6-3 Changes in GSH coefficients of the experimental and computational ODF with increasing the spindle speed	106
Fig. 6-4 The evolution of AA7075 machined under different feed rates at $D = 1\text{ mm}$ and $V = 5000\text{ rpm}$	108
Fig. 6-5 The hyper-surface containing all the possible microstructure achievable by changing the feed rate. Red points show the computationally determined points.	108
Fig. 6-6 Polynomial fitting of changes in computationally determined microstructure coefficients obtained by varying the feed rate.....	109
Fig. 6-7 The effects of increasing depth of cut in (a) The evolution of microstructure coefficients in AA7075 (b) a hyper-surface containing the possible processing paths leading to the possible microstructures. The red points show the simulation points.	111
Fig. 6-8 The effects of increasing spindle speed (a) The evolution of microstructure coefficients (b) a hyper-surface containing the possible processing paths leading to the possible microstructures. The red points show the simulation points.	111
Fig. 6-9 congregation of all the microstructural paths obtained for simulations for the three process parameters. The hyper surface shows the possible microstructures. The red points show the simulation points	112

Fig. 6-10 The Hall-Petch plot for the hardness of the machined samples.....	113
Fig. 7-1 Schematic sectioning of the ellipsoidal particle to determine the stress. Blue arrows represents traction and red arrow represent stress. The black arrow represents the unit normal to the cross-section.....	124
Fig. 7-2. Schematic illustration of the elliptical surface of cross sectioning and ellipsoid	125
Fig. 7-3 constant stress contours of the first principal stress in uniaxial loading for (a) $\theta = 0^\circ$ and (b) $\theta = 45^\circ$. x represents the position in the particle and a is the major semi-axis of the elliptical particle. (c) and (d) are FEM simulations respectively corresponding to (a) and (b).	126
Fig. 7-4 constant stress contours of the first principal stress in pure shear at constant shear strain rate as a function of θ ; x represents the position in the particle and a is the major semi-axis of the elliptical particle. (b) the FEM simulation result for the case pure shear loading at $\theta = 45^\circ$ and shear strain rate of 2700 s^{-1}	127
Fig. 7-5 Comparison of CM and FEM approaches in uniaxial tension.....	128
Fig. 7-6 Comparison of CM and FEM approaches in pure shear	128

SUMMARY

Depending on the material system and machining conditions, the localized strain, strain rate and temperature fields induced to the material during the machining process can be intense. Therefore, a wide variety of microstructural evolutions are likely to occur below the machined surface. These microstructural changes take place at various scales. First of all, due to the severe plastic deformation below the machined surface, the crystallographic orientation of grains can change dramatically. In addition, if the levels of the induced temperature and strain are high enough, recrystallization may occur, new grains may form and subsequently grow. Additionally, contingent upon the duration of the machining process, partial grain growth might also happen. Last but not least, if the material is consisted of more than one phase, the microstructural characteristics of secondary phases will also evolve. The ultimate result of all the aforementioned evolutions produces remarkable changes in the mechanical and thermal (and almost all other) properties of the material, which consequently affect the response of the material during service.

A comprehensive modeling framework that reliably captures all the aspects of the above microstructural evolutions in machining is absent in the open literature. This work coalesces concrete and all-inclusive modeling toolsets into a unified scheme to follow the mentioned phenomena in machining of aluminum alloy 7075. The modeling outcomes are verified by experimental results to assure reliability. Finite element analyses were applied to obtain the stress, temperature, strain and strain rate fields developed in the material during machining at different parameters. Kinetic-based models were exploited to determine the possible recrystallization or grain growth. A viscoplastic self-consistent crystal plasticity model was utilized to investigate texture evolution below the machined surface. Also for multi-phase materials, the first steps in developing a totally new

constitutive model to yield the extent of the possible refinement in the second phase precipitates, were taken.

The main goal of the work was to link the above-mentioned microstructural evolutions to process parameters of machining by mathematical derivation of process path functions. Therefore, prediction of microstructural changes as a result of changing the process parameters became possible; which has significant industrial potential and importance. Additionally, such a direct and complete linkage between machining and microstructure is completely new to the scientific community in manufacturing and design fields.

1. INTRODUCTION

1.1 Motivation

A. Mallock is amongst the very first researchers who investigated the behavior of materials under cutting action [1]. Fig. 1-1 shows Mallock's sketch published in 1881, where he suggests a shearing mechanism in shaving of "layers" of hardened steel in orthogonal cutting. Mallock was interested in relating the chip behavior to cutting angles and geometry of the tool used in cutting of different materials. From his time till now, the interaction of cutting tools and devices with the material being processed, has been the subject of apparently endless research.

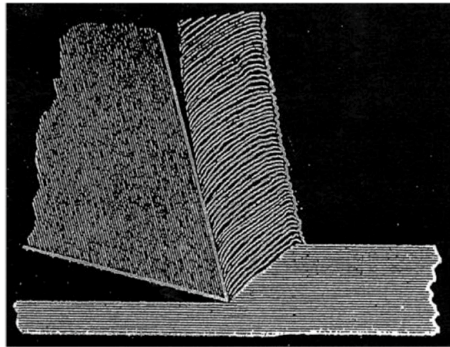


Fig. 1-1 Mallock's drawing of shearing of "layers" of hardened steel in cutting[1]

During the next century, researchers concurred that in almost any cutting or machining process, two categories of parameters namely "manufacturing parameters" and "material parameters", play the most significant roles. A complete understanding of a machining process results in obtaining the necessary force or power required for the process, stress fields induced to the material, deformation zones in the material, chip formation and etc. Obviously, another part of such wholesome comprehension is identification of the response of the material to the above phenomena. Depending on the process, manufacturing parameters can include tool speed, material feed rate, tool angle

and other geometrical parameters, cooling, lubrication and etc. Manufacturing parameters are usually considered as independent parameters and are dictated by the user or the limitations of the specific machining process or the device. On the other hand, material parameters (in this context, equivalently material properties) such as hardness, inelastic and elastic constitutive law constants, thermal conductivity and so forth are usually dependent parameters and are functions of manufacturing parameters and initial attributes of the material. The functionality of material parameters with respect to manufacturing parameters originates from the fact that the microstructure of the material undergoing machining, “evolves” dynamically as the process continues. Because properties of materials are strongly dependent on the microstructure, the manufacturing parameters affect the material parameters during the process. Therefore, investigating the microstructural evolutions in machining is of prime importance. Also, since it is usually desired to know the properties of the material after machining, following the microstructural changes during the process is absolutely necessary.

The microstructural phenomena occurring in manufacturing processes can be divided into two general groups. The first group consists of the microstructure changes produced by plastic deformation or the temperature rise during machining. The second group is comprised of the evolutions that are produced by residual stresses and occur after machining. Obviously, the first group of the microstructural phenomena has the same nature as “material parameters” introduced above, since they affect the process. This group includes changes in crystallographic texture, grain size and size distribution evolutions, changes in grain boundary attributes, changes in chemical composition (mechanically activated phase transformations), defect density changes and so on.

Recently, a novel concept called materials-affected manufacturing has been proposed [2] which iteratively incorporates the material properties as process inputs into manufacturing mechanics models as shown by Fig. 1-2. This new concept states that since the property evolution is dynamically changing (due to dynamic evolution of

microstructure during machining) as the manufacturing process goes on; the change in the material attributes should be iteratively integrated into the process to achieve a far more accurate description of the mechanics of machining process.

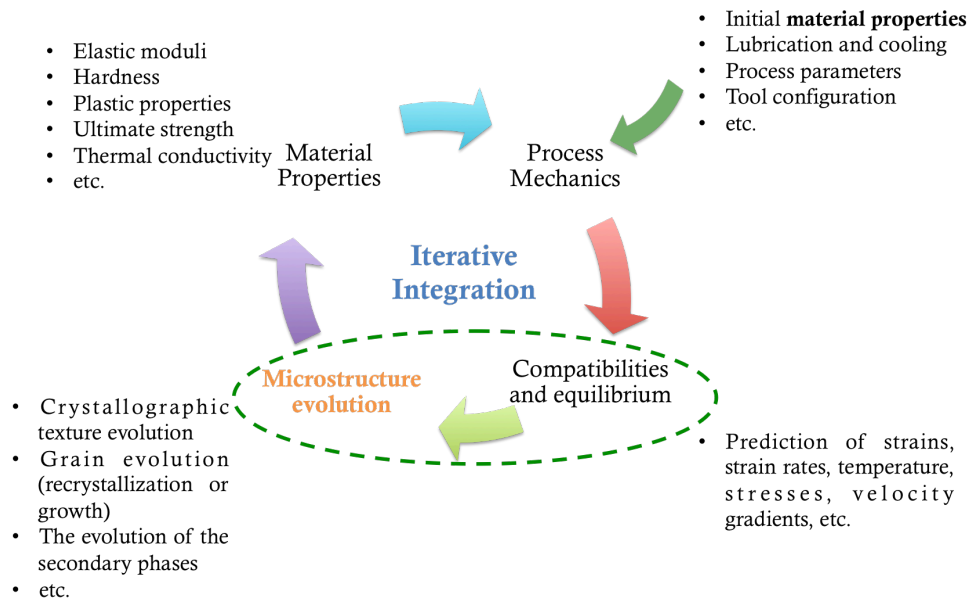


Fig. 1-2 Schematic illustration of the materials-affected manufacturing concept[2]

The whole purpose of the materials-affected manufacturing is to more accurately model manufacturing processes. Still, because of being recently proposed, this new concept needs to be tested in terms of applicability and feasibility and should be compared to the available non-iterative manufacturing models and to experimental results for checking the level of accuracy it can provide. The first step in the implementation and testing the materials-affected manufacturing concept, which constitutes the focus of this work, is shown by the green dashed ellipse in Fig. 1-2. The extent of the section, covers obtaining all the field variables induced to the material due to machining and subsequently, determining the totality of material response and microstructure evolutions

as a result of the manufacturing process. Therefore this part of the work in testing and implementing the concept contains the details of all the essential microstructural evolutions occurring as a function of applied mechanical and thermal loads in turning. Fundamental innovations in materials-focused part of testing and implementing the newly proposed concept are as follows:

- Systematic capturing of materials microstructural evolution during manufacturing
- Accurate prediction of macro-scale materials properties after processing.
- Quantitative estimation of the effects of manufacturing process parameters on materials properties and service behavior.
- Achieving a computational microstructural design and materials selection tool by exploiting the inverse of the developed procedure.

The potential benefits of the above contributions to fields of manufacturing and materials science and engineering are as follows:

- i. Development a new and systematic methodology enabling predictive modeling and planning of manufacturing processes in achieving desirable materials properties and functionalities.
- ii. Satisfaction of the skyrocketing demand of more accurate prediction of manufacturing processes.
- iii. Integrating manufacturing process mechanics and material microstructural dynamics in multi-scale and dual-causality frameworks for high fidelity modeling and analysis.
- iv. Decoding the complicated interactions between process and materials and offering a clear path to avoid developmental trial-and-errors thus achieving “first-and-every-part-correct” manufacturing.

1.2 Objectives and scope

The ultimate goal of the current work is to obtain a comprehensive toolset capable of correlating manufacturing process parameters to microstructural characteristics and subsequently to properties of the processed materials through computational modeling validated by solid experimentations. This ultimate goal, can be further fragmented into the following smaller objectives:

- Computational determination of thermo-mechanical loads (i.e. stresses, strains and strain rates, temperature, etc.) induced to the material during manufacturing.
- Capturing the effects of the thermo-mechanical loads on the microstructure of the material under study through computational modeling
- Validation of occurrence of predicted microstructural evolutions due to the loads by concrete experimentation.
- Obtaining the process path functions by computationally continuation of changing the process parameters and following the evolutions in the microstructure.

In connection to the innovations and benefits mentioned in section 1-1, and in order to achieve the above objectives; the turning process and aluminum alloy (AA) 7075, were respectively chosen as the manufacturing process and the material system to focus on.

The scope of this work extends to setting depth of cut, feed rate and the spindle speed as the process parameters to study and correlate to microstructural changes. For each of these parameters, one high and one low level were selected. The material was machined under the significant combinations of high and low levels of each parameter. Microstructural characterizations were performed on the machined samples and the observed modifications in the microstructure were attributed to the changes in process parameters. Crystallographic texture and grain size and size distribution are the

experimentally investigated microstructural features. Microhardness measurements below the machined surface were conducted to exhibit the significant effects of the microstructural changes in the properties of the material.

In parallel, finite element (FE) analysis was chosen as the main computational tool to determine the thermo-mechanical loads exerted on AA7075 in turning. Initially, complete FE simulations were performed for each machined case to determine the temperature and all the components of strain, strain rate and stress tensors induced to the material due to machining. In order to capture texture evolution, crystal plasticity modeling was performed based on the output of FE simulations. Additionally, kinetic-based equations of recrystallization and grain growth were coupled with the FE code to yield the extent of grain size evolution as a function of the thermo-mechanical loads.

In addition to determination of the cases which computational results have the most agreement with experimental observations, the process parameters were continued to change in FE simulations. For all these “pure computational” cases (i.e. not accompanied by experiments), the same procedures of modeling microstructural evolutions were followed. Finally, the microstructural attributes for texture evolution, were mathematically transferred in a microstructure hull to yield the process path function of machining AA7075, which is a pure numerical tool which is capable of predicting texture evolution without any machining, FE simulations and crystal plasticity modeling being done.

In addition, the very first steps in including the modeling the evolution of secondary phases were taken by introducing an all-new continuum-mechanical model which determines the stress fields inside the secondary phases as a function of thermo-mechanical loads.

From the perspective of materials-affected manufacturing, there is still a gap between manufacturing and materials science. This work, constructs a solid foundation to link the two sciences from this perspective. Inevitably, filling up the whole gap with

reliable knowledge requires an enormous amount of work, beyond the scopes of this dissertation. In this regard, experimental and computational investigations of higher order microstructural evolution parameters (such as dislocation density) and the modeling and testing the change in properties (except microhardness below the machined surface) as a result of machining are out of the scopes of the current dissertation. Furthermore, testing different modeling frameworks such as analytical models of determination of field variables in machining or various crystal plasticity schemes or recrystallization models for comparing to each other and to experimental results are beyond the scope of this work.

1.3 Organization of the dissertation

Due to the nature of the present research, which requires connecting manufacturing and materials sciences in a fashion never reported before; several different modeling schemes are tied to experiments. To follow the conventions of the scientific community, brief literature reviews and/or methodology explanations are presented for each modeling framework or the experimental part.

However, in order to avoid confusion and promote easy readership, chapter two is completely devoted to a literature review on microstructural evolutions in materials due to thermo-mechanical processing. In this regard, first the microstructural evolutions induced by machining of different metal are briefly reviewed. The next section focuses on characteristics and attributes specific to AA 7075. To summarize the main points, the chapter is concluded with a “summary” section.

Chapter 3 outlines the thermo-mechanics of cutting by establishing a connection between process parameters in metal cutting and field variables induced to the workpiece. The chapter continues to explain the experimental methodology applied in this work. Then, details of the FE analysis reported in this dissertation, are identified. Again, the important materials covered in the chapter are summed up in the final summary section.

Chapter 4 focuses on texture evolution. The first section of the chapter is a necessary introduction to the texture topic, to define the jargon used in the analysis of the results and to familiarize the reader with the conventions in texture analysis. The chapter continues to a brief explanation of the applied methodology for texture evolution modeling. Then the experimental and computational results are discussed and compared. Since this chapter mainly serves as the means to validate modeling results or to determine under which processing conditions models are most accurate; the presentation of results involves in comparison between simulations and experiments. This chapter concludes with the “conclusion and future trends” sections, which summarizes the findings and suggests the research direction to continue the work.

Chapter 5 discusses the observed changes in the grain size related aspects of microstructural evolution in machining. Similar to chapter 4, a brief introduction of modeling scheme used to capture recrystallization and grain growth is mentioned. Then a complete comparison between experimental and modeling results is conducted. The important outcomes of discussions of the chapter as well as suggestions for future research are summarized in the last section.

Chapter 6 starts with mathematical foundation of establishing the process path functions, which are the computational means of yielding the texture evolutions without any necessity of performing experiments or FE simulations. However, reliable derivation of the process path functions requires a few more FE runs followed by crystal plasticity models. These new results in addition to outcomes of chapter 4 are exploited to construct the process path functions for machining of AA7075. Similar to previous chapters, this chapter concludes with a summary of discussions and recommendations for future trends.

Chapter 7 focuses on the very first steps taken for modeling the evolution of secondary phases due to the application of thermo-mechanical loads to a multi-phase material. An analytical model, purely based on continuum mechanical formalism is introduced in this chapter. Then, the model is applied to a hypothetical case of simple

mechanical loading on AA7075 with large enough secondary η precipitates. Well-established FE simulations verify the results of this novel continuum-mechanical model. Similar to previous chapters, the final section includes a summation of findings as well as propositions on how to couple this model with the materials-affected manufacturing framework.

The final chapter of this dissertation is a summary of all the conclusion points and an outlook at the horizon of continuing the work on founding a robust connection between materials and manufacturing science and engineering.

2. BACKGROUND AND LITERATURE REVIEW

2-1 Microstructural phenomena in metals

In addition to selecting an optimized material system for any product, careful control of the microstructure is extremely important. There are a large number of reports on failure of parts due to microstructural deficiencies in optimal material systems[3-5]. Manufacturing processes impose inevitable effects on the microstructure of the material being used for a product. As a result, in a vast majority of engineering products, microstructural control steps such as heat treatment are necessary after finishing manufacturing steps. In a comparatively fewer cases of products such as machining [6-9], it is possible to combine the microstructure control steps (or at least a portion of such steps) and manufacturing steps. There are several potential benefits in integrating the microstructure control and manufacturing steps including the economic gains due to eliminating the costly microstructure control steps, as well as the possibility of robust prediction of performance of the material based on manufacturing parameters. Such a carefully designed manufacturing process is called “thermo-mechanical control processing” [10-12].

In thermo-mechanical processing of metals, a broad spectrum of mechanisms can cause the evolution of the microstructure. Additionally the evolution can occur at different grain-aggregate [13, 14], grain and sub-grain [15] and defect levels [16-18]; or it can be localized (like surface evolution in machining processes [7]) or volume-distributed [10, 11]. In most cases, mechanical and thermal loads applied to the material cause such microstructural evolutions. Irradiation [19], energetic-particle bombardment [20] and a few other types of loads [10] can also evolve the microstructure. The most common microstructural modifications (usually regardless of the nature of the cause) include recovery, recrystallization, grain growth and crystallographic texture evolution and phase transformations (including precipitation) if the alloy system allows [10, 11]. Descriptions

of most important microstructural phenomena occurring in thermo-mechanical processes is as follows:

Recovery

Recovery is the relaxation of stored strain energy in the material. Microscopic observations suggest that recovery is thermodynamically a thermally activated process, which kinetically requires a minimum level of stored strain energy to occur. Recovery is accompanied by a reduction in dislocation density and therefore reduces the yield strength of the metal and increases the ductility. As an example of softening effects of recovery, Li et al. investigated AA7005 under uniaxial compression test with different loading rates and concluded that the activation energy for recovery is 147 kJ/mol for that specific alloy [21]. As mentioned, the kinetic of recovery is affected of loading (stored strain energy). Souza et al. studied the rate of recovery in austenitic stainless steels and obtained its relationship with peak stress as shown in Fig. 2-1. They also obtained semi-empirical equations to relate the kinetics of recovery to loading conditions [22].

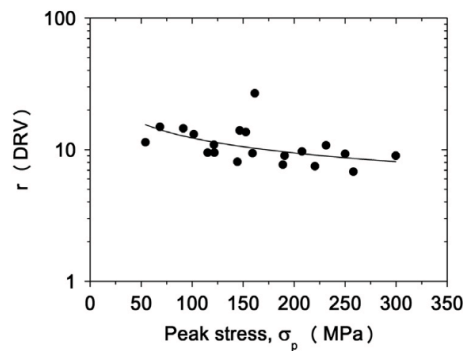


Fig. 2-1 Dependence of the rate of recovery to the loading condition[22].

Some authors prefer not to call recovery a “ microstructural evolution” [11]; mainly due to lack of microscopically visible effects of recovery on the microstructure in most cases. Nonetheless it is definitely a microstructural modification that can have tangible effects on the properties and response of the material [10].

Recrystallization

Recrystallization is replacement of deformed grains by new non-deformed grains. Thermodynamics and kinetics of recrystallization is somehow similar to recovery, which makes most of the authors consider recrystallization as a subsequent step to recovery (and not considering recovery as a separate step) [23]. In fact, separation of the end of recovery and onset of recrystallization can be difficult when a polycrystalline aggregate is considered. Unlike recovery, in recrystallization, nucleation can alter the kinetics (in addition to stored strain energy) since recrystallization is fundamentally based on nucleation of new grains. The recrystallized microstructure usually has a much smaller average grain size compared to the deformed state. The average recrystallized grain size depends on the availability of nucleation sites and the rate of growth of nuclei. “Dynamic recrystallization” occurs when the temperature is high enough in a thermo-mechanical process and recrystallization and deformation occur simultaneously; while the recrystallization triggered after mechanical deformation is so-called “static recrystallization”[23].

Dynamic recrystallization of a machined surface is a relatively common phenomenon. Courbon et al. recently reported recrystallized grains as a result of machining of AISI1045 steels [24]. Fig. 2-2 shows an Electron Back Scatter Diffraction (EBSD) image showing recrystallized areas after machining. It is reported that the average grain size of the machined surface was 200 nm while the initial grain size was between 10 to 20 μm [24].

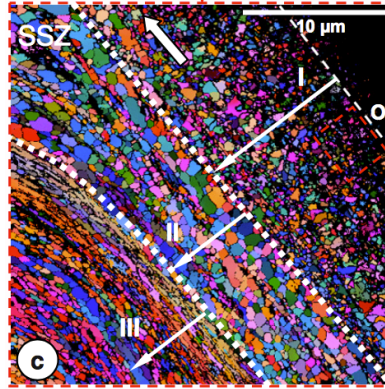


Fig. 2-2. EBSD image of recrystallized AISI1045 steel due to machining[24]

Recrystallization due to machining has also been observed in Al-based materials. Fig. 2-3 shows the transmission electron microscope (TEM) micrographs of (a) as-received and (b) a machined surface of AA1100. According to Ni et al. [25] a refined recrystallized structure comprised mostly of equi-axed smaller grains was obtained.

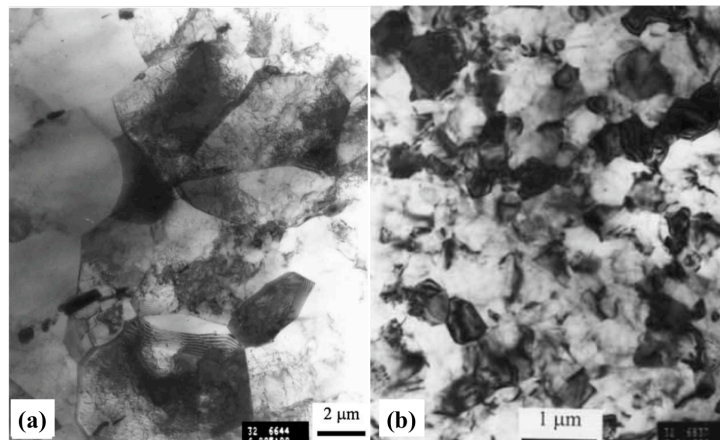


Fig. 2-3. TEM micrographs of (a) as-received AA1100 and (b) machined surface[25].

In a similar study on Inconel 718, a recrystallized region was observed below the machined surface in different machining conditions [26]. Fig. 2-4 shows the corresponding EBSD maps. Another report on AISI 304L stainless steel shows a severe recrystallization extending $150\ \mu\text{m}$ deep below the machined surface as shown by Fig. 2-5[27].

In addition to experiments, simulations also predict occurrence of grain refinement and recrystallization in machining of several alloy systems including Ti[18], Cu and Al [28], AA7075 [29, 30] and Inconel[31].

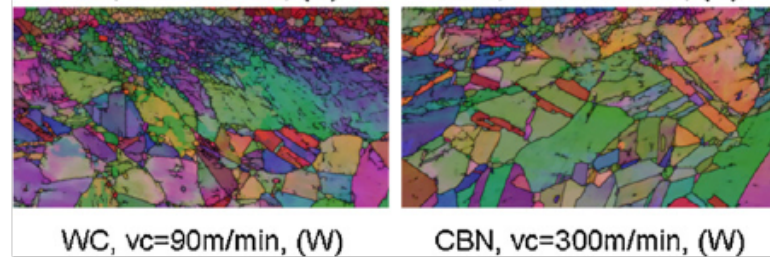


Fig. 2-4 Recrystallization below the machined surface of Inconel 718 at different machining conditions[26]



Fig. 2-5 Recrystallization occurring below the machined surface of AISI 304L stainless steel[27]

Grain growth

Grain growth is usually considered a fully thermal process, meaning that both thermodynamic and kinetic (movement of grain boundaries) are controlled by temperature[23]. The higher the temperature is (prior to melting), the larger the grains

become. Coalescence of all the grains in a polycrystalline aggregate into a single crystal is not possible due to several factors including all the microstructural inhomogeneities, which restrict growth of grains. Fig. 2-6 demonstrates an example of machining-induced grain growth in OFHC copper where an increase in the average grain size from 214 *nm* to ~260 *nm* is observed by machining [32].

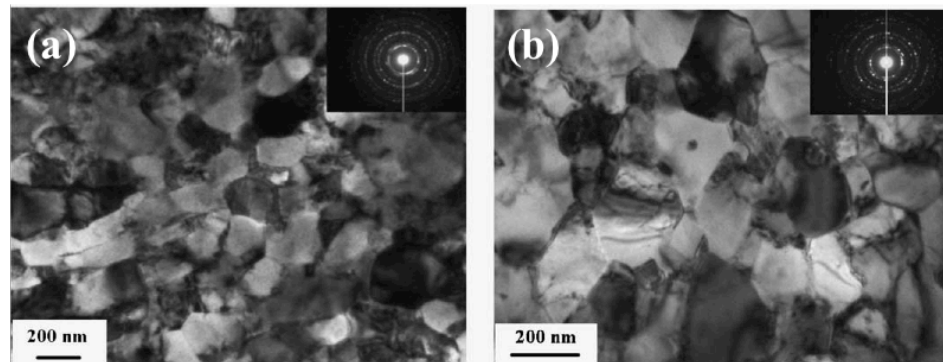


Fig. 2-6, in TEM images showing an increases from (a) 214 to (b) 260 nm in the average grain size of OFHC copper due to machining[32]

Preferred crystallographic orientation (Texture)

Depending on the intensity, plastic deformation can re-orient the grains in a polycrystalline aggregate along one (or more) preferred orientation(s) also known as “texture”. Fig. 2-7 illustrates observation of a deformed layer below the machined surface of AA7075 [33]. Depending on the material system and slip and twinning systems, such deformations will lead to texture evolution. Thermodynamically, re-orientation of grains occurs because slip of certain crystallographic planes is easier (thermodynamically more favorable) along certain direction when a mechanical load is applied. Kinetics of plastic deformation is usually controlled by temperature and rate of application of the mechanical load. Materials constants, hardening phenomena and microstructural inhomogeneities restrict the extent of preferred orientation.

As an example of machining-induced texture evolution, Fig. 2-8, shows Experimental observations and simulation results of texture evolution in orthogonal cutting of OFHC copper[34].

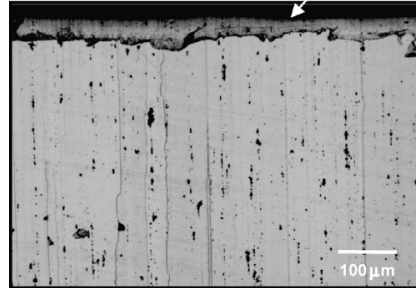


Fig. 2-7 Machining of AA7075 creates a deformed layer below the machined surface shown by a white arrow[33]

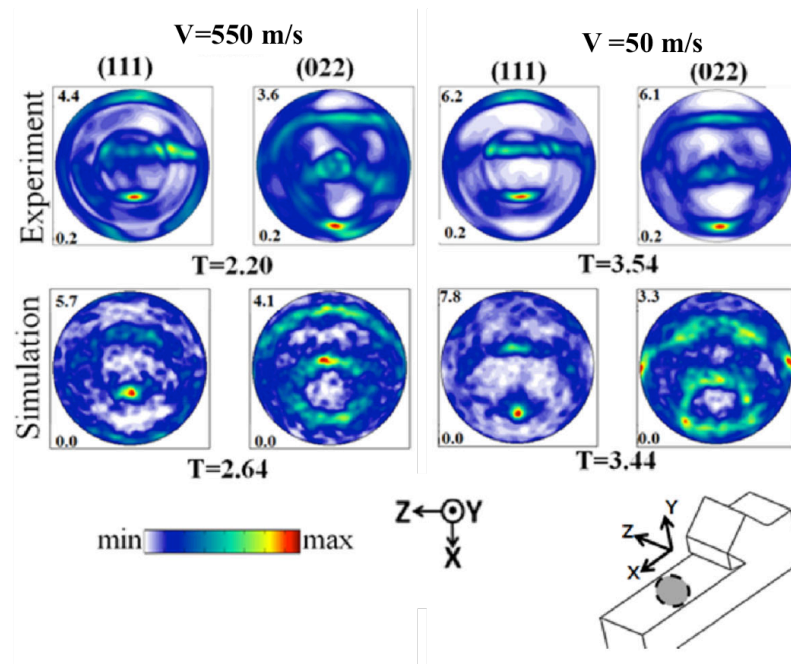


Fig. 2-8 Texture evolution at the machined surface of OFHC copper in orthogonal cutting[34]

Phase transformations

Depending on the chemistry of the base metal and alloying elements and the corresponding phase transformations (e.g. eutectoid and peritectoid transformations) an alloy system can accommodate precipitation of new secondary phases. The

thermodynamics and kinetics of nucleation and growth or dissolution of precipitates is often a complicated function of mechanical and thermal and thermal stimulants and differs from case to case. Presence, average size and distribution of precipitates can lead to remarkable modification in mechanical properties of the material; as rule of thumb, precipitates increase the strength of the material and generally reduce fracture toughness and fatigue endurance. The finer the precipitates are, the higher is the strength and the lower are the adverse effects. Additionally, morphology and distribution (segregated at the grain boundaries or inside the grains) of the precipitates affect the impact on material behavior. An example of a report on machining induced phase transformation is shown in Fig. 2-8. Machining loads promote β phase precipitation in the Ti64 system, on the machined surface[35].

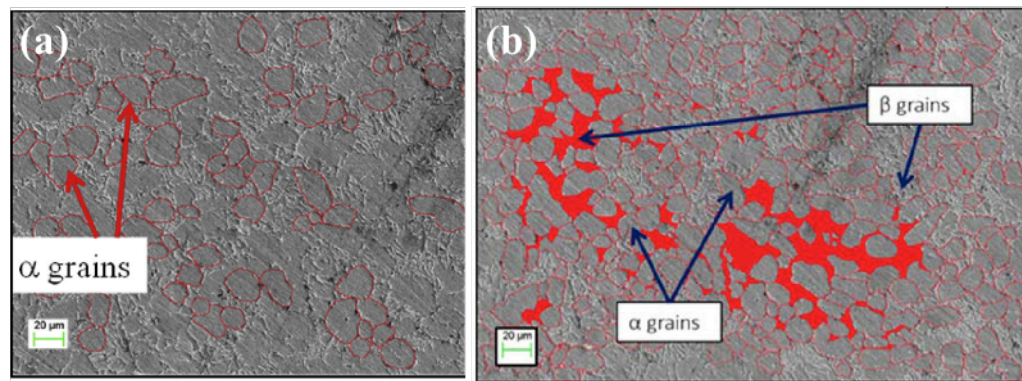


Fig. 2-9 comparison of the amount of the β phase in (a) as-received and (b) machined Ti64[35]

2-2 Microstructural phenomena in aluminum alloy 707

2-2-1 General characteristics of AA 7075

Aluminum and its alloys possess one of the highest specific elastic modulus (i.e. elastic modulus to weight ratio), specific strength, high ductility and relatively high corrosion resistance. Additionally, aluminum is the most abundant metal in the Earth's crust (the second most abundant element after semi-metal Si) and is a relatively easy and

low-cost metal to smelt and cast. The combination of the above characteristics made Al and its alloys one of the most widely used metallic materials today. Many industries such as aerospace, automobile, shipbuilding, construction, electronic and packaging industries heavily depend on aluminum [36, 37]. In 2013, more than 1.9 million metric tons of Al was produced in the U.S. The total Al demand of the U.S. in the same year was 10.94 million metric tons [38]. Al crystallizes in the face-centered cubic (FCC) system possessing 12 slip systems. Ductility of Al and its alloys increases with temperature. Elongation of most Al alloys become almost double compared to room temperature at temperatures above 400°C. Aluminum alloy (AA) 7075 is one of the most widely used members of the 7000 Al alloy family. 7075 has zinc and magnesium as major alloying elements. Chemical composition of commercial AA7075 is listed in Table 1-1 in weight percent [36].

Table 2-1 Chemical composition of commercial AA7075 in weight percent (Wt%)[36]

Al	Si	Fe	Cu	Mn	Mg	Cr	Zn	Ti	Zr	Other
bal.	0-0.4	0-0.5	1.2-2	0.0.3	2.1-2.9	0.18-0.29	5.1-5.6	0-0.2	0-.04	0-0.15

The 7000 Al alloy series are probably the highest strengths family of aluminum alloy commercially available. AA7075 possesses superior fatigue endurance, but can show low fracture toughness compared to other Al alloys, especially after some heat treatment procedures such as the T6 [36]. Due to the high strengths, AA7075 found a large number of aerospace applications after World War II and as early as 1950's. Recently, better candidates emerge for a few of the applications of AA7075 in aerospace industry. Nonetheless the alloy still is one of the most highly used materials (metallic or non-metallic) in aircrafts [36, 37].

The reported microstructural evolution in thermo-mechanical processing of AA7075 parts can be categorized based on the processing temperature as hot working, warm working and cold working [11]. Processing occurring below the melting (or

solidus) temperature and above the recrystallization temperature is called hot working. On the other hand, cold working is referred to processes occurring well below recrystallization temperatures, mainly at room temperature. The recrystallization temperature of Al based alloys is often considered as almost half of the melting temperature. The reported recrystallization temperature for AA7075 is reported in the range 320-450 °C depending on the intensity of the applied strain [29, 39, 40]. Recrystallization of as-cast AA7075 materials occurs at the low extreme of the temperature range due to high thermodynamic tendency of the coarse dendritic structure to fragment into refined grains [10]. Additionally, the large intermetallic precipitates that usually segregate along the grain boundaries in the as-cast microstructures get refined and more evenly redistributed in the interior of the grains during hot working. It has been reported that the Al based alloys are prone to abnormal grain growth in hot working such that the reduction in yield and ultimate strengths can cause operational problems [11]. Usually, the abnormally large grains are distributed in thick sections of a piece where the strain is small. In hot working of Aluminum alloys, a critical deformation (i.e. %15) exists below which abnormal grain growth occurs. Additionally in large strains, the abnormal grain growth may also occur if the shear deformation is severe especially at lower sides of hot working temperature range. Furthermore, overheating in heat treatment can also cause excessive grain growth. Al doesn't possess any allotropic transformations; therefore refinement can't be directly driven by heat treatment unlike steels. Any refinement or coarsening happening in Al based materials is a result of recrystallization and growth. Consequently, the choice of the parameters and conditions of any thermo-mechanical processes applied to Al based alloys should be extremely careful, otherwise, adverse effects caused by excessive grain growth can easily ruin the performance of the material [11].

2-2-2 Recovery and recrystallization in AA7075

Due to high stacking fault energy and low self-diffusion energy (ease of dislocation climb and slip), recovery in Al and some of its alloys happens relatively effortless compared to other metals and alloy systems [23]. In fact, in many cases recovery takes place at the same time as deformation (so-called dynamic recovery) either when the strain rate is higher than 10^{-2} s^{-1} or temperature is above $\sim 300^\circ\text{C}$.

As an example of the effect of recovery on materials behavior, Mueller et al.[41] studied this phenomenon in AA7075 by cathodically charging the material with hydrogen or under vacuum in HCl environment. Fig. 2-10 shows that the electrochemically induced recovery (i.e. releasing the stored strain energy) [41] in tension of AA7075 results in and increase in ductility. Apparently in this case, instead of applying temperature, electrical energy provides the thermodynamic activation energy for recovery.

Several mechanisms have been proposed for recrystallization in aluminum alloys including discontinuous recrystallization, continuous recrystallization and geometrical recrystallization. Discontinuous recrystallization usually occurs in pure Al or its composites[11]. Continuous recrystallization and geometrical recrystallization are more common in aluminum alloys. As mentioned earlier, recrystallization involves nucleation and growth, which are functions of stored strain energy and the diffusion coefficient. The initial microstructure, process parameters, mode of deformation, temperature of deformation and rate of deformation are amongst the factors that affect the strain energy and also the diffusion coefficient. In Al-based materials, increasing the concentration of alloying elements (or generally impurities) results in a reduction of recrystallization temperature[11], possibly mainly due to blocking of dislocations along second phase particles. Additionally, the 7000 series have much lower stacking fault energy compared to pure Al, which makes the series (including 7075) more likely to recrystallize. Increasing the temperature of deformation also increases the severity of recrystallization in AA7075[11]. Dynamic recrystallization can severely occur in AA7075 even at low strain rates (if the processing temperature is high-enough).

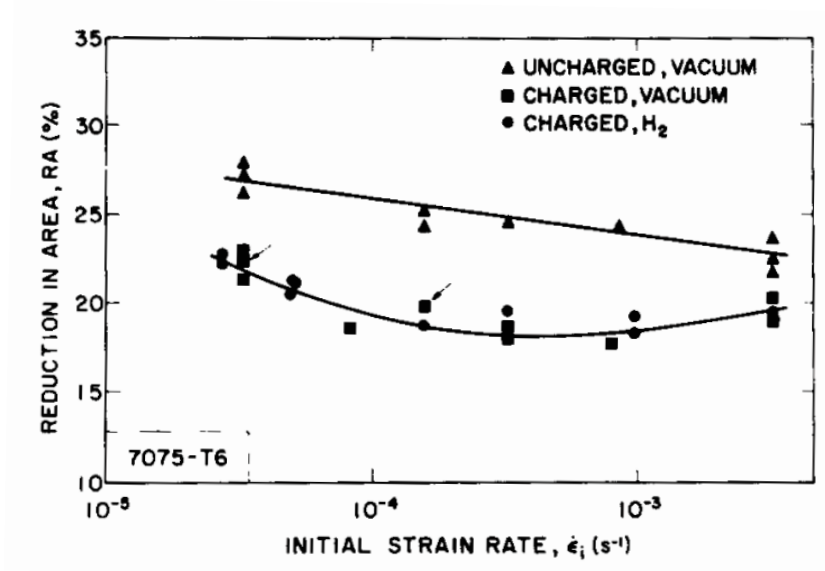


Fig. 2-10 Increase in ductility (i.e. increase in reduction area) in tension of AA7075 by electrochemically induced recovery[41]

As Fig.2-11 shows, Yang et al. [40] observed recrystallization in AA7075 in uniaxial tension tests at 773 K with strain rate of $2.9 \times 10^{-3} s^{-1}$ and the total strain of 160%.

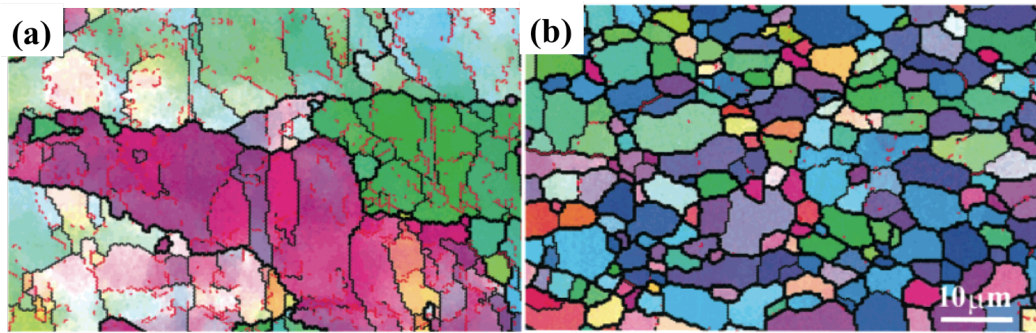


Fig. 2-11 (a) As-received and (b) recrystallized AA7075 obtained by high temperature tension tests[40]

2-2-3 Texture evolution in AA7075

Texture evolution in aluminum alloys is mainly due to rotation of the operative slip system towards the direction of the applied external force. It is believed that twinning has a little contribution to texture evolution of AA7075 [36, 42]. Existence of preferred crystallographic orientation results in anisotropy in properties such as elastic constants, thermal conductivity and so forth. Deep drawing, rolling and friction stir processing of AA7075, are the famous processes leading to development of preferred orientation in AA7075. Fig. 2-12 shows a severe texture evolution observed in accumulative roll bonding of AA7075 after 6 passes[42]. According to Fig. 2-12 (c), the change in the color of the grains demonstrates the texture evolution. As another example, Fig. 2-13 illustrates the pole figures showing the change in texture attributes of AA7075 caused by friction stir processing [43]. Early findings of this work on texture evolution of AA 7075 due to machining is also published in [44, 45].

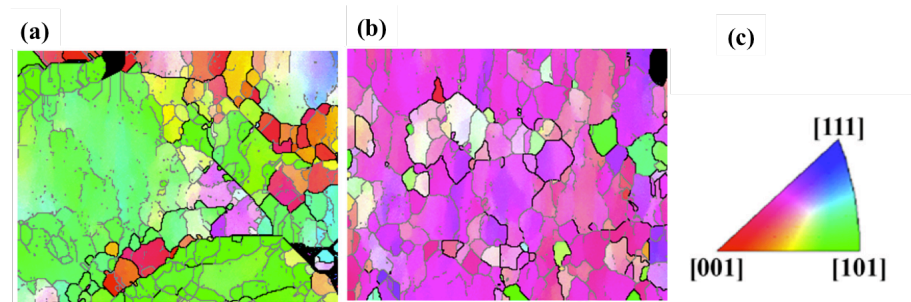


Fig. 2-12 Grains orientation in AA7075 after (a) 1 pass and (b) 6 passes of accumulative roll bonding. (c) shows the legend of grain orientation[42]

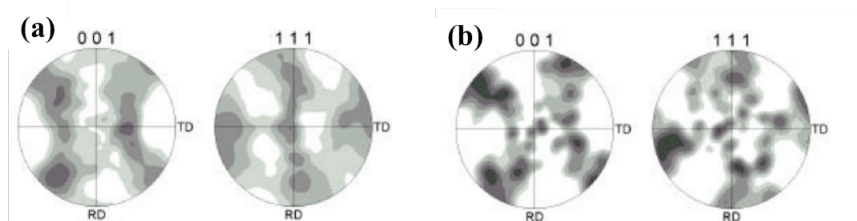


Fig. 2-13 Pole figures showing texture characteristics of (a) as-received and (b) friction stir processed AA7075[43]

2-2-4 Heat treatment and precipitation hardening in AA7075

In heat treatable Al alloys such as 7075, precipitation is possibly the most important microstructural phenomenon occurring in thermo-mechanical processing. Research on precipitation behavior of Al alloys started in late 19th century and now is more than 100 years old[37]. However, the recent scientific findings on the mechanisms and atomistic details of the process have lead to far better control over the type, shape, size and distribution of precipitates and consequently on properties and response of the product.

Precipitation-hardening occurs when the solubility of the secondary phases, an intermetallic in most cases, greatly varies with temperature. Heating the alloy to a sufficiently high temperature, dissolves all the secondary phases. This status is called saturated solid solution. Quenching from the high temperature of saturated solid solution retains the single-phase microstructure at lower (such as room) temperature. This status is called super-saturated solid solution. At the low temperatures, the secondary phases have a thermodynamic drive to form precipitates. The phenomenon of formation of precipitates from a saturated solid solution is called aging. Precipitation is a diffusional process and needs time and temperature to have a fast kinetics. As a result, depending on the alloy system, at room temperature no aging may occur, although the thermodynamic force is strong but the kinetics dictates zero rate for the phase transformation reaction[36]. In most cases (including 7075), heating at moderate temperatures is required to produce precipitates. For the case of 7075, several heat treatment processes are proposed and given names starting with “T”, standing for “temper”. For example the *T6* is the heat treatment process of holding the super-saturated solid solution alloy at 120°C for 24 hours. Table 2-2. lists the changes in mechanical properties of the non-tempered AA7075-0 (i.e. cooled down in equilibrium from saturated solid solutions) compared to the T6 tempering[36].

Table 2-2 Mechanical Properties changes in T6 tempering of AA7075[36]

	AA 7075-0	AA 7075-T6
Yield strength (MPa)	145	500
Ultimate tensile strength (MPa)	275	570
Elongation (%)	11	5

The mechanism of precipitate formation and the chemical composition of precipitates depend on the amount of alloying elements. The sequence of precipitate formation in 7075 alloy is as below[37]:



GP stands for GP zones taken from the names of two pioneer scientists, Guinier and Preston, who discovered the atomistic mechanism of formation of precipitates in Al alloys. The sequence of precipitation in 7075 is as follows [46]: GP zones aggregates with nanometer size start first. Selected area electron diffraction (SAED) is applied to differentiate the GP zones from the base material. Growth of GP zones will result in formation of η' precipitates. High-resolution transmission electron microscopy show that the GP zones and η' precipitates are highly coherent with the matrix. Further soaking at aging temperatures will lead to coarsening of η' precipitates which reduces the coherency with the matrix Al resultsing in formation of η precipitates which are believed to have chemical stoichiometry very close to $MgZn_2$. It is believed that GP zones and coherent or semi-coherent precipitates contribute to enhanced yield strengths. Mainly because the strain field caused by precipitation can hinder dislocation movements. However, the coarser more disperse distributed incoherent precipitates have less strengthening effects due to high average spacing between them. As a results over aging, can cause serious deterioration of properties in Al based alloys and is usually avoided[46]. Average size of η precipitates in AA 7075 depends on many factors including deformation history and

aging process; but values in the range of tens of nanometers to several microns are reported [36].

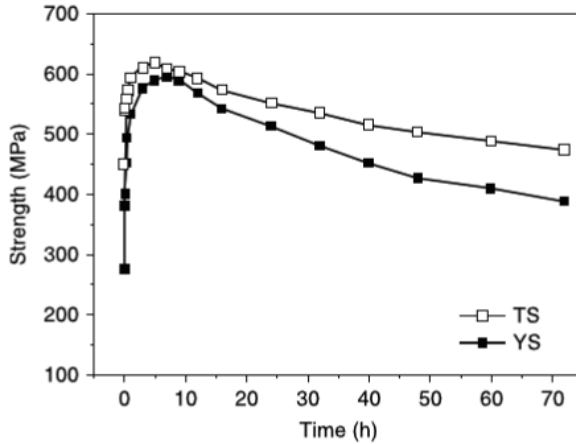


Fig. 2-Changes in strengths of AA 7075 as a function of aging time. TS and YS respectively show tensile and yield strength[10]

Fig. 2-14 illustrates the change in tensile strength of AA7075 as a function of aging time. The reason of strength reduction is believed to be coarsening of the precipitates (over-aging)[10]. Although the mechanical properties of aged AA7075 is lower than the peak properties obtained in initial stages of aging, there are reports in literature about improved stress corrosion cracking of over-aged AA7075 compared to peak-aged[10]. In addition to more traditional one-step temper cycles, two or three step temper cycles for AA7075 are also developed; a summary of treatment processes can be found in [36].

2-3 Summary

Researchers concur that recovery, recrystallization, grain growth, texture evolution and phase transformations are the most important first order microstructural evolutions occurring in processing of materials. Several experimental observations of the above phenomena in machining of different types of metals and alloys (such as Steel, Al-based, Ni and Cu alloys) were mentioned. However, even in experimental works without

any predictive modeling, the open literature misses a systematic study on determination of the effects of changing machining parameters on the trend of the incidence of the above microstructural evolution.

Aluminum alloy (AA) 7075 is mainly known as an “aerospace material” due its light weight and superior mechanical properties. AA 7075 possesses a relatively low stacking fault energy, which leads to ease of recrystallization compared to pure Al or other Al-based materials. Severe plastic deformation processes, such accumulative roll bonding, friction-stir processes or equi-channel angular pressing, are reported to stimulate significant changes in the texture and grain attributes of AA 7075. Additionally, this alloy system is heat treatable by precipitation-hardening process where precipitates nucleate and grow from a saturated solid solution. The size and distribution of precipitates have a remarkable role on the properties and performance of the material. Therefore, careful control of the heat treatment process as well as clear understanding of the deformation history are critical in achieving the desired properties of AA 7075.

3. THERMO-MECHANICS OF CUTTING

3-1 Forces in Orthogonal Cutting

In most industrial cases, cutting operations are three-dimensional and extremely complicated in terms of mechanical analysis. However, a basic understanding of the mechanics of cutting process can be obtained by first considering the simplest two-dimensional version of metal cutting, which is called “orthogonal cutting”. Fig. 3-1(a) demonstrates a 3D perspective of orthogonal cutting geometry. There is another form of two-dimensional cutting which is more complicated than orthogonal cutting. In this cutting geometry, the cutting tool is inclined with respect to the workpiece as depicted by Fig. 3-1(b). This type of cutting is called “oblique cutting”.

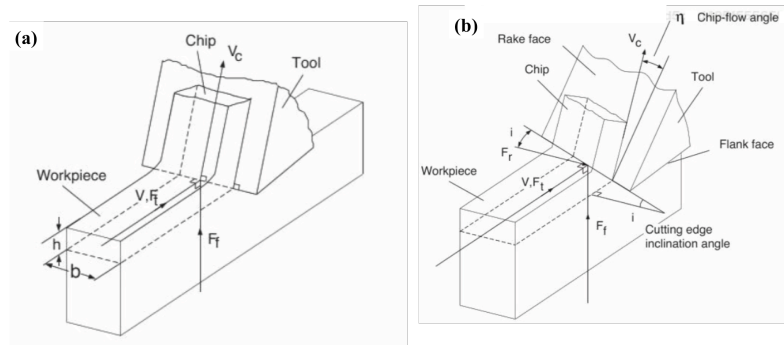


Fig. 3-1 (a) Orthogonal cutting and (b) Oblique cutting geometry[6]

For the sake of simplicity, the case of orthogonal cutting is considered for mechanics analysis. The cutting velocity is V , the cutting width is b and the depth of cut is h as shown in Fig.3-1 (a). The orthogonal cutting can be securely assumed as a plane-strain deformation by neglecting the deformation along the width of the workpiece [6, 47]. As a result, the cutting forces only act along the direction of the tool movement and chip thickness. These two force components are respectively called tangential (F_t) and feed force (F_f). As shown by Fig. 3-1(b), there is an extra force in oblique cutting acting along the radial direction of inclination of tool, which is called radial force (F_r).

Researchers believe that in orthogonal cutting, the deformation occurs at three different zones[47, 48] as illustrated by Fig. 3-2. Additionally, orthogonal cutting deals with two important angles, namely rake angle α_r , and shear angle ϕ_c .

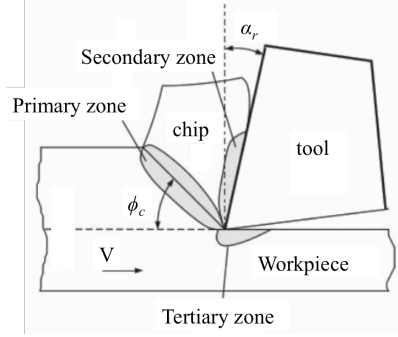


Fig. 3-2. The deformation zones in the cross-sectional view of orthogonal cutting. α_r and ϕ_c are the rake and shear angles respectively.

Several approaches have been proposed for analysis of mechanics of cutting. However, researchers categorize two of them as main toolsets for metal cutting analysis[6]. The first approach proposed by Merchant [49] assumes the primary zone is a thin plane and the second one proposed by Lee et al.[48] and modified by Palmer and Oxley[47] assumes the primary zone has a thickness. Here for the sake of simplicity and for the purpose of clarity of presentation, we follow Merchant's model. We additionally assume that the normal and shear stress, σ_s and τ_s , acting on the shear plane are constant. It can be shown that the shear force F_s , acting on the shear plane is related to tangential and feed forces [49]:

$$F_s = F_t \cos \phi_c - F_f \sin \phi_c \quad (3-1)$$

The normal force acting on the shear plane can be similarly written as:

$$F_n = F_t \sin \phi_c + F_f \cos \phi_c \quad (3-2)$$

The area of the shear plan is easily obtained as follows:

$$A_s = b \frac{h}{\sin \phi_c} \quad (3-3)$$

with the assumption of uniform stresses on the shear plane[6, 49] one can obtain the stress acting on the shear plane as follows:

$$\tau_s = \frac{F_s}{A_s} = \frac{(F_t \cos \phi_c - F_f \sin \phi_c) \sin \phi_c}{bh} \quad (3-4)$$

and

$$\sigma_s = \frac{F_n}{A_s} = \frac{(F_t \cos \phi_c + F_f \sin \phi_c) \sin \phi_c}{bh} \quad (3-5)$$

One important characteristic of cutting processes is the relatively high strain and strain rate of cutting processes compared to other conventional plastic deformation processes. In order to better analyze the strains in orthogonal cutting, a cutting diagram is shown in Fig. 3-3.

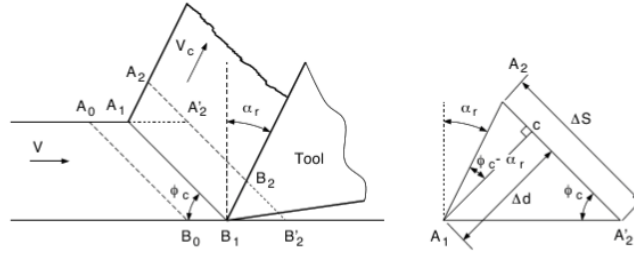


Fig. 3-3. Deformation diagram in orthogonal cutting[6]

According to Fig. 3-3, the shear strain γ_s is the ratio of deformation ($\Delta s = A_2'A_2$) over the nominal undeformed distance ($\Delta d = A_1C$). Simple rearrangement and noting to the geometry shown by Fig. 3.3 leads to:

$$\gamma_s = \frac{\cos \alpha_r}{\sin \phi_c \cos(\phi_c - \alpha_r)} \quad (3-6)$$

If one assumes an average shear strain (i.e. $\dot{\gamma}_s = \gamma_s / \Delta t$) and the velocity on the shear plane is $V_s = \Delta s / \Delta t$, then the shear strain rate can be expressed as:

$$\dot{\gamma}_s = \frac{\gamma_s}{\Delta t} = \frac{V_s}{\Delta d} = \frac{V \cos \alpha_r}{\Delta d \cos(\phi_c - \alpha_r)} \quad (3-7)$$

It is agreed that Δd is closely related to the depth of cut in orthogonal cutting and most of the time is within the range $0.15-0.2 \frac{h}{\sin \phi_c}$ [6, 47, 49]. Eq. (3-6) and (3-7) have an important significance: They link the shear strain and strain rate of cutting to the process parameters V and depth of cut, Δd . Such linkages are the foundation of the current thesis, which tries to connect the process parameters in machining to the loads which cause the microstructure to evolve.

In addition to the primary shear zone, one can also consider the secondary and tertiary shear zones. In both of these zones, a frictional force needs to be added to the force balance. In the secondary shear zone, the friction force acting on the rake face of the tool, F_u , can be written as:

$$F_u = F_t \cos \alpha_r + F_f \sin \alpha_r \quad (3-8)$$

F_v the normal friction force on the rake is:

$$F_v = F_t \cos \alpha_r - F_f \sin \alpha_r \quad (3-9)$$

then, μ_a , the friction coefficient between the sliding chip (if the movement of chip is assumed to be sliding only on the rake face) is:

$$\mu_a = \tan \beta_a = \frac{F_u}{F_v} \quad (3-10)$$

and the velocity of the chip V_c , is:

$$V_c = \frac{\sin \phi_c}{\cos(\phi_c - \alpha_r)} V \quad (3-11)$$

In the tertiary deformation zone, which is the zone that drives the microstructure evolution of the machined surface; two frictional forces act on flank face of the angle. Clearance angle is the angle between the flank face and the machined surface. The ratio

of the friction force on the flank face F_{ff} normal force on the flank face F_{fn} determines an average friction coefficient between the finished surface and the cutting tool.

$$\mu_f = \frac{F_{ff}}{F_{fn}} \quad (3-12)$$

There are several models to predict cutting forces[50, 51] as well as the shear angle[52], which are based on more complicated physical phenomena such as minimum energy principle or slip line force or other mechanistic assumptions[6]. There are several reports in literature on measuring and modeling the cutting forces in orthogonal or three-dimensional cutting. As an example, cutting forces in orthogonal cutting of AISI 1040 steel is measured as a function of cutting geometry (rake and clearance angles) and cutting speed[53]. Fig. 3-4 shows the cutting force as a function of the rake angle for velocity $V=150 \text{ m/min}$.

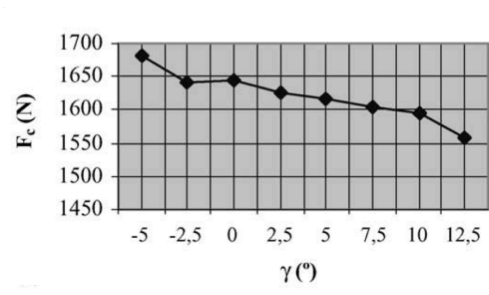


Fig. 3-4. Cutting force in AISI1040 steel as a function of rake angle γ [53]

As another example, Kishawy et al. measured the cutting forces in orthogonal cutting of AA7075 and compared to the mechanistic analytical model. Fig 3.5 shows that there is a good agreement between experimental measurements and analytical model of force prediction [54].

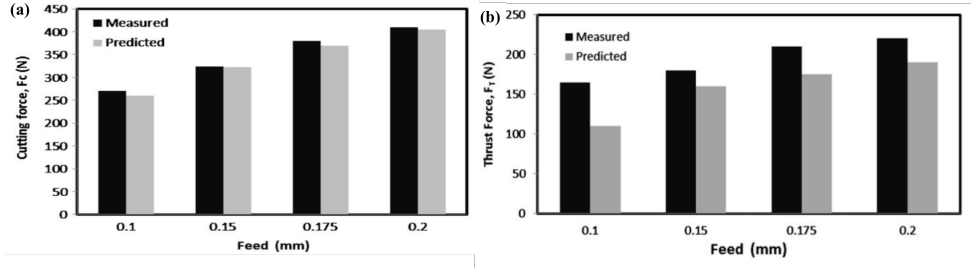


Fig. 3-5. (a) the cutting force and (b) the thrust force in orthogonal cutting of AA7075[54]

3-2 Temperature rise in orthogonal cutting

The temperature rise in orthogonal cutting is mainly due to friction between the cutting tool and the workpiece. The second contribution to the temperature rise comes from the plastic deformation occurring in shear zones[55-57]. For modeling purposes, it is usually desired to express the temperature rise and the heat flux in terms of cutting parameters such as the velocity and depth of cut and the geometry of cutting. Here, again for the sake of simplicity, the 2D orthogonal cutting is discussed first:

On the shear plane, the shear power, P_s , is converted into heat. The shear power is the inner product of shear force and velocity [6]:

$$P_s = F_s \cdot V_s \quad (3-13)$$

With the assumption that all the shear power is consumed to increase the temperature of the primary shear zone, one can write the conservation of energy as follows [6]:

$$P_s = bhV\rho C(T_s - T_0) \quad (3-13)$$

where C is the specific heat capacity of the workpiece material expressed in $J/kg^\circ C$. The first term, $bhV\rho$, is the mass removal rate, which has the dimension of kg/s . ρ represents the density of the material in kg/m^3 . T_0 and T_s are respectively the room temperature and temperature rise due to shear deformation and the rest of symbols are already defined. Experimental results point to the fact that the above formalism is over-estimating. Therefore, researchers proposed corrections to the above formalism[47]:

$$T_s = T_0 + \lambda_h (1 - \lambda_s) \frac{P_s}{bhV\rho C} \quad (3-14)$$

where λ_h ($0 < \lambda_h \leq 1$) and λ_s are correction factors respectively standing for the plastic work done outside the shear plane and the proportion of head that flows into the workpiece by conduction. Several empirical and semi-empirical equations have been proposed to account for the two above correction factors [58, 59]. Temperature rise in the secondary and tertiary shear zones have an additional frictional factor in addition to the plastic deformation. The total power is the superposition of shear and frictional power:

$$P_{tot} = P_s + P_u \quad (3-15)$$

The total power has to come from the velocity of cutting (V) and the powder due to friction has to come from the velocity of the chip V_c , obtained by equation (3-11).

$$P_u = F_u \cdot V_c \quad (3-16)$$

and

$$P_{tot} = F_t \cdot V \quad (3-17)$$

The principle of conservation of energy can be applied to the total power and it can be related to the temperature rise in tool and workpiece. Again, empirical and semi-empirical correction factors can be applied to the resultant equation to account for other physical phenomena that affect the temperature rise in cutting. Additionally much more complicated models have been proposed to predict the temperature profile in metal cutting processes [55, 56, 59]. Thermal cameras and thermocouples delicately attached to the tip of the cutting tools, are amongst the mostly used experimental apparatuses to measure the temperature profile in cutting processes[60]. As an example, Fig. 3-6 shows the temperature profile measure by IR thermal imaging in machining of Ti64 alloy[61]. Additionally, a large number of reports exist in the open literature on the analytical simulation of temperature profile in orthogonal cutting[60]. As an example, Campbell et al. [33] determined the temperature profile in orthogonal cutting of AA7075-T651 and

verified it by thermocouple experiments. They concluded reducing the rake angle and higher cutting speed increases the peak temperature at the tool and workpiece contact, as illustrated in Fig. 3-7.

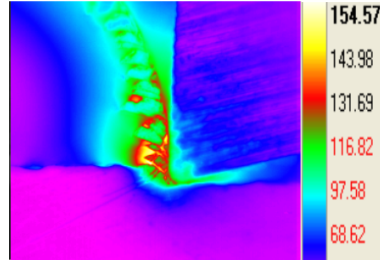


Fig. 3-6. Measurement of temperature profile in orthogonal cutting of Ti64[61]

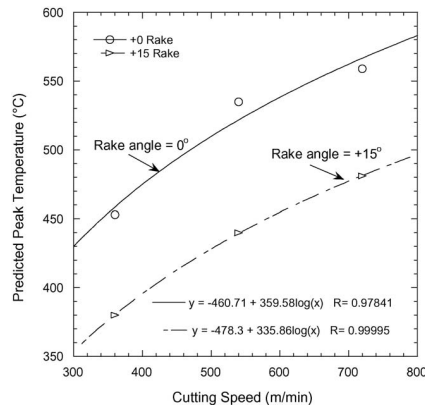


Fig. 3-7 Peak temperature prediction validated by experiments in orthogonal cutting of AA7075[33]

3-3 Turning

Turning is one of the 3D counterparts of the 2D cutting. In turning, a cylindrical workpiece is clamped in a chuck, which is rotated by a spindle. A single-point cutting tool, which is called the “insert” is held by a tool holder and does the material removal. Fig. 3-8 demonstrates a close view of the turning process showing the configuration of the insert, holder, chip and workpiece. Fig. 3-9 illustrates a schematic diagram of turning with notation of forces and other parameters.

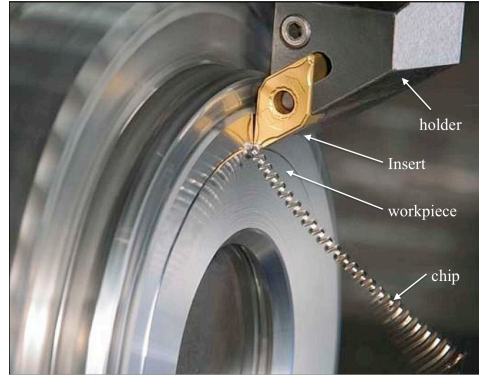


Fig. 3-8. A close view of turning process[62]

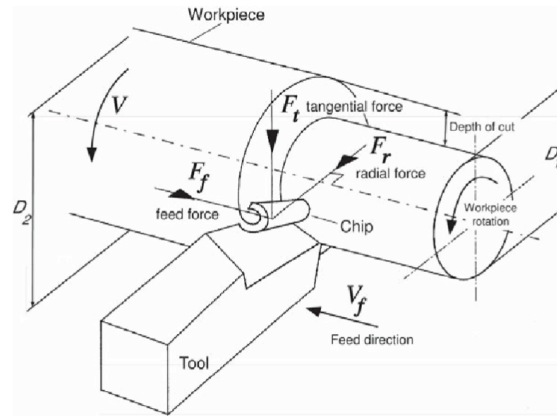


Fig. 3-9. A schematic diagram of turning process with notation of forces and other parameters[6]

Although there are similarities between orthogonal cutting and turning, the geometry of the three-dimensional orthogonal cutting is much more complicated. Fig. 3-10 schematically illustrates the geometry of the insert and tool holder. Compared to orthogonal cutting there are several important geometrical features in the inserts used for turning. The chip flows on the rake face of the tool [6]. Side rake angle is the angle between the rake face and the cutting edge and the back rake angle, is the angle between the tip of the tool and the line perpendicular to the workpiece [6].

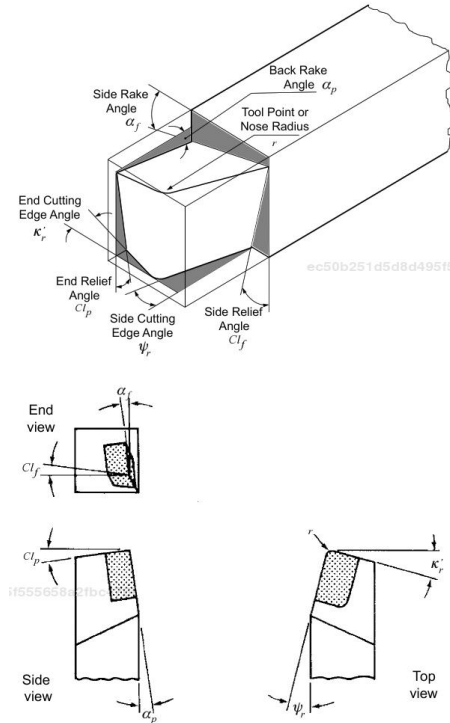


Fig. 3-10. Schematic of the geometry the insert in turning[6]

The simplest analysis of mechanics of turning is based on mechanistic approaches and needs to consider the manner of chip flow [63, 64]. A brief summary of the most simplified approach is mentioned here in order to show the linkage between mechanical and thermal loads applied to the workpiece and the geometry of cutting and also rest of process parameter in turning; namely the radial depth of cut D , the feed rate F , and the spindle rotational speed V . In standard chip formation in turning, at least two different regions in the chip can be recognized as schematically shown by Fig. 3-11(b). In region I, the chip thickness is constant. If the insert nose radius is represented by r , one can derive [6]:

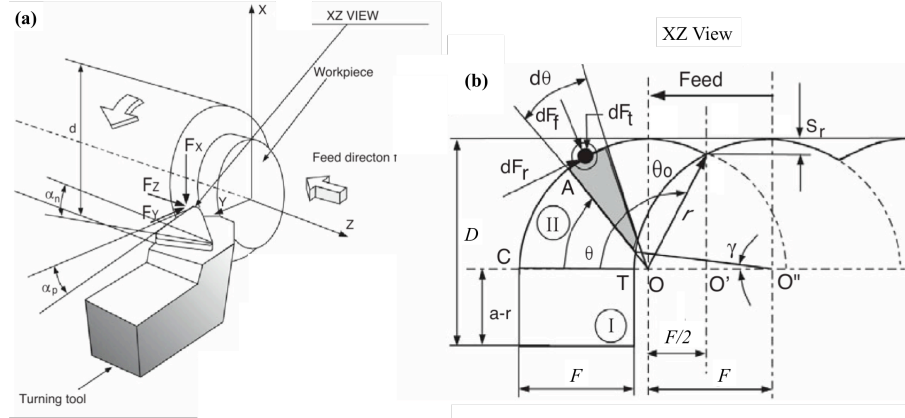


Fig. 3-11. (a) Notation of axes of coordinates and (b) schematic of standard chip formation in turning[6]

$$\begin{aligned}
 F_{xI} &= K_{tc} F (D - r) + K_{te} (D - r) \\
 F_{yI} &= K_{rc} F (D - r) + K_{re} (D - r) \\
 F_{zI} &= K_{fc} F (D - r) + K_{fe} (D - r)
 \end{aligned}
 \tag{3-18}$$

K_{tc} , K_{te} and etc. are so called “cutting constants” of the mechanistic approach to turning. Details of deriving these constants can be found elsewhere [6, 63, 64]; but they are closely related to cutting parameters and geometry:

$$\begin{aligned}
 K_{tc} &= \frac{\tau_s}{\sin \phi} \frac{\cos(\beta - \alpha) + \tan i \tan \eta \tan \beta}{\sqrt{\cos^2(\phi + \beta - \alpha) + \tan^2 \eta \sin^2 \beta}} \\
 K_{fc} &= \frac{\tau_s}{\sin \phi \cos i} \frac{\sin(\beta - \alpha)}{\sqrt{\cos^2(\phi + \beta - \alpha) + \tan^2 \eta \sin^2 \beta}} \\
 K_{re} &= \frac{\tau_s}{\sin \phi} \frac{\cos(\beta - \alpha) \tan i - \tan \eta \tan \beta}{\sqrt{\cos^2(\phi + \beta - \alpha) + \tan^2 \eta \sin^2 \beta}}
 \end{aligned}
 \tag{3-19}$$

where

$$\tan i = \tan \alpha_p \cos \psi_r + \tan \alpha_p \sin \psi_r
 \tag{3-20}$$

The rest of symbols have the same meanings as defined earlier for the case of orthogonal cutting.

In region II, where the chip area changes, the forces are calculated by integrating the following equations written in differential form. The integration should be performed over the curved chip segment [6].

$$\begin{aligned}
 dF_{xII} &= [K_{tc}(\theta)h(\theta) + K_{te}]r d\theta \\
 dF_{yII} &= -[K_{fc}(\theta)h(\theta) + K_{fe}]r \sin\theta d\theta + [K_{rc}(\theta)h(\theta) + K_{re}]r \cos\theta d\theta \quad (3-21) \\
 dF_{yII} &= -[K_{fc}(\theta)h(\theta) + K_{fe}]r \sin\theta d\theta + [K_{rc}(\theta)h(\theta) + K_{re}]r \cos\theta d\theta
 \end{aligned}$$

The angle θ in Fig. 3.11 can be safely assumed to be equal to ψ_r in Fig. 3-10 [6].

3-4 Temperature rise in turning

Compared to orthogonal cutting, turning requires more complicated thermal models if analytical derivation of temperature rise in turning is desired. Radulescu et al. summarized the reported analytical models for determining the temperature profile in the workpiece, tool and chip in turning [65]. In case of turning, the simplified energy balance models presented earlier for orthogonal cutting are shown to be very erroneous [6, 65, 66]. In order to more accurately predict the thermal flux and the temperature profile, the time dependent differential equations that govern the energy balance should be solved. The heat transfer equations at the contact point of the tool and the workpiece is [66]:

$$\frac{1}{r} \frac{\partial}{\partial r} \left(r \frac{\partial T(r,t)}{\partial r} \right) = \frac{1}{a} \frac{\partial T(r,t)}{\partial t} \quad (3-22)$$

where a is the thermal diffusivity and r is the radial distance at the tool tip. The second differential equation that needs to be solved is the heat flux equation[66]:

$$\Lambda(r,t) = -\kappa S(r,t) \frac{\partial T(r,t)}{\partial r} \quad (3-23)$$

where Λ , κ and $S(r,t)$ are respectively the heat flux, thermal conductivity and surface of integration. Several approaches are reported in the literature in order to solve the PDEs mentioned in the text. Komanduri et al. [55, 56] applied a so-called “moving heat source” model to account for the time-dependent nature of the heat flow in turning.

$$T = \frac{q}{2\pi\kappa} \int e^{-Vr \cos(\beta-\phi)} K_0 \left(\frac{Vr}{2a} \right) r d\theta \quad (3-23)$$

The temperature rise due to friction can be obtained by[55, 56]:

$$T = \frac{q}{\pi\kappa} e^{-Vr\theta/2a} K_0 \left(\frac{Vr}{2a} \right) \quad (3-24)$$

where q is the heat liberation intensity of the shear plane with the dimension of J/ms . Q is a function of cutting conditions such as the presence or absence of coolants, length of chip and tool contact and so forth [55, 56]. K_0 is a parameter emerging from the boundary conditions assumptions (infinite and semi-infinite solutions) as well as other geometrical details such as the manner of chip formation and flow, plastic deformation (in case of heat due to shear) and friction coefficients (in case of frictional heat) and depth of cut. The details of determining K_0 is reported in literature [55, 56].

As an example of modeling and experimental measurements in turning, the recent work published by Shihab et al. [67] on turning of AISI 52100 steel should be mentioned. Fig 3-12 shows the close agreement between measured and analytically modeled

temperatures at different experimental runs. In the 20 runs, the cutting speed was changed between 100 to 120 m/min , the feed rate was changed in the range of 0.1 to 0.22 mm/rev and the depth of cut was changed in the range 0.1 to 0.6 mm [67].

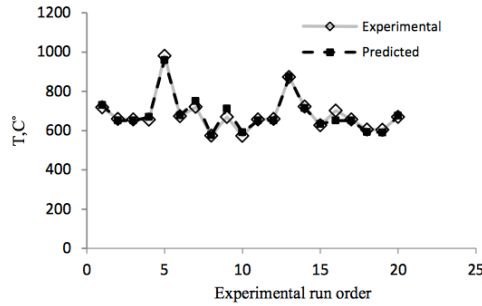


Fig. 3-12. Temperature measurement and analytical prediction in turning of AISI 5200 steel[67]

3-5 Experimental plan

In conducting the experimental work to capture the highly localized microstructural evolutions caused by machining, there are several issues that are easily encountered but not immediately obvious and therefore are very difficult to diagnose and resolve or avoid. A list of such possible pitfalls in capturing the microstructural evolutions during turning of AA7075 is as follows:

1. Exertion of thermo-mechanical loads in machining on the workpiece (not the chip) is undeniable, as confirmed by analytical closed-form solutions briefly described earlier. However, the assuring that the magnitudes of the loads are high enough to cause “tangible” evolution in the microstructure is not a straightforward task. In fact, a large number of machined AA7075 samples didn’t show a high-enough level of microstructural changes, mainly because the chosen magnitudes of turning parameters (i.e. V , F , D and the geometry of the insert and tool) were not high enough. In conclusion,
2. There are certain limitations on the on the maximal value of process parameters. For example, the spindle velocities higher than 5000 rpm are not possible with the

available lathe machines at the Georgia Tech shop. Or the depth of cut to values higher than a few millimeters are impossible to achieve in commercially available inserts and holders.

3. Electron back-scatter diffraction (EBSD) was the main characterization tool used in this work. EBSD is a surface characterization technique and requires a microscopically smooth and scratch-free surface for the best results. Sample preparation for EBSD involves in polishing the surface. If sample preparation step is not conducted with extreme care, there is a high chance that the machining-affected layer is completely removed, so no microstructural evolution compared to the as-received material is observable.

4. Even imposing the maximal microstructural evolution by maximal loads and making sure the preparation step doesn't ruin all the previous efforts may not lead to experimental observation. As previous reports emphasize, the effects of machining on the microstructure is very localized (depending on the material system and material history can be few microns), so choosing a correct microscopy tool with the correct lens is absolutely crucial.

5. The microstructural and mechanical history of the as-received material is also extremely important. Obviously if the starting material is already heavily deformed (and not tempered or annealed) there is very little room for a smaller-magnitude highly localized deformation to leave a noticeable impact on the microstructure.

Considering all the above points, a reduced-factorial two-level factor experimental plan is suggested to achieve the objectives mentioned in chapter one. 1-inch diameter Aluminum alloy 7075 rods were purchased from McMaster-Carr company. The chemical composition is mentioned in Table 2-1. Table 3-1 lists the mechanical properties of the material as provided by the manufacturer.

Okuma™ Spectrum LB2000EX was used to perform the turning experiments. Kennametal® CNMA 432-K68 negative insert with a nose radius, $R_e = 0.8 \text{ mm}$ was used

as the cutting device. This type of insert is a WC/Co unalloyed grade with minimal wear which is used for cutting hard and ultra-hard materials[68]. Fig. 3-13(a) shows a schematic of the turning insert. -5° rake angle Kennametal® MCGNR 164D tool holder was used to hold the insert. As mentioned earlier and based on the previous reports [6, 47] negative rake angles, exert higher forces to the workpiece and causes severe insert wear. That's why negative holders are occasionally used in industry and rake angles lower than -5° are not commercially available. Fig. 3-13 shows the geometry of the insert and the holder used in machining experiments. Table 3-2 lists the dimensional characteristics of the insert and the holder [68].

Table 3-1 Properties of the as-received AA7075[69]

Hardness (V)	175
Modulus of elasticity (GPa)	72
Yield Strength (MPa)	440
Ultimate tensile strength (MPa)	510
Elongation at break (%)	11
Solidus ($^\circ\text{C}$)	477
Liquidus ($^\circ\text{C}$)	635
Coefficient of thermal Expansion-linear at 25°C ($\mu\text{m}/\text{m}\cdot^\circ\text{C}$)	23.6
Thermal conductivity at 25°C (w/m-K)	130

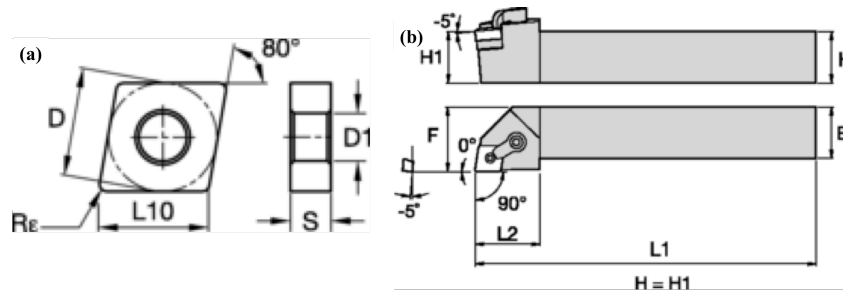


Fig. 3-13 Geometrical sketch of (a) Kennametal CNMA432-K68 insert and (b) Kennametal MCGNR-164D holder used in the turning experiments[68]

A reduced factorial experimental plan with two-level factors was used. Apart from the same tool and holder geometry (which causes the a very aggressive cutting), the other remaining factors to change are, the rotational velocity of spindle V , the feed rate F and

the radial depth of cut D . Table 3-3 itemizes the process parameters and the chosen levels.

Table 3-2 Dimensions of the insert and the holder used in experiments. The symbols are defined in Fig. 3.13 and the unit is millimeter[68]

D	D1	S	L10	R_g	H	F	B	L1	L2
12.7	4.76	5.16	12.9	0.8	25.4	31.75	25.4	152.4	31.75

Table 3-3 The changeable process parameters and the chosen low and high levels

	D (mm)	F (mm/rev)	V (rpm)
Low	1	0.01	200
High	3	0.8	5000

Noting Table 3-3, one realizes that even the lower depth of cut (1 mm) is extremely high compared to the usual values reported in literature [6]. Additionally, the higher-end feed rate and spindle velocity are significantly higher than the values usually reported in literature or industrially applied to manufacture parts.

The machined samples were mechanically polished by 180, 240, 320, 400, 600, 800 and 1200 grits. Then the samples, were polished by 3 and 1 μm colloidal diamond suspension and finally were fine-polished by 0.04 μm colloidal silica suspension. The last step of sample preparation was electropolishing by a Struers Lectropol-5 electropolisher machine under constant 25 V potential in a 40 ml perchloric acid/400 ml ethanol/ 400 ml distilled water solution for 1 min.

A TESCAN MIRA X3 FE-SEM equipped with EDAX-TSL EBSD camera was used to perform microstructural analysis. In EBSD investigations, machined surfaces (or in case of the as-received sample, a peripheral surface) were scanned in 2 μm steps. The

SEM was operated at 20kV with the beam intensity of $19 \mu A$ and a spot size of 68 nm . Fig. 3-14 schematically shows the geometry of experiments and the investigated region with respect to the machined surface. The collected EBSD data were cleaned up by “neighbor orientation correlation” procedure of EDAX-TSL OIM™ software package. The start of the clean up process was level 1 and ended at level 5. The methodology details of texture evolution modeling is explained in chapter 4.

Microhardness measurements were conducted by Buehler Tukon™ 1102 microhardness machine on the electropolished surfaces. The microhardness test was conducted under the ASTM E384 standard with a Vickers indenter under 2 kg of force. Each hardness test was repeated 5 times in order to make sure about statistical soundness of the results.

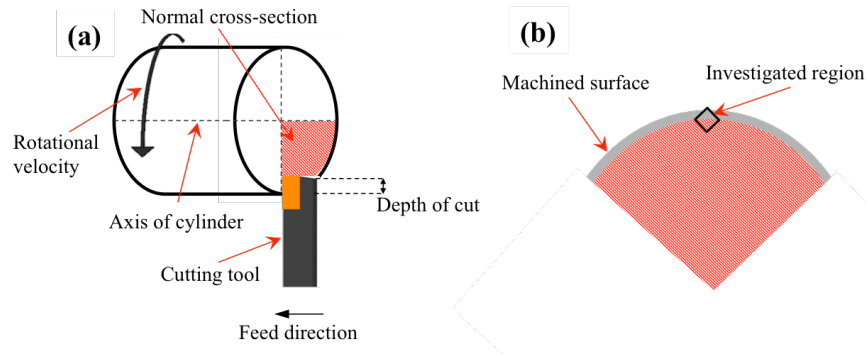


Fig. 3-14. (a) The schematic geometry of the turning experiments. The area hatched by the red color is the cross-section normal to the axis of the cylindrical sample. (b) The top view of the normal cross-section. The machined surface (gray color) and the region investigated by characterization tool are schematically demarcated

3-6 Finite element analysis

Finite element analysis (FEA) is an effective tool for solving a wide range of problems dealing with simultaneous high-order partial differential equations (PDE). In

most of the cases that FEA is applied, either the governing PDE can't be analytically solved or the geometry of the problem is very complicated that makes the application of boundary conditions impossible. Turning has both the characteristics. That's why in computational modeling of machining processes, FEA is the most widely used modeling tool in order to determine the thermo-mechanics of machining processes. In turning, FEA provides the unique capability of finding all the time-dependent mechanical and thermal entities such as stresses, strains, strain rates, temperature and etc. in the workpiece, chip and tool. FEA also provides the possibility of considering the frictional interactions between the tool and the workpiece.

One of the viable FEA software packages which is tuned for machining processes is the DEFORM™ Premier package developed by Scientific Forming Technologies Corp. The temperature-dependent stress-strain-strain rate model of Johnson-Cook type for AA7075 taken from [70]. The frictional parameters between the 0.8 mm nose carbide tool and AA7075 was taken from [29]. Similar to experiments, FE modeling was performed on a 25.4 mm diameter piece with the process parameters listed in Table 3-3. In order to save computation time, a 45° arc of the cylinder was only modeled. Fig. 3-15 demonstrates a schematic geometry of the analysis domain, the insert and the sample. The element size was varied based on the required accuracy of field variables. Fig. 3-16 shows the modeled arc and the cutting insert illustrating the mesh size variation as well as the insert in cutting action. The minimum element size is 100 μm and the maximum element is 1.2 mm with more than 11000 elements in the total assembly. Convergence analysis was performed in order to make sure the element sizes were chosen optimally.

ABAQUS™ version 6.13 was used as the FEA tool to obtain the results presented in chapter 7, where more details about the corresponding simulations are outlined.

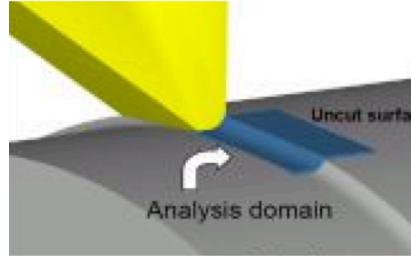


Fig. 3-15. Schematic demonstration of the insert, the uncut surface and the analysis domain; the image taken from [71]. A 45° arc of the 25.4 mm diameter piece was analyzed in this research.

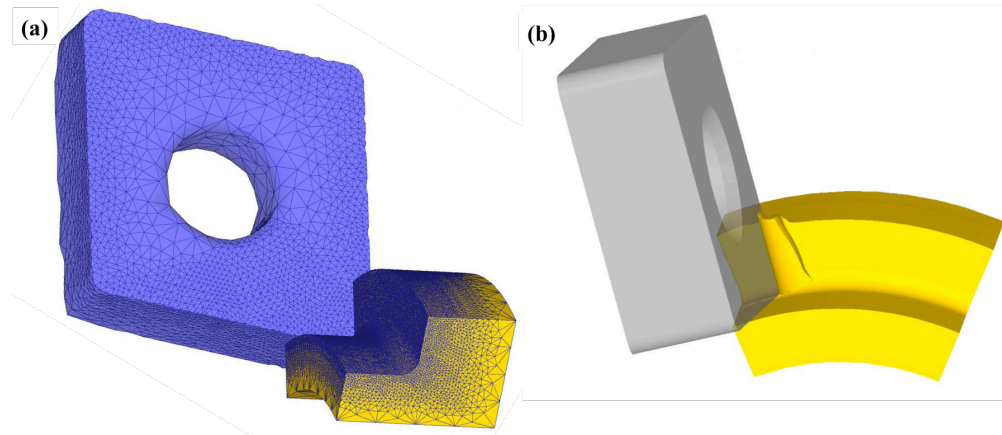


Fig. 3-16 (a) the insert (blue) and the simulated arc in turning of the AA7075 (yellow); the mesh size variation is also shown. (b) the insert (gray) in cutting action

3-7 Summary

The stress, strain, strain rate and temperature that a material experiences in a cutting process are direct functions of cutting parameters and the geometrical configurations of cutting process. Establishing such functional relationships is relatively straightforward for 2D simplifications of cutting processes. A 3D cutting action such as turning, requires more computational and numerical power for complete determination of the thermo-mechanics of the process. Finite element method is an accurate alternative to analytical cutting models. For a specific problem, the required computation power and time for FE modeling is usually more than most of the analytical approaches. However, FE method doesn't make the simplifying assumptions that are usually made in almost any

analytical model. In addition, FE provides numerical values of position and time dependent field variables where analytical models may have limitations in calculating.

Based on previous experiences in machining of Al-based materials, observable evolutions in microstructure do not occur unless the machining conditions are very aggressive. Considering this fact and along the guidelines provided in chapter 1 to achieve the objectives of this project, an experimental plan was designed and followed. Depth of cut, feed rate and spindle speed, with two low and high level values, were chosen as process parameters of this research work. Preparation of samples for microstructural characterization plays an important role in conducting experimental observations, since complete removal of the machining-affected layer below the surface is very likely if preparation steps are not performed with extreme care. All the experimental and post-experimental procedures were conducted according to established standards or conventions of the scientific community.

4. CRYSTALLOGRAPHIC TEXTURE EVOLUTION

4-1 Crystallographic Texture and Anisotropy

In crystallography, “texture” is defined as preferred orientation of crystallites in a polycrystalline aggregate[72]. There is a wide spectrum in the degree or intensity of texture, starting from a completely random orientation of grains to a fully textured aggregate, where “all” the grains are oriented along the same direction. Such a condition means that all the (hkl) planes in all the grains are parallel to each other. In nature, microstructures close to both ends of the spectrum (i.e. randomly oriented or fully textured) can be found [73]. One should note that a 100% randomly oriented microstructure is very unlikely to naturally occur or even synthesized in laboratory. Almost any so-called randomly oriented microstructure has a degree of inhomogeneity and non-randomness in the orientation of crystallites, but obviously microstructures very close to “theoretical” randomness are absolutely common; in fact the great majority of natural or synthesized crystalline materials are considered as randomly oriented. Thermo-mechanical processes such as heat treatment, rolling, extrusion and so forth can remarkably alter texture in metals.

The importance of texture in materials science stems from “anisotropy”. Properties (mechanical, thermal, magnetic, optical, chemical, etc.) of single crystals can be very different along different crystallographic directions. For example, rotation of axis of loading can lead to a %15 change, namely from 63 to 72 *GPa*, in the Young’s modulus of commercially pure Aluminum, [74]. The dependence of the Young’s modulus to the rotation of axis of loading in single crystal aluminum is shown in Fig. 4-1. As another example, Choudhuri et al. measured the speed of sound along different crystallographic directions of single crystal aluminum and reached to a 10.4% difference between $\langle 100 \rangle$ and $\langle 111 \rangle$ directions [75].

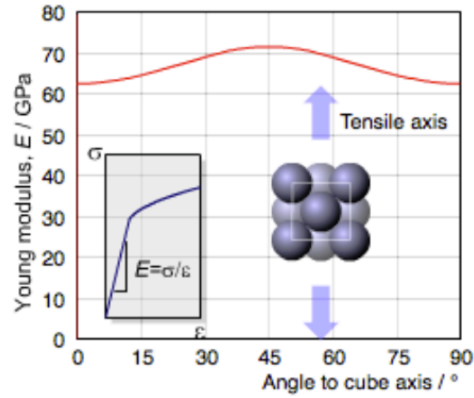


Fig. 4-1 The change in Young's modulus of Al single crystal as a function of rotation of axis of loading with respect to the single crystal orientation[76]

Anisotropy in Aluminum and its alloys is more pronounced in plasticity and plastic properties. Hosford studied plasticity of Al-4wt%Cu single crystals and concluded that there is a 25% difference in the level of stress in stress-strain curves of single crystals in plane strain compression as shown by Fig. 4.2 [77].

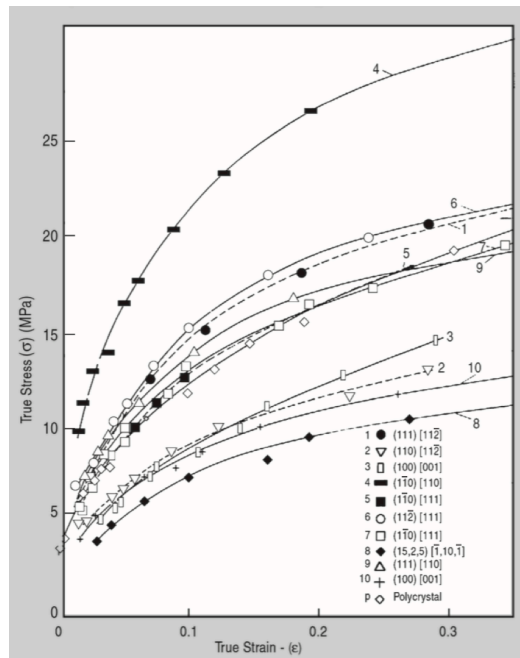


Fig. 4-2 Plane strain compression curves of Al-4wt%Cu single crystal along different crystallographic orientations [77]

The above examples, demonstrates the importance of texture analysis in materials, specifically because metals such as aluminum and its alloys are very prone to texture

evolution in thermo-mechanical processing (refer to section 2-2-3). Such significant differences in properties, which are caused by manufacturing processes, affect the processes in the first place and also can deteriorate performance or even lead to failure if not considered in the design steps.

The investigation of texture in materials can be generally categorized in two classes: macro-texture and micro-texture analysis [73]. Macro-texture deals with larger scale pieces of materials (*mm* length scale), like a rolled sheet of metal, and investigates the volume-averaged texture components in this length scale. Traditionally, X-ray diffraction has been used to perform macro-texture studies on materials[73]. On the other hand, micro-texture is the localized analysis of the texture in the order of μm or below. This type of analysis is specifically useful if the texture modification is localized and mostly occurs over a surface. Electron-back scatter diffraction (EBSD) is the main tool to analyze micro-texture[73, 78]. EBSD is an additional module that can be installed on scanning electron microscopes (SEM) to accommodate micro-texture investigations. If the analysis of texture is required in the nanometer scale, the transmission electron microscopy (TEM) counterpart of EBSD, which is called Precession Electron Diffraction (PED), can be applied. PED has the unbeatable capacity in texture analysis of grains in the order of 10 *nm* or below in size. If orientation of a single grain (regardless of size) is required (a single grain doesn't have anything to do with texture), selected area electron diffraction (SAED) capability of TEM should be used. Similar to EBSD cameras in the case of SEM, PED detectors can be added to TEM machines, while almost all the modern TEMs are equipped with SAED detectors.

4-2 Representation of texture

Position of any point in material space is determined by three components, usually noted by *x*, *y* and *z*. These components determine the distance of the point from a

“reference point” called the origin. x , y and z are the necessary movements along the Cartesian axes to get to the desired point from the reference point. Similar to position, “orientation” of objects in space can be determined by means of three components, which are called “Euler angles”. Euler angles are the necessary rotations about Cartesian coordinate axes, which can get to the desired orientation from a reference orientation. Unlike position coordinates, orientation coordinates (i.e. Euler angles) can be defined in more than one way [72]. In this work, we follow the notation chosen by Bunge [79]. In Bunge’s notation, the Euler angles are shown by φ_1 , Φ and φ_2 . Figure 1.4 demonstrates the definition of Bunge’s notation. In order to get to the desired orientation, φ_1 is the rotation about the z axis. Φ is rotation about the already rotated x axis which is shown by x' in Fig. 1-4. φ_2 is the rotation about z'' the axis (the z axis after the two previous rotations).

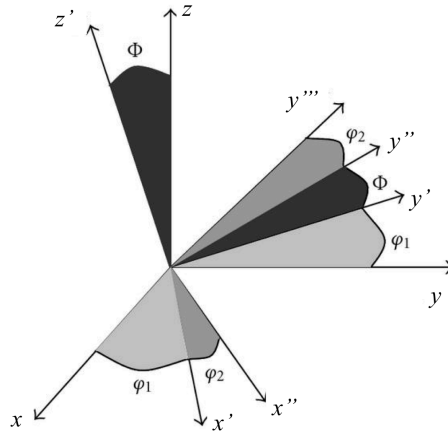


Fig. 4-3. Schematic illustration of Euler angles defined by Bunge's notation. Image taken from[80]

Similar to any object, the orientations of crystallites in space can be represented by Euler angles. The reference orientation is so-called the “sample” or “laboratory” frame and obviously should be kept constant in any texture analysis. The orientation coordinates of each crystallite, is called the “crystal” frame. In Bunge’s notation of Euler

angles, the range of φ_1 and φ_2 is $[0, 2\pi]$, while Φ in the $[0, \pi]$ range covers all the possible orientations.

Pole figures

In order to represent the degree or existence of a preferred orientation in polycrystalline aggregates, it is helpful to have a normalized intensity plot of certain crystallographic planes of all the crystallites with respect to three sample coordinate axes. “Pole figures” serve this purpose. Since, texture deals with orientations and angles, a stereographic projection is used in plotting pole figures. Fig. 4-4 shows a (111) pole figure in rolling of AA7075[81]. The three orthogonal sample directions are rolling direction (RD), transverse direction (TD) and normal direction (ND). In Fig. 4-4 ND is the center of the pole figure and RD and TD are denoted. Since the directions are orthogonal, the angular distance between the RD or TD and ND is 90° which is equal to the radius of the pole figure. The iso-intensity contours show the orientation of normalized population of the (hkl) planes, in this case (111), with respect to these three sample axes. The radii of the circle, as well as the quarter-circle arcs are graduated in 90° .

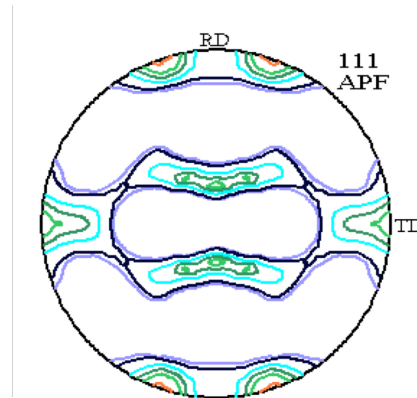


Fig. 4-4. (111) pole of figure of rolled AA7075[81]. The normal direction (ND) is the center of the pole figure

Inverse pole figures (IPFs)

In rolling and similar processes, the sample coordinate has three distinctive directions, which makes pole figures suitable means to demonstrate texture. If the process, involves with one important direction rather than three (such as extrusion or drawing), then the inverse pole figures (IPFs) are superior means to manifest texture. Additionally, if a surface is processed, again IPFs are more beneficial to represent texture since the normal to the surface can be considered as the single important direction of the IPF.

Machining belongs to this category, where a surface (either the machined surface or one surface normal to it) can be assumed as the primary surface of texture analysis. In inverse pole figures, the normalized populations of crystallographic planes in all the crystallite are shown as iso-intensity contours. Similar to pole figures, the stereographic convention of 90° radii and quarter-arcs holds true in determining orientations. Fig. 4-5 shows a complete inverse pole figure, typical of cubic crystals. There is no iso-intensity contour plotted on this image and therefore, it is not representing planes normal to a direction (or to a surface).

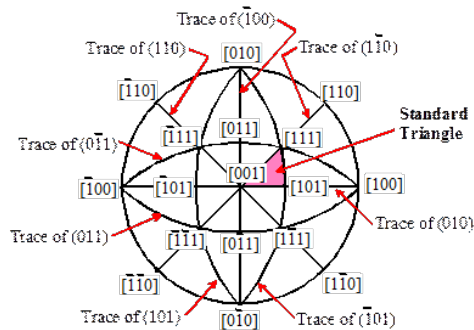


Fig. 4-5. A schematic of complete inverse pole figure of cubic materials. Each pole belongs to the certain plane labeled. Image taken from[82]

A complete IPF (such Fig. 4-5), looks like a pole figure. To differentiate, in presentation of IPFs, a pseudo-triangular portion, so-called “standard triangle”, confined by (001), (101) and (111) planes, is used. Related to inverse pole figures, the grain maps

obtained by EBSD also show the orientation of grains of the scanned surface with respect to the three crystallographic planes mentioned above. In other words, these maps show the orientation of the crystallographic plane of the grain at the surface with respect to the three planes above. Obviously, another direct application of such inverse pole figure maps is obtaining grain size and size distribution. Additionally, these maps can provide information on grain boundary characteristics. Fig.4-6 shows the IPF of the as-received AA7075 material. The intensities in pole figures are normalized to “theoretical randomly oriented” microstructures. This means the intensity 1 is the theoretical random. Intensities below 1 have no physical significance and only occur because of the necessities of numerical calculation of texture (will be covered in next chapters). The intensities higher than 1, demonstrate non-randomness. Fig. 4-6 shows that the as-received material is not completely randomly oriented, although very close. The maximum intensity on the as received IPF is ~ 2.3 and it occurs for the planes halfway between (001) and (111) which is (112) plane.

Fig. 4-7 exhibits the grain map overlaid by inverse pole figure of the as-received rod. There are two important parameters in determining the quality of EBSD scans, confidence index (C.I.) and image quality (I.Q.). C.I. is a measure of the success of the software to assign a (hkl) plane of the corresponding crystallographic system to each scan point. C.I. ranges between 0 to 1; where 0 means software has failed in determining the orientation of the point and 1 means a 100% match between the scan point and the theoretical crystallographic index. Due to atomic scale inhomogeneities, strains and residual deformations in grains and resolution limits of the detector and the SEM, C.I. values above 0.1 are accepted as reliable[78]. On the other hand, I.Q. provides a qualitative description of the successfulness of a scan without any significance of its absolute value. Thus instead of presenting the I.Q. in terms of a number, a gray-scale map similar to the colored orientation map is presented (e.g. Fig. 4-7(b)). A scan with high enough quality has an I.Q. map congruous to grain map. Because the scan at the grain

boundary points have lower quality (and also C.I.), so the grain boundaries appear darker on I.Q. maps. Comparing Fig. 4-7(a) and (b), one realizes that the scan of the as-received AA7075 had a high quality. The average C.I. of the scanned points was 0.42.

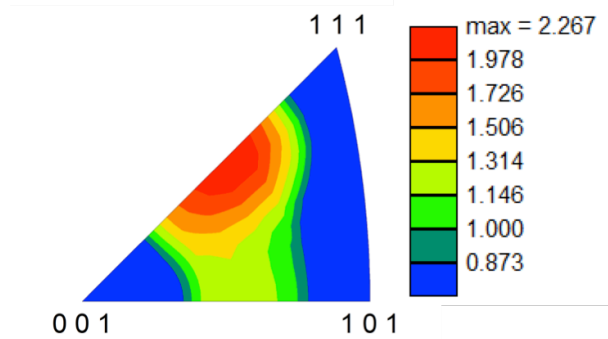


Fig. 4-6. The inverse pole figure (IPF) of the as-received AA7075 material

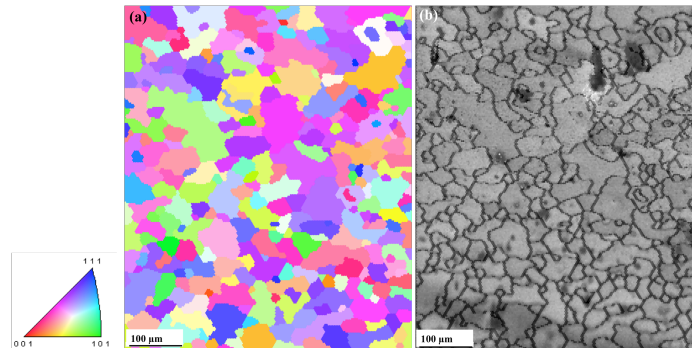


Fig. 4-7 (a) the grain and (b) the image quality (IQ) maps of the as-received AA7075. The average confidence index (CI) of the scan was 0.42.

In Fig. 4-7, a qualitative distribution of grain sizes can also be seen. There are large grains with equivalent diameter more than $150 \mu m$ and smaller grains with diameters around $10 \mu m$ are also visible. Next chapter delves more deeply into the evolution of grain size and size distribution.

ODF Plots and constant cross-sections

Inverse pole figures (and pole figures) provide a more qualitative description of texture. In order to fully describe the texture characteristic of a material, usually several of such figures are provided. Even providing multiple (inverse) pole figures can lead to an inevitable loss of some orientation data. Complete and quantitative portraying of texture is done through the “orientation distribution function” or ODF. The ODF is a probability density function, which yields the probability of finding a certain orientation g (i.e. $g = (\varphi_1, \Phi, \varphi_2)$) in a polycrystalline aggregate. The mathematical definition of the ODF, represented by f , is:

$$\frac{dV(g)}{V_{tot}} = f(g)dg \quad (4-1)$$

Where dg represents an orientation element. $dV(g)$ is the volume of crystallites having the g orientation (in the sample coordinates) and V_{tot} is the total volume of the polycrystalline body. Since f is a probability function, integrating f over the total volume of the material is equal to unity:

$$\oint f(g)dg = 1 \quad (4-2)$$

It can be easily shown that [79], $dg = \frac{1}{8\pi^2} \sin \Phi d\varphi_1 d\Phi d\varphi_2$ then one can rewrite eq. (4-2) as:

$$\int_0^{2\pi} \int_0^\pi \int_0^{2\pi} f(\varphi_1, \Phi, \varphi_2) \sin \Phi d\varphi_1 d\Phi d\varphi_2 = 8\pi^2 \quad (4-3)$$

Conventionally (and similar to intensity contours in (inverse) pole figures), the ODF is normalized to the “theoretical randomly oriented” polycrystal. Such an aggregate is assumed to have a constant intensity of 1 in the whole range of the three Euler angles. Any non-randomness in a material then represented by intensity above unity, the higher the intensity is, the further the orientation is compared to random. Such a conventions makes comparison of texture components in different materials possible. Computation of

ODF from experimental micro-texture data seems straightforward since volume (or equivalently the area on 2D images) of each crystallite and its orientation (i.e. $g = (\varphi_1, \Phi, \varphi_2)$) is known. Additionally, computation of the ODF from macro-texture data (i.e. pole figures obtained by X-ray diffraction) is also possible and the algorithms are explained elsewhere [73, 79].

It can be shown that Euler angles provide an orthonormal bases vector [79]. The ODF is a function of three arguments (i.e. $f = f(\varphi_1, \Phi, \varphi_2)$); therefore visualization of ODF requires four dimension, three for the arguments and the fourth one for the value of the function. One way of visualizing the ODF is plotting the iso-intensity contours of the ODF in the three-dimensional space of Euler angles. This way of presentation is exclusively the only way found in the reports of open literature. Fig. 4-9 demonstrates a hypothetical ODF in the 3D Euler space.

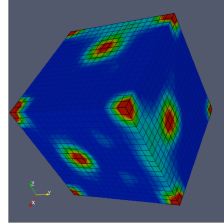


Fig. 4-8 A 3D representation of the ODF of a hypothetical material[83].

Symmetry in the crystallographic system reduces the necessary range of Euler angles to completely describe the ODF. Although pure geometrical consideration defines the range that mentioned earlier, symmetry dictates that a complete ODF for a cubic material is described in the range $0 \leq \varphi_1$ and $\varphi_2 \leq 45^\circ$ and $0 \leq \Phi \leq 72^\circ$ [79]. This region of the Euler space is called the “fundamental zone”. Out of the fundamental zone (in the full range of the Euler space) the ODF repeats itself. Each crystallographic system possesses a different fundamental zone [79]. Nevertheless, for the sake of presentation, the three axes of coordinates demarcate a range from 0 to 90° . In fact, this representation provides more

than enough data, still easier to plot and visualize. The ultimate goal behind plotting the ODF is obviously to observe the effects of different processes on texture as well as comparing the texture characteristics of different processes and different materials together. The normalized ODF, which is plotted in Fig. 4-8, can hardly achieve this goal. Complexity of the functional relationship of f of φ_1 , Φ and φ_2 , as well as existence of different intensity levels make understanding of texture difficult. Additionally, the inevitable plotting of the iso-intensity contours on the faces of the Euler space cubes, prevents visibility of the interior of the cube, unless only a selected intensity contour is plotted.

Therefore, for a clearer representation of texture and a faster qualitative and quantitative analysis, the normalized ODF is plotted in 2D contour maps at constant cross-sections of one the three Euler angles. Fig. 4-9 demonstrates the constant φ_2 cross-sections of the ODF of the as-received AA7075 material. The 0 to 90° range of φ_2 is sectioned at 5° intervals. Obviously for closer following of the 3D ODF plot, one can section at lower angle intervals; although sectioning the ODF by intervals below 5° is absolutely rare.

Looking at 4-9, one realizes that finding and following the occurrence of maximum intensities in the Euler space is much easier. As mentioned earlier, the 0-90° range for Euler angles represents too much information for cubic system. Along the same lines and in order to make interpretation of ODF much easier, it is common to consider even less cross-sections; specifically because important texture features in systems such as cubic (or even hexagonal) occur at certain φ_1 , Φ and φ_2 angles. In this work, a convention for face-centered cubic (FCC) system [73] is followed and constant cross-sections at $\varphi_2 = 0, 25, 45$ and 65° are presented. In addition to presenting the ODF in a Cartesian coordinate, a polar coordinate can be used to present iso-intensity contours of ODF as a function of three Euler angles. Then the cross-section of ODF at constant Euler

angles leads to pole figures. This way of representing texture is so-called “crystal orientation distribution” or COD.

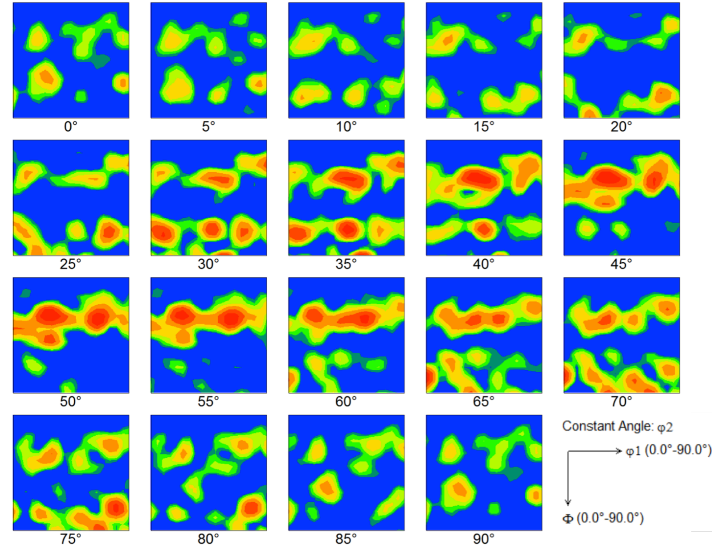


Fig. 4-9 Constant ϕ_2 cross-sections at 5° intervals of the ODF of the as-received AA7075

Texture Fibers

Texture analysis started with X-ray investigations of rolled metals and alloys. Researchers observed that for different materials (even belonging to the same crystal system), different points in the Euler space will show maximized ODF intensities after being rolled. In other words, rolling of Cu and Al (although both are FCC metals) will not necessarily lead to the same preferred orientation or ODF. These specific points with high intensity observed in the ODFs of different rolled materials are called “texture components” and each is given a name to designate. Table 4-1 summarizes the highly encountered texture components in rolling of Al and Al alloys[84]. It is important to note that almost all the texture components have several varieties occurring at different Euler angles [72, 84].

Table 4-1. Frequently observed texture componets in rolling of Al and Al alloys[84]. The Euler angles are expressed in degrees.

Texture component	φ_1	Φ	φ_2
Copper (C)	90	30	45
Brass (B)	59	34	65
S	35	45	0/90
Goss (G)	0	45	0/90

In many cases, a mixture of high intensities of several texture components exists in a material. Therefore, the texture is expressed by volume fraction of different components forming the texture characteristic of a material [85, 86]. Yet, the better way to express the texture attribute is through “texture fibers”.

A closer look at most of the ODFs reveals that the maximal intensities are continuous along orientation paths in the Euler space. These orientation paths (or orientation tubes) are so-called fibers. Fig. 4-10 schematically shows the two common fibers in rolling of FCC materials.

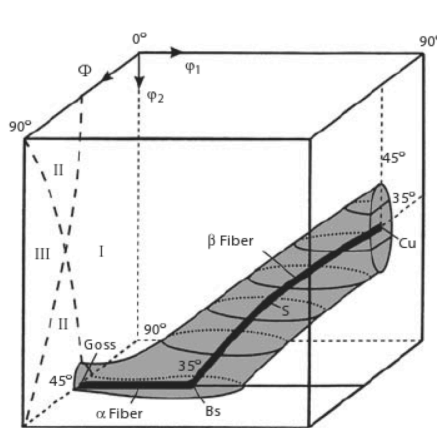


Fig. 4-10. Schematic illustration of α and β fibers[87]

The α fiber is the continuation from Goss component towards Brass component and the β fiber starts from Brass component and ends in Cu. In processes other than rolling, other fibers may occur in FCC metals as well. Table 4-2 lists the most common fibers of FCC metals with their start and end Euler angles.

Table 4-2. Most common FCC texture fibers with start and end Euler angles in degrees

Fiber Designation	Start			End		
	φ_1	Φ	φ_2	φ_1	Φ	φ_2
α	0	45	0	90	45	0
β	90	35	45	35	45	90
τ	90	0	45	90	90	45
γ	60	54.7	45	90	54.7	45

One can reduce the dimensionality in visualization of the ODF to only one dimension (compared to 2D cross-sections of the Euler space), by plotting the intensity of the ODF along fibers. This way provides a more feasible way for quantitative and qualitative comparison of texture though some details may be lost. Fig. 4-11 shows the α , β and τ fiber plots for the as-received material.

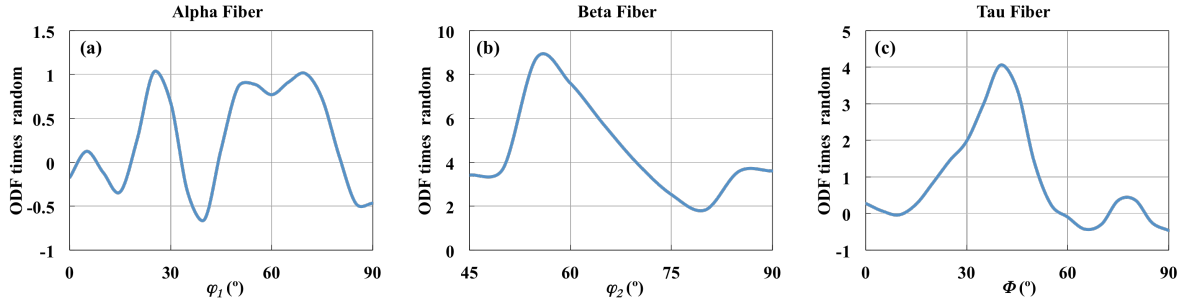


Fig. 4-11 (a) α , (b) β and (c) τ fibers of the as-received material

Fig. 4-11 is plotted with the normalization convention that the intensity of a randomly oriented sample is unity; so any part of the plot below has no physical significance. Additionally, small negative values may also show on the plot. Such values should also be neglected since a value can't be a negative times as much as a reference. The reason why such negative values appear on fiber textures will be explained in the next chapters. Fig. 4-12 shows that the probability of finding grains along the β fiber and where $\varphi_2 \approx 55^\circ$ is about 9 times of a randomly oriented material. Additionally, the probability of finding grains oriented along the τ fiber where $\Phi \approx 40^\circ$ is 4 times as much as a random sample. Comparing the three fiber textures of the as-received material, one

can conclude that the grains of the as-received material are more probable to be oriented along the β fiber where the minimum of the curve is at ~ 2 times random intensity. Such a behavior is reported for extrusion of Aluminum alloys [84, 88].

4-3 Modeling of texture evolution

As mentioned in chapter 2, thermo-mechanical processes change the orientation of grains. As an example, recrystallization process is believed to change the rolling texture to a mixture of C component and random orientation [23]. Similarly, inelastic deformation can impose a remarkable effect on texture. Slip and twinning are the top inelastic deformation mechanisms in crystalline materials. Experimental observations suggest that in FCC metals such as Aluminum, twinning is mostly suppressed and the major mechanism of inelastic deformation is slip [89-91]. “Slip” is the movement of dislocations on certain crystallographic planes along certain crystallographic direction (i.e. the Burgers[92] vector of the dislocation). The combination of slip plane and slip direction is called the “slip system”. Each crystal system possesses a different number of slip systems. In FCC crystals, the slip planes are the $\{111\}$ family and the slip direction is the $\langle 011 \rangle$ family [93]. Considering the different unique planes and directions in these two families, one concludes that FCC system has 12 slip systems. Table 4-3 summarizes the 12 slip systems of FCC lattice.

Table 4-3 The 12 slip systems of FCC crystal

Plane	(111)			Plane	$(\bar{1}\bar{1}1)$		
Direction	$[0\bar{1}1]$	$[01\bar{1}]$	$[\bar{1}10]$	Direction	$[011]$	$[101]$	$[1\bar{1}0]$
Plane	$(\bar{1}11)$			Plane	$(1\bar{1}\bar{1})$		
Direction	$[0\bar{1}1]$	$[\bar{1}0\bar{1}]$	$[110]$	Direction	$[011]$	$[10\bar{1}]$	$[\bar{1}\bar{1}0]$

The reason of changing the crystallographic orientation of grains in deformation by slip is explained by Schmid’s law [94]. It is thermodynamically preferable for crystals to orient the normal to the slip plane (\mathbf{n}) to the direction(s) of the externally applied loads

in deformation. Fig. 4-13(a) and (b), schematically show this phenomenon in uniaxial tension and compression. Activation of any slip system requires that the shear stress acting on the slip system reach a critical value, so-called the “critical resolved shear stress” or τ_{CRSS} .

The problem of capturing the changes in crystallite orientations in plastic deformation of a polycrystalline material is so-called “crystal plasticity”. Sachs[95] and Taylor[96] were the pioneer researchers tried to solve the problem. Sachs assumed that all the crystallites in the aggregate experience the same state of stress during all the steps of deformation. This simplifying assumption leads to violation of compatibility condition between grains [97, 98]. Taylor made a different simplifying assumption to avoid the compatibility issue. He assumed all the grains experience the same state of strain in plastic deformation [96]; but this assumption violates the equilibrium condition [97, 98].

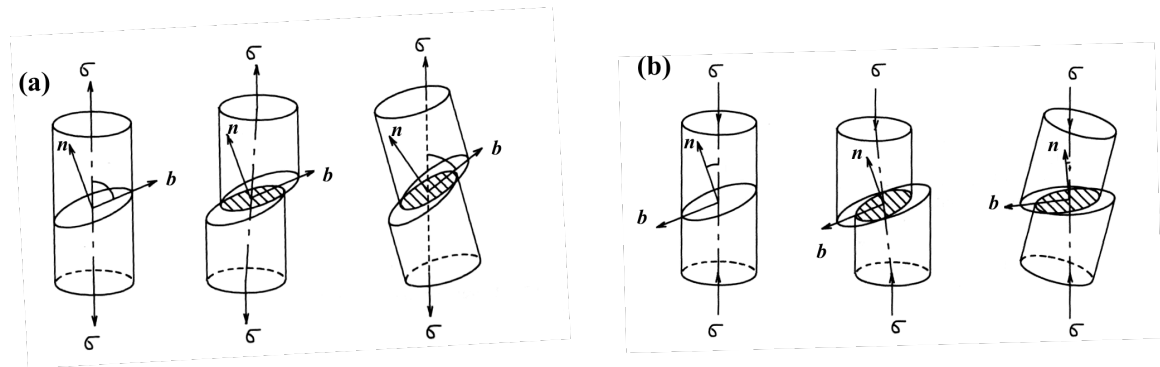


Fig. 4-12 Schematic illustration of crystal rotation in (a) uniaxial tension and (b) uniaxial compression. b denotes the slip direction[93]

During the past decades, a great deal of attention was paid to modifying Sachs- or Taylor-type models[99]. Furthermore, several other models were proposed by researchers[100, 101]. Followed by groundbreaking work of Eshelby[102] on obtaining the strain fields in ellipsoidal inhomogeneities embedded in solids, “self-consistent” approaches to solve the crystal plasticity problem were introduced [97, 103]. Self-

consistent methodology approximates each grain with an equivalent ellipsoid and replaces the rest of grains with an equivalent homogenized medium; where properties are obtained by the self-consistent homogenization method [104]. Then, following the formalism proposed by Eshelby, the strain and rotation fields in the ellipsoidal grain can be obtained. Therefore, activation of different slip systems can be captured and rotation of each grain can be determined. Ahzi et al. modified the self-consistent model to accommodate time-dependent large deformations [99]. Such schemes are called visco-plastic self-consistent or (VPSC) techniques. Lebensohn and Tomé were able to modify the available VPSC models to cover large visco-plastic deformations in non-cubic systems [105]. The research on more accurate, computationally inexpensive solutions for the crystal plasticity problem is still continuing. A good example is the statistical crystal plasticity scheme suggested by Garmestani et al. [106, 107]. In this work, we exploit the VPSC scheme. The computer code is available by the Los Alamos National Laboratory. The 6th version of the VPSC code written in FORTRAN was compiled and run with double precision by Intel® FORTRAN compiler (version 14.0.2) licensed to the Georgia Institute of Technology. The basis of the VPSC scheme is as follows:

The Schmid paramter m_{ij} , is the symmetric part of the tensor product of \mathbf{n} and the slip direction \mathbf{b} :

$$m_{ij} = \frac{1}{2}(n_i b_j + b_i n_j) \quad (4-4)$$

The strain rate in the crystal $\dot{\epsilon}_{ij}^c$, is assumed to have a power law relationship with the stress σ and the critical resolved shear stress τ_{CRSS} , of the crystal:

$$\dot{\epsilon}_{ij}^c = \dot{\gamma}_0 \sum_s m_{ij}^s \left(\frac{m^s : \sigma}{\tau_{CRSS}^s} \right)^n \quad (4-5)$$

The superscript s denotes the slip system and the summation is done over all the active slip systems. $\dot{\gamma}_0$ is a normalization factor and n is the rate-sensitivity exponent of the material. The VPSC scheme linearizes eq. (4-5) [99, 105]:

$$\dot{\epsilon}_{ij}^c = M^c (\dot{\epsilon}) : \sigma^c \quad (4-6)$$

where M^c is a rate dependent secant modulus. The same type of equation can be written for the equivalent homogenized medium [99, 105]:

$$\bar{\dot{\epsilon}}_{ij} = \bar{M} : \bar{\sigma} \quad (4-7)$$

The over-bar denotes the values for the medium. The self-consistent approach leads to [99, 105]:

$$\dot{\epsilon}_{ij}^c - \bar{\dot{\epsilon}}_{ij} = \bar{M}^C : (\sigma^c - \bar{\sigma}) \quad (4-8)$$

and

$$\bar{M}^C = n(I - S)^{-1} : S : \bar{M} \quad (4-9)$$

where S is the forth rank Eshelby tensor which is only a function of the shape of the ellipsoidal grain [102]. The spin (rate of rotation) Ω_{ij}^c of the crystal, which accounts for the crystallographic texture evolution can be found:

$$\Omega_{ij}^c - \bar{\Omega}_{ij} = \Pi : S^{-1} : (\dot{\epsilon}_{ij}^c - \bar{\dot{\epsilon}}_{ij}) \quad (4-10)$$

Π is the skew-symmetric forth rank Eshelby tensor [102]. The hardening behavior of the material is considered and used to update τ_{CRSS} during the process. The Voce hardening law [108] is used the code. The constitutive behavior of AA7075 can be obtained for each temperature through a Johnson-Cook model [70] and fitted into the Voce law. Eq. (4-11) presents the Jonson-Cook model:

$$\sigma = [A + B\epsilon_p^n][1 + C \ln \dot{\epsilon}] \left[1 - \left(\frac{T - T_{room}}{T_{melt} - T_{room}} \right)^m \right] \quad (4-11)$$

where A, B, C, n and m are materials constants with the values reported in [70]. Table 4-4 lists the material parameters. The reason behind using the Johnson-Cook model is its capability in incorporating the effects of high temperature, which are of prime importance in machining. In fitting the Johnson-Cook equation to Voce's law, the temperature obtained by FEM was considered in obtaining the Voce constants for each VPSC run.

Table 4-4 Material parameters for AA7075 reported by[70]

A	B	n	C	m
527	575	0.72	0.017	1.61

4-4 Micro-texture evolution in machining of AA7075

In addition to the material parameters, the VPSC code requires the loading inputs in form of the components of the velocity gradient tensor and total strain (equivalent strain) applied to the material in the process. As described in chapter 3, FEA was used to determine thermomechanical loads. As an example, Fig. 4-14 shows the equivalent strain and strain rate in a middle step during cutting operation under $D = 1 \text{ mm}$, $F = 0.01 \text{ mm/rev}$ and $V = 5000 \text{ rpm}$. D, F and V respectively stand for depth of cut, feed rate and spindle speed.

Fig 4-14 is snapshot showing two mechanical parameters at a frozen time. However, In order to completely capture the microstructural evolution in the whole duration of cutting, one needs to consider all the thermo-mechanical as a function of time. In order to achieve this, 10 material points with almost equal distance across the width of cut were used as benchmarks for obtaining the velocity gradient and total strains. Fig. 4-15 shows the chosen point. The data for theses points are captured for during the whole duration of the process as can be seen, the points don't go into the chip after the cutting operation passes the points; they are exactly located on the machined surface.

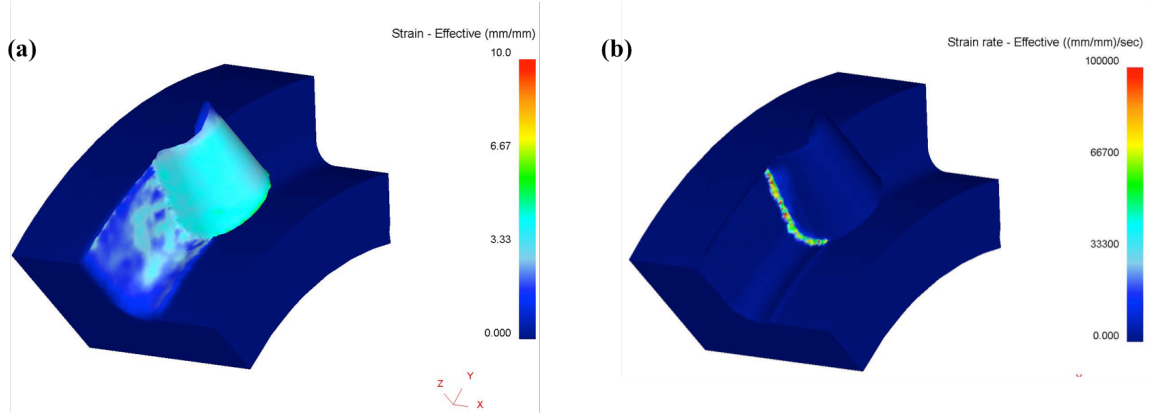


Fig. 4-13. (a) effective strain and (b) effective strain rate obtained by FEM for simulating machining at $D = 1 \text{ mm}$, $F = 0.01 \text{ mm/rev}$ and $V = 500 \text{ rpm}$.

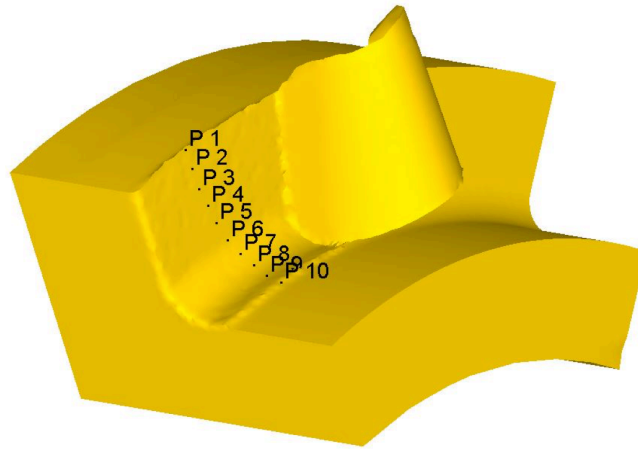


Fig. 4-14. The points in the workpiece chosen for extracting mechanical data necessary for running the VPSC code

Fig. 4-16 demonstrates the equivalent strain and strain rate obtained from the simulations of machining under $D = 1 \text{ mm}$, $F = 0.01 \text{ mm/rev}$ and $V = 5000 \text{ rpm}$.

The equivalent strain (or similarly the strain rate) is calculated by the following equation:

$$\epsilon_{eq} = \sqrt{\frac{2}{3} \epsilon_{ij} \epsilon_{ij}} \quad (4-12)$$

Fig. 4-16 shows that first of all, the values are very high; strain in the order of 5 or 6 and the strain rate in the order of 10^4 (1/s) . These orders of magnitude are common for

cutting and material removal operations [6] and are basically a sign of soundness of simulation and data report. Although these values are in the order of other reported values in literature, they are higher than most of the reports. This is because of the extremely aggressive cutting conditions chosen to maximally affect the microstructure of the material. In addition, Fig. 4-16 reveals that values of strain and strain rate for the intermediate points across the width of cut (i.e. points 4, 5 and 6) are higher than the rest of the points, although all the points have values in the same order. This doesn't seem to violate previous reports and analytical derivations of strains in metal cutting.

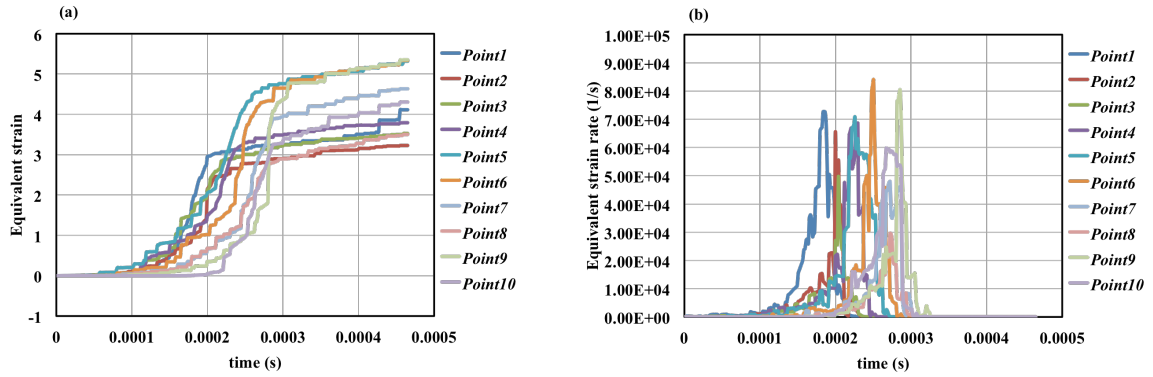


Fig. 4-15. FEA simulation results of (a) equivalent strain and (b) strain rate for machining under $D=1$ mm, $F=0.01$ mm/rev and $V=5000$ rpm. The 10 points are demarcated in Fig. 4-15.

In addition to material constants and crystal slip systems and the initial orientation of grains in terms of Euler angles; the full velocity gradient tensor and the total plastic strain of a deformation process are the two necessary inputs for the VPSC code to simulate rotation of grains. The DEFORM package doesn't calculate the velocity gradient directly. However, since the position and velocity components can be extracted as a function of time, velocity gradient can be numerically calculated. In calculation of the velocity gradient, the correctness check is the inelastic incompressibility:

$$v_{i,i} = 0 \quad (4-13)$$

where v_i is the component of the velocity and the $,i$ notation denotes partial differentiation with respect to x_i (i.e. x , y or z). According to Fig. 4-16, maximal strains and rates occur at points 4,5 and 6; therefore an average value for all the velocity gradient components of these points is determined and plotted in Fig. 4-17.

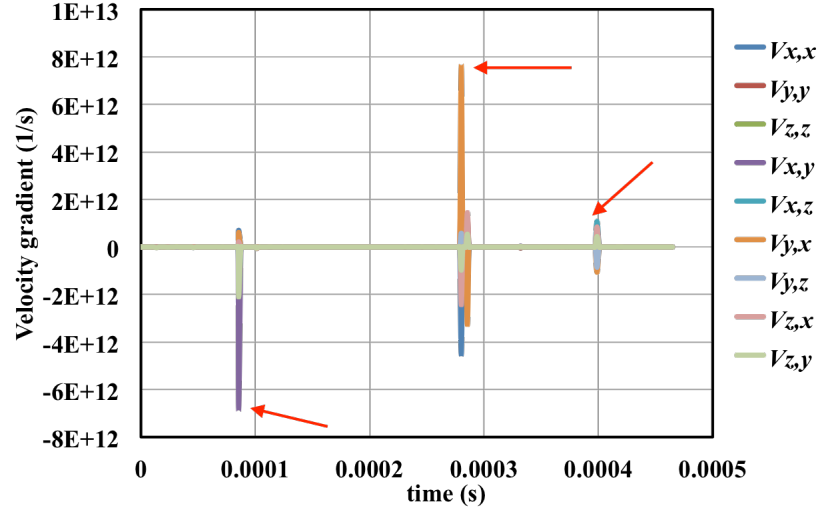


Fig. 4-16 The full velocity gradient tensor for average of points 4, 5 and 6 of Fig. 4-15. The red arrow shows the time steps that these point experience non-zero velocity gradient

According to Fig. 4-17, in the duration of cutting, at three distinctive time steps, these three points experience a non-zero velocity gradient, which is marked by red arrows; although the strain, strain rate and velocity components can be non-zero during these time steps. Fig. 4-17 shows that in turning, a complicated load is applied to the material, which is far from 2D plane strain simplification. (Plots not shown here but plane stress assumption is also not valid for turning). In addition to the main diagonal components of the velocity gradient tensor (i.e. $v_{x,x}$, $v_{y,y}$ and $v_{z,z}$), the shearing components namely $v_{y,x}$, $v_{z,x}$, $v_{x,y}$ and $v_{y,z}$ are non-zero and have values in the order of the diagonal components. Fig. 4-18 demonstrates that the incompressibility condition is acceptably satisfied for the velocity gradient components plotted in Fig. 4-17.

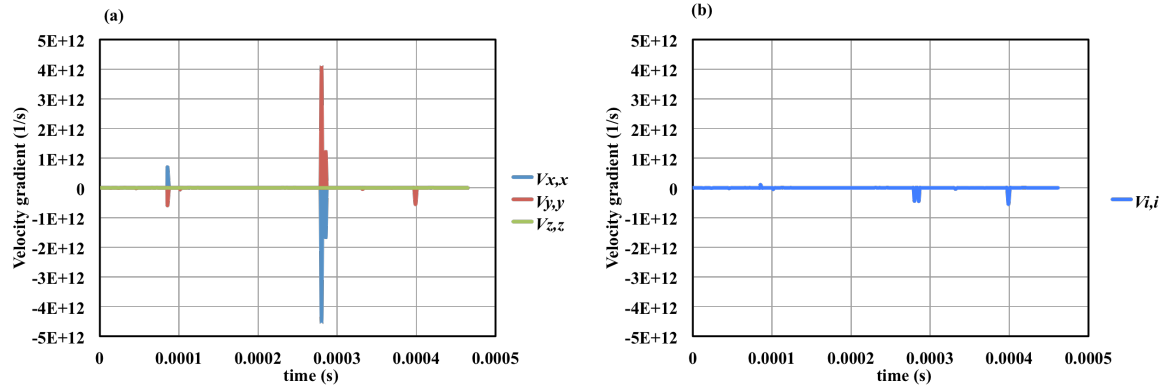


Fig. 4-17 (a) The diagonal components of the average velocity gradient tensor for points 4, 5 and 6 of Fig. 4-15 under $D=1\text{ mm}$, $F=0.01\text{ mm/rev}$ and $V=5000\text{ rpm}$. (b) Checking the incompressibility conditions.

As shown by Fig. 4-18 (a), the average diagonal components have values with the almost same magnitude but different signs. Fig. 4-18 (b) illustrates the acceptable satisfaction of the incompressibility condition. Interestingly is $v_{z,z} \approx 0$ while according to Fig. 4-17, at least one of shear velocity gradients acting on yz and zx planes are non-zero. The VPSC code considers hardening of material. Therefore, three separate runs for the three deformation impacts shown by the red arrows in Fig. 4-17 would lose the hardening effects of the previous runs. So, all the components of the three impacts were superimposed and one VPSC simulation were run for each sample. In other words, it was assumed that all the deformation occurred at once. Considering the time scale of Fig. 4-17, (ten thousandths of a second); this simplifying assumption seems valid.

As will be explained in chapter 5 (and can be seen in Fig. 5-4), the depth $200\text{ }\mu\text{m}$ below the machined surface can be safely chosen as the depth below which our characterization instruments can capture no microstructural phenomenon. Therefore, all the following micro-texture analyses are extracted from this area. Fig. 4-19 and 4-20 compare texture characteristic the obtained by experiments after machining and FEA and VPSC simulations.

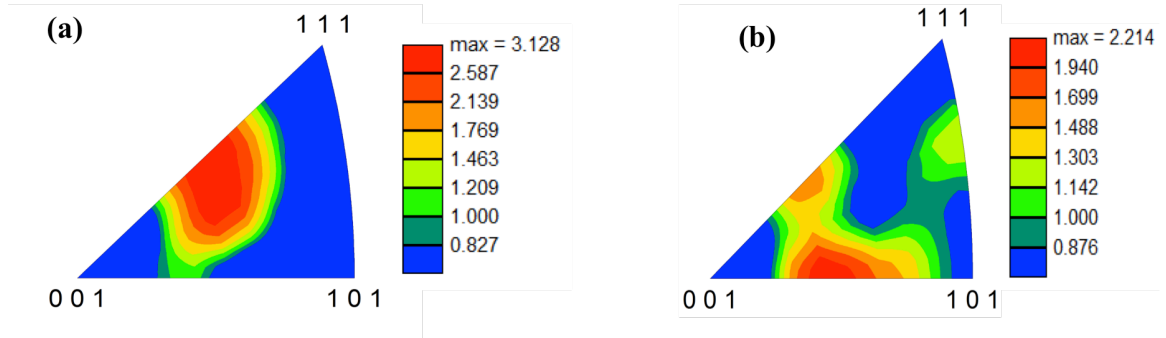


Fig. 4-18 (a) Experimental and (b) computational IPF for machining at $D=1\text{ mm}$, $F=0.01\text{ mm/rev}$ and $V=5000\text{ rpm}$.

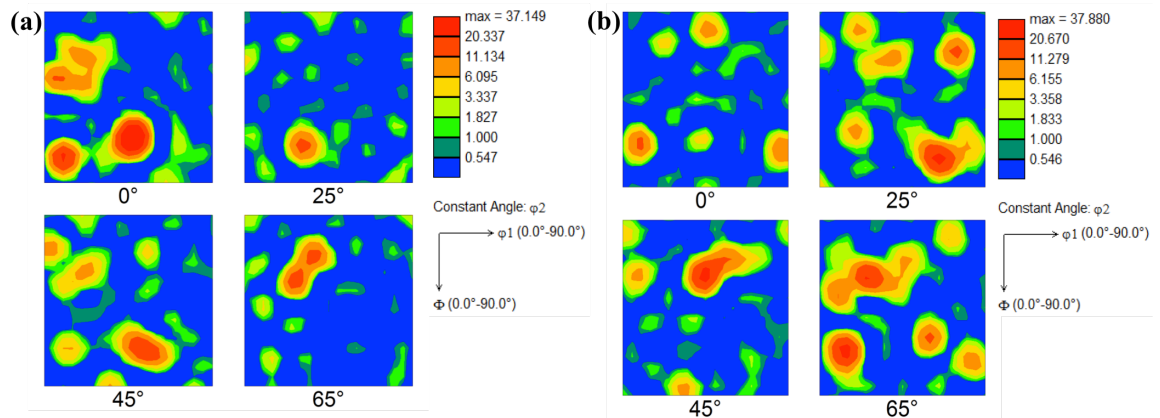


Fig. 4-19 (a) Experimental and (b) computational ODF for machining at $D=1\text{ mm}$, $F=0.01\text{ mm/rev}$ and $V=5000\text{ rpm}$.

Obviously, the input to both experiments and modeling effort were the initial as received material (Fig. 4-9) or its texture attributes. According to Fig. 4-19(a) the preferred orientation of the material machined under $D = 1\text{ mm}$, $F = 0.01\text{ mm/rev}$ and $V = 5000\text{ rpm}$ is the same as the as-received material shown in Fig. 4-6, both materials show a (112) preferred orientation. The maximum intensities in both samples are close to randomly oriented material, although there is a slight difference (an increase in machined sample) in the intensity. This change or a portion of it, can be also due inhomogeneities within the materials. On the other hand, comparing Fig. 4-19 (b) to 4-19(a) reveals that computer simulations of texture evolution, predicts a change in the preferred orientation towards (102) direction or planes with similar Euler angles. Nonetheless, the predicted

intensity, 2.214, is still quite close to random configuration. The reason behind this discrepancy in the predicted and experimentally observed texture is explained in the next chapter where possible recrystallization or grain growth is investigated. As mentioned earlier, the ODF can provide a complete qualitative and quantitative comparison of texture. According to Fig. 4-20 (a) and (b), the prominent texture component in the full range of Euler angles is different in the experimental and simulation results, although the maximum intensities are very close. None of the two cases (and neither the initial material shown in Fig. 4-9) show any strong texture component listed in Table 4-1, therefore texture fibers are the only remaining means to compare and analyze the ODFs.

Fig. 4-21 compares the three most common FCC texture fibers for the machined and simulated AA7075. From Fig. 4-12, the texture fibers of the initial material, we concluded β and τ fibers are more prominent compared to α . Fig. 4-21 shows that both experiments and simulations follow the same trend for the machined sample.

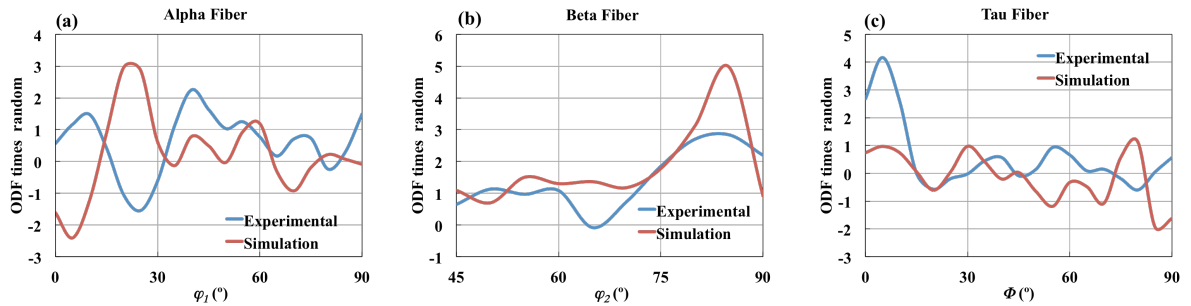


Fig. 4-20. Comparison of (a) α , (b) β and (c) τ fibers for machining and simulations under $D=1$ mm, $F=0.01$ mm/rev and $V=5000$ rpm.

For the case of machining, interestingly both simulation and experiment predict the same trend in the β fiber, which happens to remain the most noticeable in the material. Though, simulations predict that the intensities along the α fiber increase and reduced along the τ fiber.

Increasing the depth of cut to 3 mm (while keeping F and V constant at 0.01 mm/rev and 5000 rpm respectively) significantly increases the total strain, which is in accord with literature[6]. Fig. 4-22 demonstrates the average equivalent strain and strain rate for points 4, 5 and 6 across the width of cut, for 1 and 3 mm depths of cut.

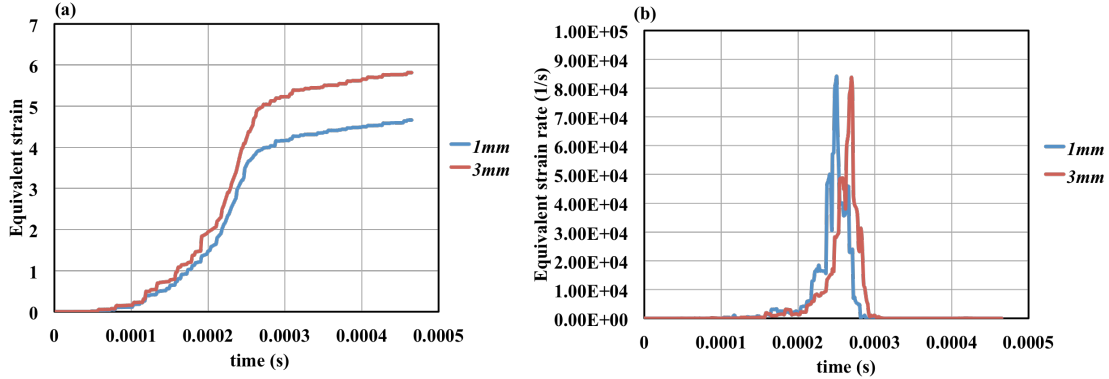


Fig. 4-21 Comparison of (a) equivalent strain and (b) equivalent strain rate for 1 and 3 mm depths of cut. F and V were respectively 0.01 mm/rev and 5000 rpm for both of the cases.

Based on Fig. 4-22, a 3 fold increasing the depth of leads to a ~24% increase in the average equivalent strain to the high value of 5.77. The shape and the maximum value of the strain rate curve remains similar but apparently increasing the depth of cut causes the maximal values of the equivalent strain rate occur half a ten thousandths of a second later, in cutting operation.

Similar to the case of 1mm depth of cut, all the components of the averaged velocity gradient tensor for the three middle points and the Euler angles of grains of the as-received material were input to the VPSC code. Additionally, EBSD experiments were done on the sample machined under the above conditions. Fig. 4-23 and 4-24 compare the experimental and simulation results of texture evolution under $D = 3$ mm, $F = 0.01$ mm/rev and $V = 5000$ rpm.

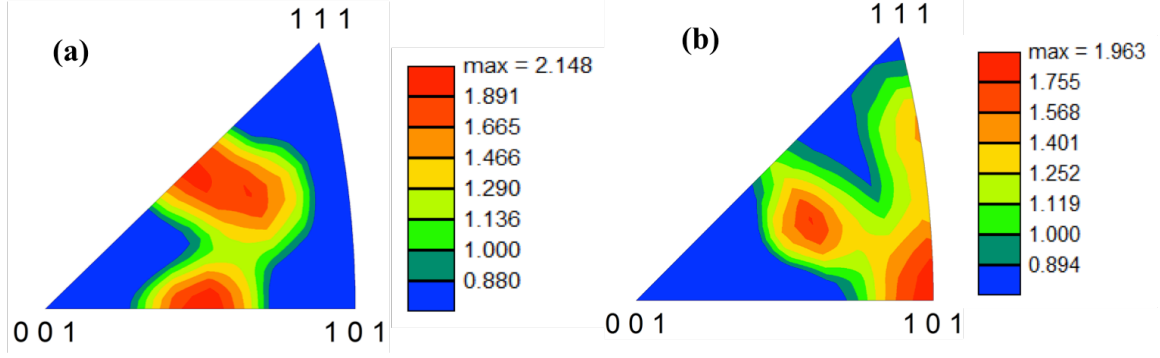


Fig. 4-22 (a) Experimental and (b) computational IPF for machining at $D=3$ mm, $F=0.01$ mm/rev and $V=5000$ rpm.

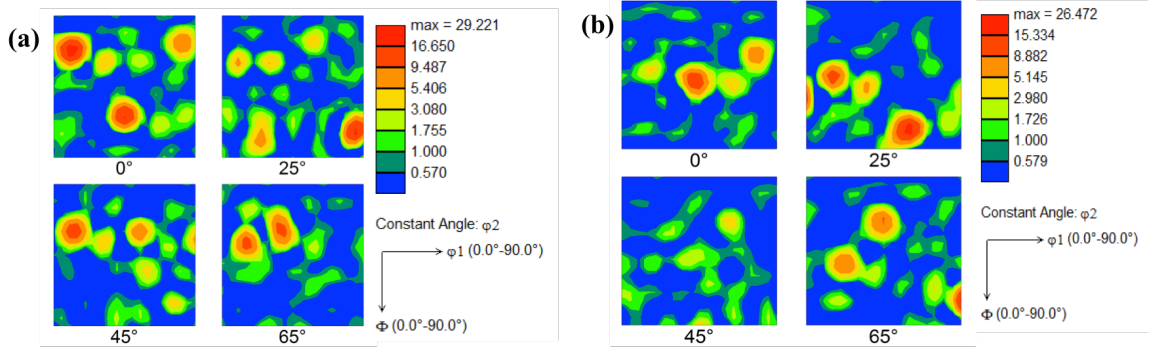


Fig. 4-23 (a) Experimental and (b) computational IPF for machining at $D=3$ mm, $F=0.01$ mm/rev and $V=5000$ rpm.

Fig. 4-23 (a) shows that the increased equivalent strain (compared to Fig. 4-19(a)) caused by the increased depth of cut leads to dual prominent orientation in the IPF. Although the initial (112) planes still show high intensities, another orientation of high intensity (102), is starting to emerge. Fig. 4-23(b) resembles Fig. 4-23(a) in terms of dual high intensity of the IPF. Though, it seems that the simulations predict a slightly different orientations compared to the experiment. i.e. $\sim(214)$ and (101) instead of (112) and (102). Looking at the ODFs presented by Fig. 4-24, one realizes there are several points of match between modeling and measurements. Texture components close to $(\varphi_1, \Phi, \varphi_2) \approx (45^\circ, 0^\circ, 65^\circ)$, $(90^\circ, 25^\circ, 75^\circ)$, $(65^\circ, 45^\circ, 35^\circ)$ and $(45^\circ, 65^\circ, 30^\circ)$ are common between the two cases. Texture fibers are compared in Fig. 4-25 for a deeper comparison.

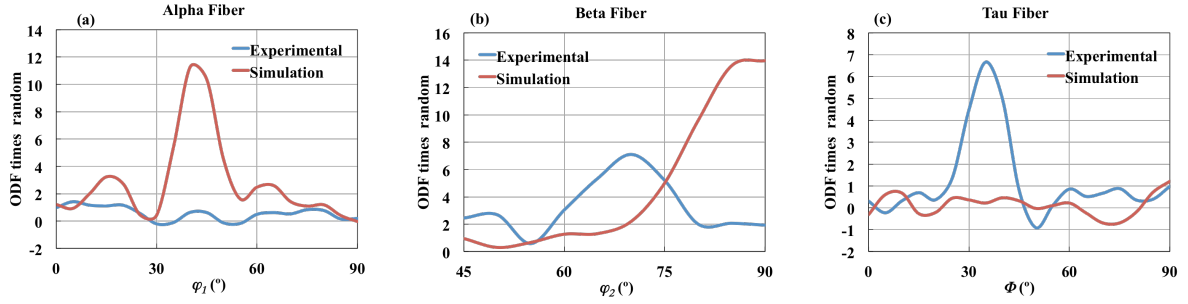


Fig. 4-24 Comparison of (a) α , (b) β and (c) τ fibers for machining and simulations under $D=3\text{ mm}$, $F=0.01\text{ mm/rev}$ and $V=5000\text{ rpm}$

As shown by Fig. 4-25, there are still remarkable differences between the texture attributes of the machined sample and its computer simulation. Nonetheless, the experimental results predict a stronger texture compared lower to depth of cut (Fig. 4-21), as proved by higher intensities of the fibers. However, the simulations still predict a stronger texture with characteristic components α in and β fibers. Similar to the previous case, simulations predict the strongest texture component is along the β fiber and occurs at $\varphi_2 > 80^\circ$.

As shown by Fig. 4-26, increasing the feed rate (from 0.01 mm/rev to 0.8 mm/rev) leads to a remarkable increase in the maximum strain rate calculated by FE simulations. Additionally, higher strain rates are exerted for a longer period of time over the sample. However, the level of strain is similar and even smaller in the higher feed rate. Only after the maximum strain rate time step is elapsed, the strain in the larger feed rate case starts to get higher. A comparison of Fig. 4-22 and 4-26 shows that increasing in the depth of cut causes an increase in the equivalent strain but the rate at which the strain is induced doesn't change noticeably. While, increasing the feed rate affects the strain rate more prominently.

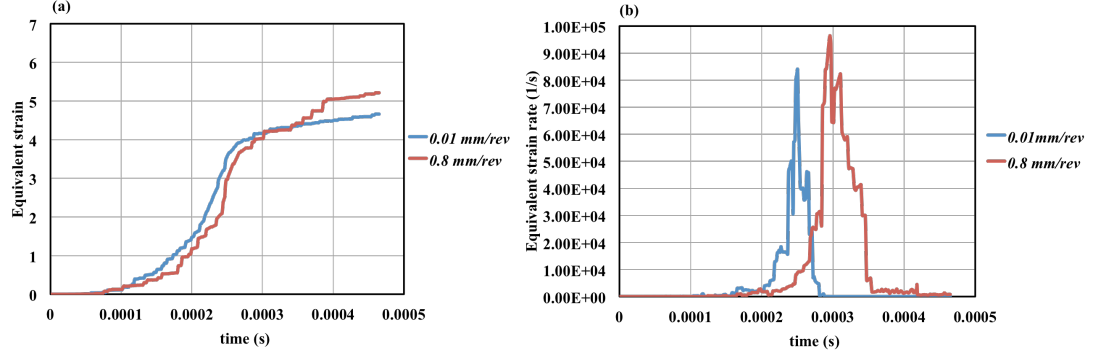


Fig. 4-25. Comparison of (a) equivalent strain and (b) equivalent strain rate for 0.01 *mm/rev* and 0.8 *mm/rev* feed rates. *D* and *V* were respectively 1 *mm* and 5000 *rpm* for both of the cases.

The results of experimental and computational micro-texture studies of the increased feed rate case are shown in Fig. 4-27 and 4-28. The initial material, after being machined at under $D = 1 \text{ mm}$, $F = 0.8 \text{ mm/rev}$ and $V = 5000 \text{ rpm}$ develops a relatively strong texture leading to crystallographic planes between (001) and (101) orient normal to the studied cross-section. This is shown in Fig. 4-27(a). The prediction of the VPSC model for this load condition is quite close to the experimental results, demonstrated by Fig. 4-28.

Fig. 4-28(a) and (b) shows the ODF of the experimentally analyzed material and computationally modeled in machining at an enhanced feed rate. Along the same lines as the IPF, the texture components in both cases seem to be very close. The strongest texture component is the *S* component occurring around $(\varphi_1, \Phi, \varphi_2) \approx (35^\circ, 45^\circ, 0^\circ)$. The close agreement in texture evolution between modeling and experiment can be completely illustrated by comparing the texture fibers shown in Fig. 4-30.

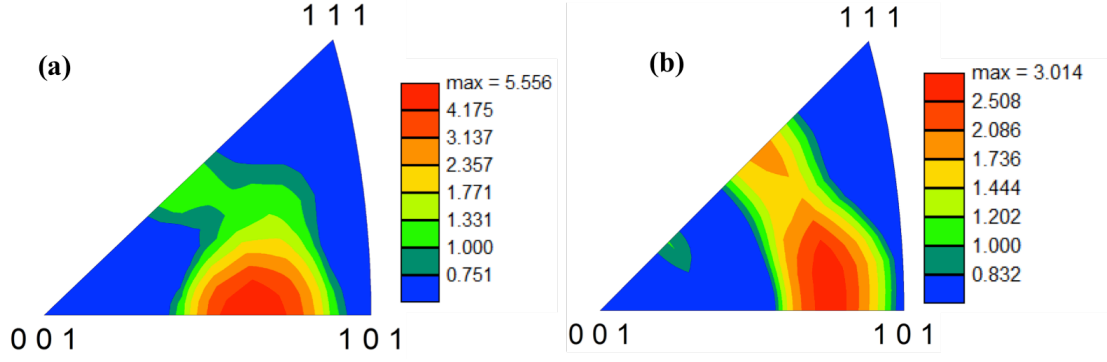


Fig. 4-26 (a) Experimental and (b) computational IPF for machining at $D=1\text{ mm}$, $F=0.08\text{ mm/rev}$ and $V=5000\text{ rpm}$

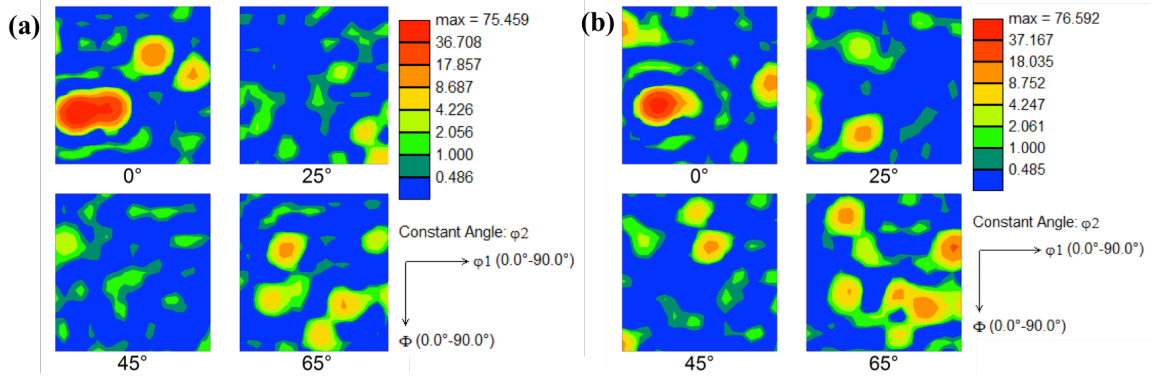


Fig. 4-27. 4-28 (a) Experimental and (b) computational ODF for machining at $D=1\text{ mm}$, $F=0.08\text{ mm/rev}$ and $V=5000\text{ rpm}$

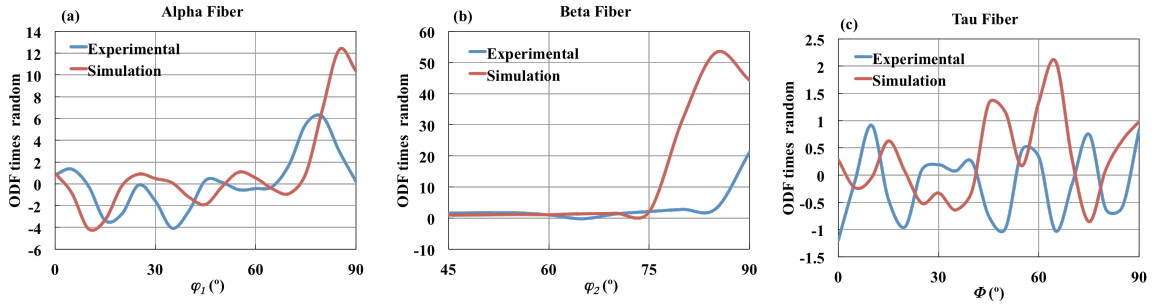


Fig. 4-29. Comparison of (a) α , (b) β and (c) τ fibers for machining and simulations under $D=1\text{ mm}$, $F=0.08\text{ mm/rev}$ and $V=5000\text{ rpm}$

The modeling texture fibers closely follow the experimental ones, both in terms of intensity and shape of the curves. The α fiber shows a maximum intensity about 6 times

random around $\varphi_1 \approx 75^\circ$. Computer simulation predicts a very similar trend, however more momentous in texture. The β fiber is the most intense texture component. The maximal values occur at $\varphi_2 > 80^\circ$. Experiments show that the highest intensity is about 20. Although simulations show exactly the same trend, again over estimate the strength and predict the highest intensity to be about 52. Both simulation and experiments show that the τ fiber possesses the lowest intensity, close to random. Nonetheless, both forecast the same shape for the curve of the τ fiber.

In order to observe the effects of spindle speed V , on the microstructural evolution and micro-texture development, two different samples machined at 200 and 5000 *rpm*. The depth of cut and feed rate were kept as the highest tested values, 3 *mm* and 0.8 *mm/rev* respectively. Fig. 4-31 illustrates the equivalent strain and strain rates in machining at extreme spindle speeds.

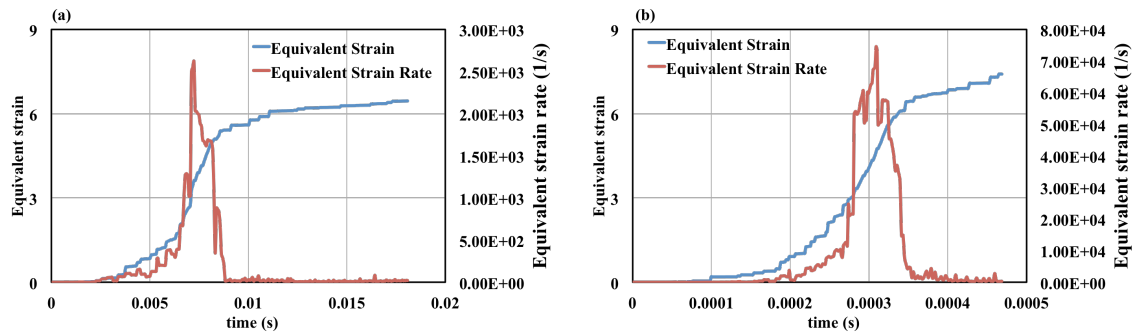


Fig. 4-30 FEA results of equivalent strain and strain rate in (a) 200 and (b) 5000 *rpm* spindle speed. $D=3$ *mm* and $F=0.8$ *mm/rev* for both the cases.

It is worthy of attention that in the low spindle speed, the total duration of removing the material from the simulated arc (Fig. 3-17) will be much longer compared to the high spindle speed, as shown in in Fig. 4-31. Comparing the strains and strain rates for the above cases, one realizes that increasing the spindle speed, leads to a slight increase in the equivalent strain. As shown by the previous results, the strain depends more closely on the depth of cut, so both of these cases show the highest strains (above

6). On the other hand, the strain rate in the high spindle speed case is an order of magnitude larger than the low-spindle speed case. Therefore, one expects to see the effects of increased strain rate much more pronounced in the high spindle speed cases.

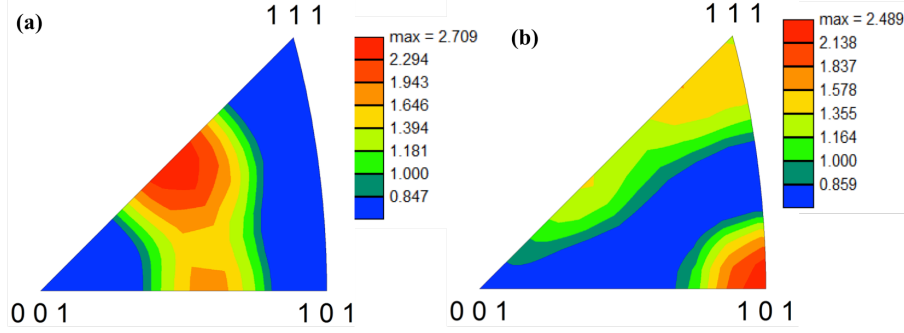


Fig. 4-31 (a) Experimental and (b) computational IPF for machining at $D=3\text{ mm}$, $F=0.08\text{ mm/rev}$ and $V=200\text{ rpm}$

Fig. 4-32 shows the obtained experimental and computational IPFs for machining at low and high spindle speed while the two other parameters are the highest. Although, the strain rate that the material experienced is an order of magnitude lower than other cases, but being in the order of $2.5 \times 10^3\text{ (s}^{-1}\text{)}$, it is still high enough for a degree of texture evolution. Fig. 4-32(a), shows that the machining conditions had a tendency to orient the crystallographic planes in a direction between (001) and (101). According to Fig. 4-32(b), the VPSC model predicts a high population of (101) plane gets normal to the analyzed surface.

Fig. 4-33 compares the experimental and computational ODF for machining under low spindle speed. The experimental results suggest there are several dominant texture component present including the components at $(\varphi_1, \Phi, \varphi_2) \approx (65^\circ, 30^\circ, 45^\circ)$, $(0^\circ, 30^\circ, 45^\circ)$ and other components. The simulation results show a strong Goss texture at $(\varphi_1, \Phi, \varphi_2) \approx (0^\circ, 45^\circ, 0^\circ)$ in addition to the most prominent component of the experimental counterpart at $(\varphi_1, \Phi, \varphi_2) \approx (65^\circ, 30^\circ, 45^\circ)$.

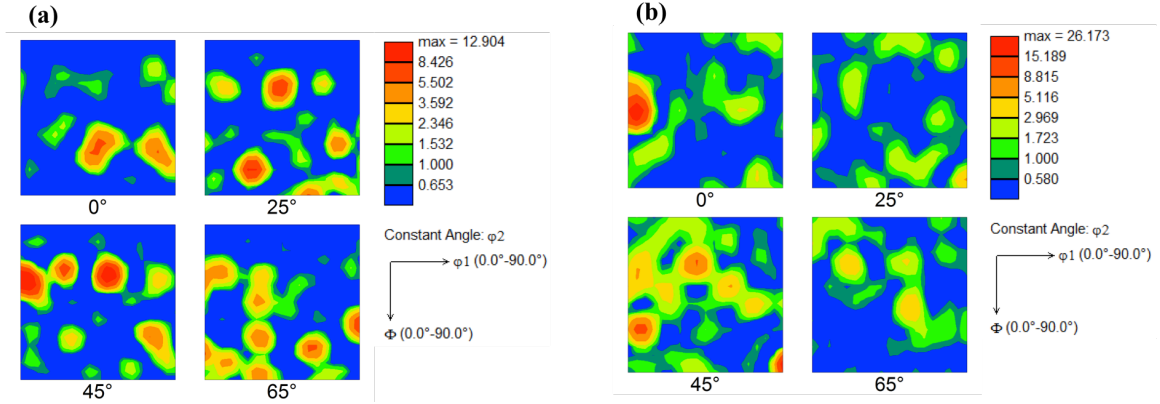


Fig. 4-32. (a) Experimental and (b) computational ODF for machining at $D=3$ mm, $F=0.08$ mm/rev and $V=200$ rpm

Fig. 4-34 demonstrates the α , β and τ texture fibers of the sample machined at the low spindle speed. The β and τ fibers of the simulation and experimental outcomes closely follow each other, while the simulation results show a strong maximum in the α fiber at φ_1 low angles. This corresponds to the strong Goss component observed in the simulation results but the experiments don't show it.

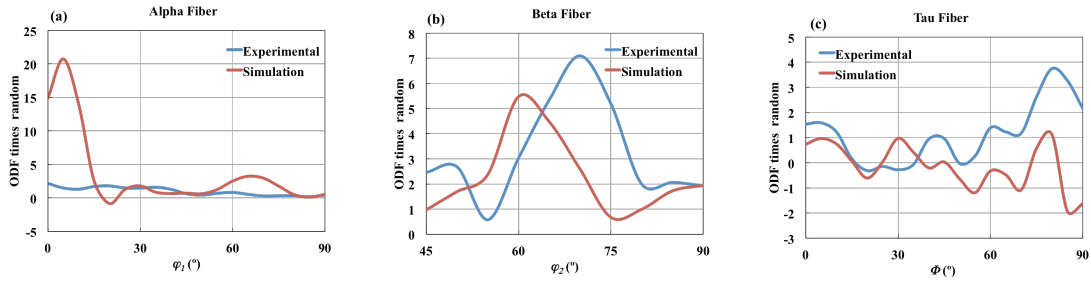


Fig. 4-33. Comparison of (a) α , (b) β and (c) τ fibers for machining and simulations under $D=3$ mm, $F=0.08$ mm/rev and $V=200$ rpm

Fig. 4-35 demonstrates the IPFs of machining with high spindle speed. Similar to all the previous modeling cases, Fig. 4-35(b), predicts an outstanding (101) preferred direction. However, the experimental results show a tendency to a direction between (101) and (102).

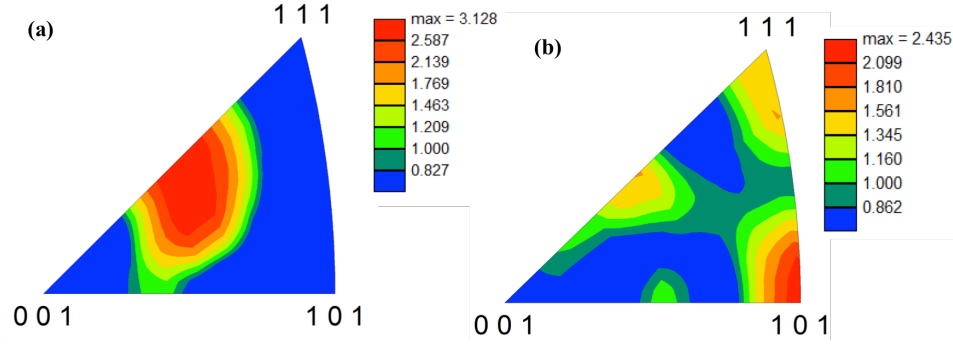


Fig. 4-34. (a) Experimental and (b) computational IPF for machining at $D=3$ mm, $F=0.08$ mm/rev and $V=5000$ rpm

Fig. 4-36 Shows the ODFs for the case of machining at high depth of cut, high feed rate and high spindle speed. The common strong component between the two cases is the $(\varphi_1, \Phi, \varphi_2) \approx (45^\circ, 30^\circ, 45^\circ)$.

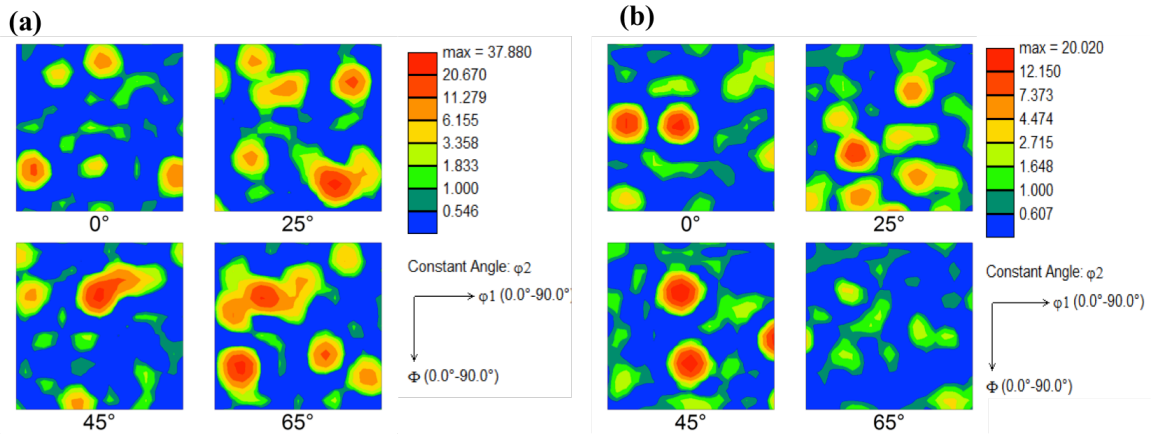


Fig. 4-35 (a) Experimental and (b) computational ODF for machining at $D=3$ mm, $F=0.08$ mm/rev and $V=5000$ rpm

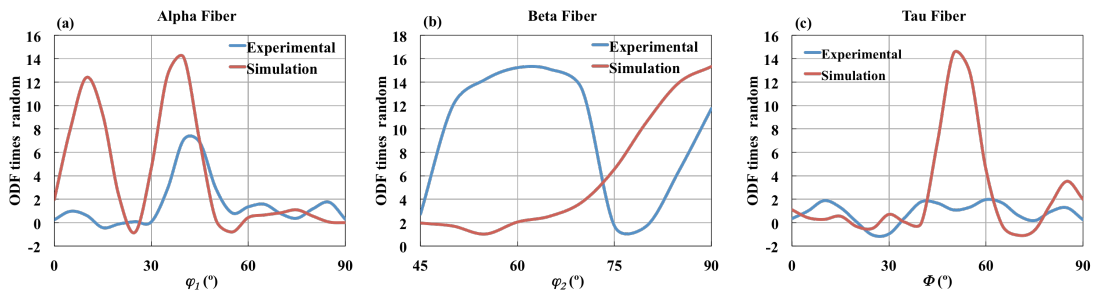


Fig. 4-36. Comparison of (a) α , (b) β and (c) τ fibers for machining and simulations under $D=3$ mm, $F=0.08$ mm/rev and $V=5000$ rpm

In Fig. 4-37, α , β and τ texture fibers are plotted against the Euler angles in the corresponding ranges. The β fiber of both experimental and modeling studies, show a maximum at high φ_2 angles; while a hump at lower angles is seen in the experimental results which is absent in modeling output. One maximal peak of the α fiber is also common between both of the frameworks while a peak in the τ fiber is only predicted by the computer code.

4-5 Conclusions and Future Trends

Texture analysis of the as-received material shows a characteristic close to randomly oriented microstructures. Amongst the orientations confined in the inverse pole figures, the as-received material shows a high intensity of (112) planes. Amongst the texture fibers, the β fiber shows the highest intensity around $\varphi_2 \approx 60^\circ$ with an intensity of ~ 8 times random. The next intense point of texture fibers occurs in the τ fiber at $\Phi \approx 45^\circ$ with an intensity of ~ 4 times random.

According to FE results, depending on the machining conditions. the applied strain and strain rate on the surface of machined AA 7075 are respectively in the range of ~ 4 to ~ 6 and in the order $\sim 10^4$ (s^{-1}). Based on previous modeling findings, these values seem reasonable. According to experiments, machining at the low level of depth of cut and feed rate (i.e. 1 mm and 0.01 mm/rev) and the high level of speed (i.e. 5000 rpm) doesn't change the orientation of the maximal intensity shown by the IPF, however the complete ODF shows a development of a texture component mainly recognized by a hump in the β fiber in the range $80^\circ \leq \varphi_2 \leq 90^\circ$. Simulations also predict this hump.

Increasing the depth of cut to the high level while keep the feed rate at its low value, increases the discrepancy between simulations and experiments. While simulations still predict a pronounced maximum (rather than a hump) in the β fiber and a peak in the α fiber (added compared to the case of low depth of cut) at $\varphi_1 \approx 45^\circ$; the experimental

results show a maximum in the τ fiber at $\Phi \approx 45^\circ$. The reason behind this discrepancy is covered in the next chapter.

Increasing the feed rate to the high level, changes the developed texture. In this case, the prediction of simulation and experimental results are entirely close. The peak of the α and β fibers at respectively φ_1 and $\varphi_2 \approx 90^\circ$ and the rest of humps and valleys of computational predictions closely resemble outcomes of experiments.

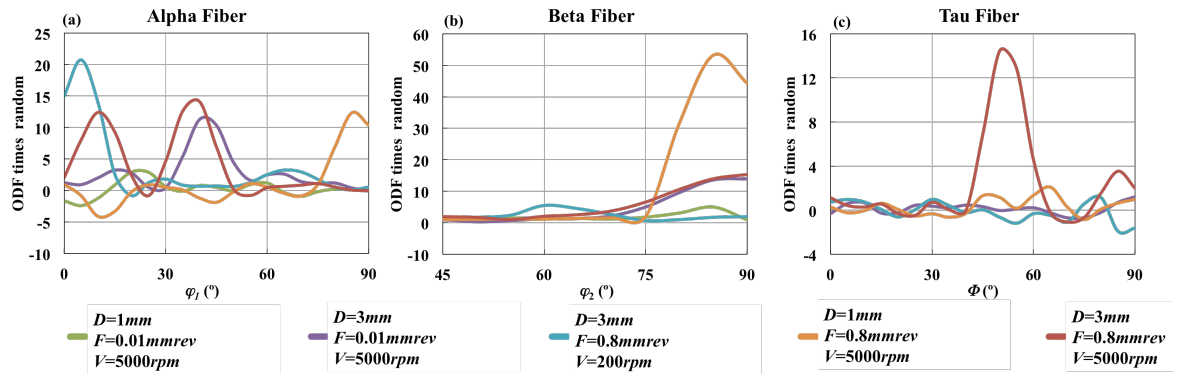


Fig. 4-37 comparison of texture fibers predicted by the computer model

Texture evolutions due to machining at low spindle speed are acceptably followed by simulations except for one peak of the α fiber that the experiment doesn't show. However, increasing the spindle speed from the low level to the high value increases the difference between modeling and experiments results. Fig. 4-37 demonstrates a comparison of all the computational texture fibers. Increasing the feed rate appears to lead to three peaks of the α fiber at 0, 45 and 90° of φ_1 and also to a very sharp peak at $\varphi_2 \approx 90^\circ$ in the β fiber. Simultaneous increase in the depth of cut, seems to cause the growth of the texture component along the τ fiber at $\Phi \approx 45^\circ$.

Based on the obtained results, the future research should be focused on continuation of changing the process parameters (or choosing the values in between the current intervals) to possibly determine all the boundaries of the agreement between

simulation and experimental outcomes. Additional process parameters such as the geometry of cutting can be also taken into account. Furthermore, the starting material can have different distinctive textures in order to consider the effect of the conditions of the starting material on the developed texture evolution framework. Lastly, different material systems with different slip and twinning attributes as well as different crystallographies, can be tested to extend the boundaries of the materials-affected manufacturing concept to other important engineering materials.

5. RECRYSTALLIZATION AND GRAIN GROWTH

5-1 Grain evolution phenomena in machining of AA7075

During inelastic deformation, the majority of the work done on the material goes out to the environment in the form of heat. About 1% of the work is reserved in the microstructure in the form of energy stored [23]. Researchers believe that the majority of the stored energy stems from generation of dislocation. The inelastic deformation caused by slip of dislocations activates dislocation generation sources and causes a several order magnitude increase in the dislocation density of the material[18, 109, 110]. The stored energy is the main thermodynamic drive for the occurrence of recrystallization. It is believed that the recrystallization phenomena at caused by high-strain deformations (specially at elevated temperatures) are fundamentally different from that of low strain. In low and moderate strain regime, the recrystallized microstructures is mainly consists of low-angle grain boundaries. While, deformation to large strains is believed to lead to a refined microstructure mainly composed by high-angle grain boundaries [23]. Recrystallization at the above conditions is so-called “continuous recrystallization”. If high temperatures accompany the large strain, the phenomenon may also be called “geometric dynamic recrystallization”.

Fig. 4-7 shows the grain map of the as-received material. The grain size distribution is demonstrated in Fig. 5-1. The distribution shows a multi-modal regime with 4 distinctive peaks around $\sim 36, 45, 56$ and $71 \mu m$. The theoretical minimum grain size considered in the calculations is $2 \mu m$. Such multi-modal behavior is sensible the distribution plot is compared to the grain map shown in Fig. 4-7. Considering the area fraction of each size bin, the average grain size is $31.6 \mu m$ and the standard deviation is $23.1 \mu m$. The relatively large standard deviation is a result of having a wide spread of

grains sizes; the smallest and the largest grain present in the sample were respectively ~ 13 and $\sim 89 \mu m$ in size.

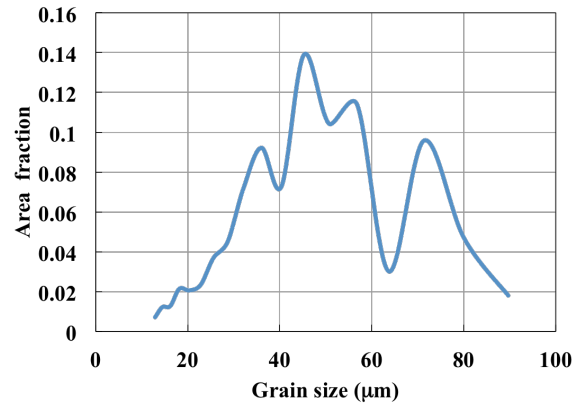


Fig. 5-1 The grain size distribution of the as-received material. The average grain size is $31.6 \mu m$ and the standard deviation is $23.1 \mu m$.

Fig. 5-2 shows the grain map and the image quality map of the sample machined at $D= 1 \text{ mm}$, $F=0.01 \text{ mm/rev}$ and $V=5000 \text{ rpm}$. In the top machined region (i.e. $200 \mu m$ below the surface).

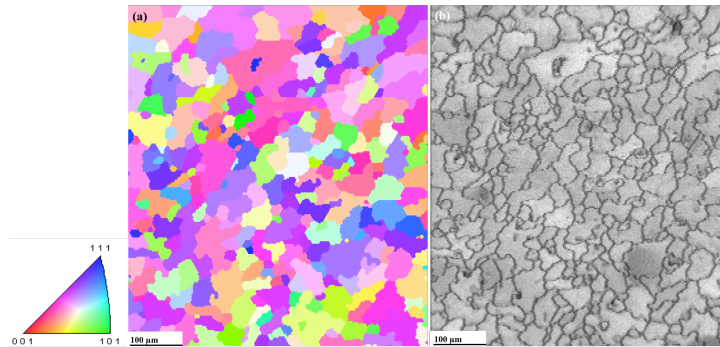


Fig. 5-2. (a) The IPF-overlaid grain map and (b) the image quality map for the sample machined at $D= 1 \text{ mm}$, $F= 0.01 \text{ mm/rev}$ and $V=5000 \text{ rpm}$. The average CI of the image is 0.31.

Fig. 5-2 suggests that a grain growth can be seen at the machined top layer. In fact, the small grains that are present throughout the bulk of the material are mostly absent in the machined top layer. This clue suggests that larger grains have swallowed the small ones. The image quality map shown at Fig. 5-2(b) shows that the quality of the of

detected signals closely follows the pattern of the microstructure; the proof of reliability of the EBSD scan. Fig. 5-3 demonstrates the grain size distribution

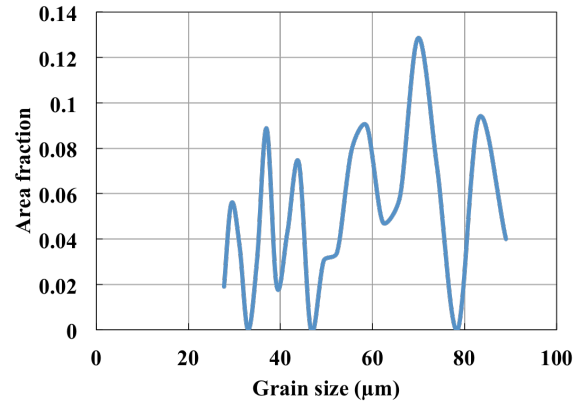


Fig. 5-3. Grain size distribution the sample machined at $D=1\text{ mm}$, $F=0.01\text{ mm/rev}$ and $V=5000\text{ rpm}$. The average grain size is $44\text{ }\mu\text{m}$ and the standard deviation is $25.65\text{ }\mu\text{m}$.

The multi-modal grain size distribution still dominates the microstructure. The existence of several peaks and valleys suggest a sort of “discontinuity” in grain sizes. In fact, growth of larger grains at the expense of disappearance of smaller grains can cause such discontinuity. In other words, one may imagine, wherever a deep valley follows a tall peak valley, grains with size of the valley have vanished and contributed to occurrence of the next peak. Development of a grain growth is obvious from the range of grain sizes under the machined surface. The smallest grains are $\sim 28\text{ }\mu\text{m}$ large while the largest grains still remain close to $\sim 89\text{ }\mu\text{m}$. Therefore, the average grain size, which is $44\text{ }\mu\text{m}$, shifts towards larger grains. However, due to the relative large spectrum of grain sizes, the standard deviation is about the same as the as-received sample and has the of $\sim 25.65\text{ }\mu\text{m}$.

Fig. 5-4 demonstrates the FE results showing the temperature field in depth of the workpiece due to machining. The average maximum temperature of points 4,5 and 6 shown in 4-14, in the duration of the cut are used in plotting Fig. 5-4. According to Fig. 4-5 (a), the peak temperature in machining at the above conditions is $450\text{ }^{\circ}\text{C}$ and the

temperature at $200\ \mu\text{m}$ below the machined surface is $\sim 210\ ^\circ\text{C}$. This depth is close to the region that shows a grain growth in Fig. 5-2. Fig. 5-4(b) illustrates the change in the average of maximum strain and strain rates that points 4,5 and 6 in the simulated machined arc experienced. The important point to note is that, the time step of occurrence of the maximal strains and rate are not the same (compare to Fig. 4-15), also the duration that the material experiences this high strain and rate is very short (thousandths of a second). Nonetheless, the depth of seeing microstructural evolution below the surface is close with what FEM predicts about depth of penetration of field variables. Another important point to note in interpretation of Fig. 5-4 is that, the FE simulations were done on an arc with the insert with nose radius of $0.8\ \text{mm}$, while in experimental machining; a $1.5\ \text{inch}$ long rod was machined. This means that, in experiment the material was exposed to temperatures for a longer time and has experienced a large number of cycles of high and low strains and rates.

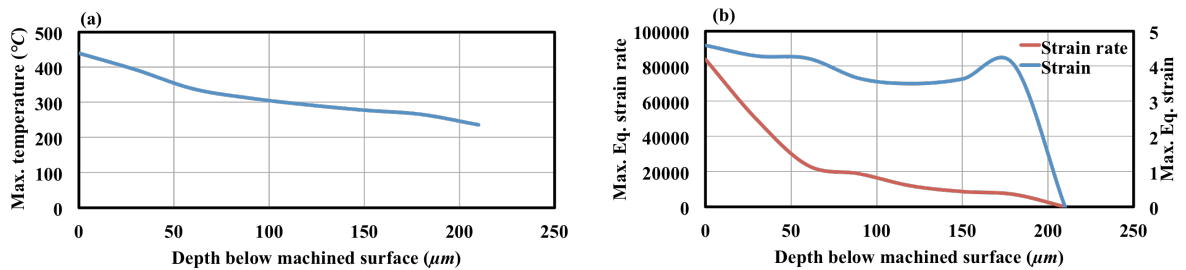


Fig. 5-4 Depth of penetration of (a) temperature and (b) maximal strains and strain rates in the sample machined at $D= 1\ \text{mm}$, $F= 0.01\ \text{mm/rev}$ and $V=5000\ \text{rpm}$.

Chapter 4, showed that FEA results suggest increasing the depth of cut leads to a significant increase in the level of strain induced to the material. In order to observe the effect of increasing the depth of cut, on grain evolution, grain map analyses was performed on the sample machined under $D= 3\ \text{mm}$, $F=0.01\ \text{mm/rev}$ and $V=5000\ \text{rpm}$ conditions. Fig. 5-5 demonstrates the grain maps.

As shown by Fig. 5-5 (a), a severe recrystallization occurs below the machined surface. The IQ map shown in Fig. 5-5 (b) is consistent with Fig. 5-5(a). Since the quality of the EBSD signal drops at the grain boundary, the areas composed of small grains appear darker due to larger area fraction of grain boundaries. Fig. 5-5 shows that even at the machined surface, still, few non-recrystallized large grains exist. Fig. 5-6 illustrates the distribution of the grain sizes under the machined surface.

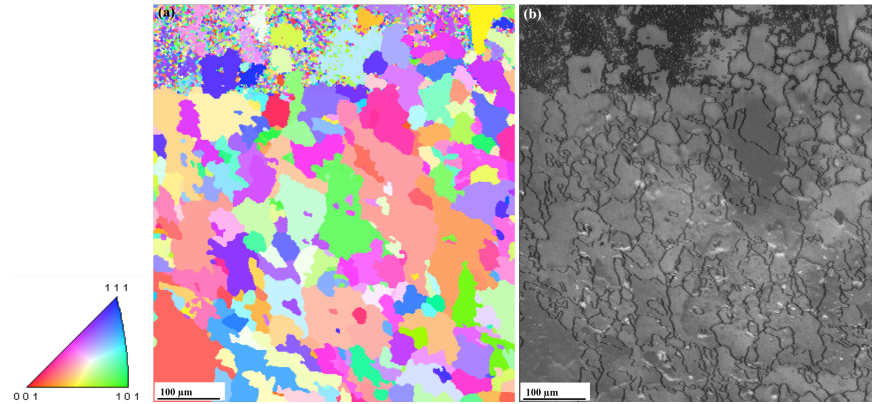


Fig. 5-5(a) The IPF-overlaid grain map and (b) the image quality map for the sample machined at $D=3\text{ mm}$, $F=0.01\text{ mm/rev}$ and $V=5000\text{ rpm}$. The average CI of the image is 0.26

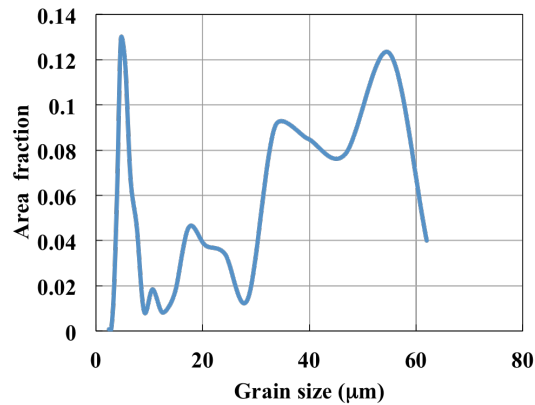


Fig. 5-6. Grain size distribution the sample machined at $D=3\text{ mm}$, $F=0.01\text{ mm/rev}$ and $V=5000\text{ rpm}$. The average grain size is $19.6\text{ }\mu\text{m}$ and the standard deviation is $18.12\text{ }\mu\text{m}$

Fig. 5-6 suggests that distribution type has changed towards a bimodal. There is a sharp peak of small grains at $\sim 7\text{ }\mu\text{m}$ and the second sharpest peak is $\sim 54\text{ }\mu\text{m}$. The average

grain size and standard deviation are respectively 19.6 and 18.12 μm respectively. The range of grain sizes are from ~ 5 to 63 μm . Apparently, compared to the previous case the increased depth of cut which causes a jump in strain and leads to a severe recrystallization. The impact of strain and stored energy on recrystallization is investigated in the next sections.

The Fig. 4-7 shows the grain and IQ map, of the sample machined at $D=1\text{ mm}$, $F=0.8\text{ mm/rev}$ and $V=5000\text{ rpm}$. The grain color code (with the legend shown at the left hand side) shows that the machining-affected layer is mostly shows the same color. This remarkable grain orientation evolution is discussed in chapter 4.

Fig. 4-8 shows the grain size distribution in the first 200 μm below the machined surface. The curve shows a bimodal-type of behavior with two prominent peaks with the same height at 60 and 70 μm . The third peak (with the intensity almost half of the other two occurs at 43 μm . Similar to machining at the same depth of cut and speed (but at lower feed rate), a grain growth seems to occur as shown in Fig. 4-7 by the absence of small grains. In the distribution shown in Fig. 4-8, absence of any peaks at smaller grains and occurrence of deep valleys are also signs of grain growth. Therefore, the average grain size has increased to 42.6 μm and the standard deviation is 18.4 μm . Comparing to the previous cases of lower depth of cut (Figs. 4-6 and 4-3), one can conclude that higher depth of cuts (which lead to higher strains) have a greater potential to lead to a recrystallization while increasing the feed rate will result in a more prominent texture evolution. Additionally, checking the texture evolution results interpreted in chapter 4, one can conclude that in the cases with significant recrystallization, the predicted and measured texture have the largest discrepancy which is obviously due to the fact that the texture evolution code doesn't consider any sort of morphology evolution.

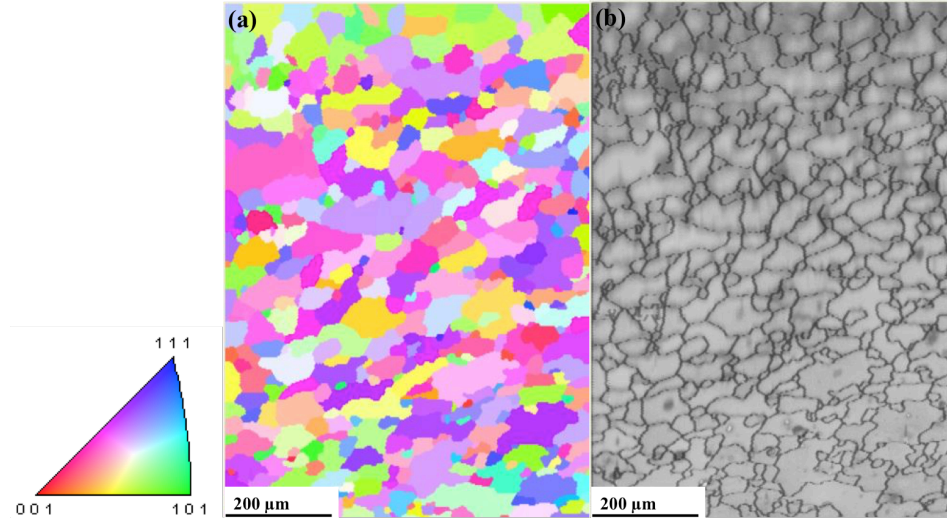


Fig. 5-7(a) The IPF-overlaid grain map and **(b)** the image quality map for the sample machined at $D=1\text{ mm}$, $F=0.8\text{ mm/rev}$ and $V=5000\text{ rpm}$. The average CI is 0.46.

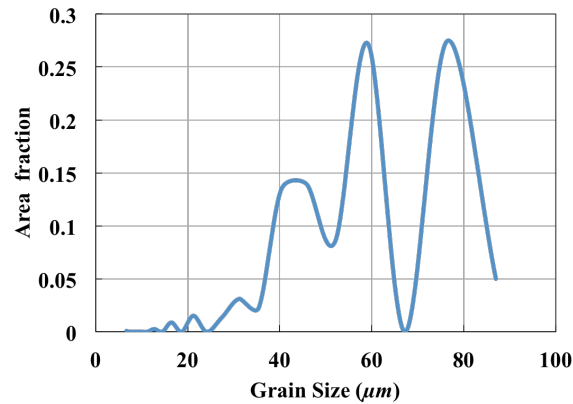


Fig. 5-8 Grain size distribution the sample machined at $D=1\text{ mm}$, $F=0.8\text{ mm/rev}$ and $V=5000\text{ rpm}$. The average grain size is 42.5 μm and the standard deviation is 18.4 μm

In a similar trend compared to texture evolution after investigating the effects of depth of cut and feed rate, the effects of spindle speed on the grain evolution are discussed below. Reducing the spindle speed significantly reduces the temperature that the material experiences. Fig. 5-9 compares the effects of the spindle speed on the maximum temperature and the temperature in the depth of the machined surface.

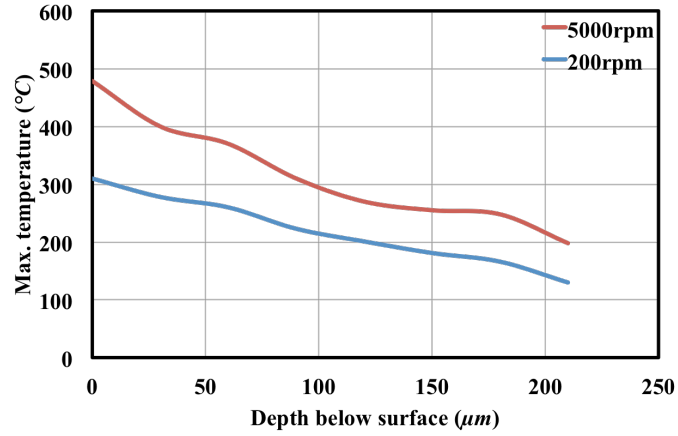


Fig. 5-9 Maximum temperature of the workpiece below machined surface predicted by FEA.

According to FEA, machining at 5000 *rpm* leads to a maximum temperature close to ~450 °C at the surface while it is ~310 °C for machining at 200 *rpm*. The slope of temperature reduction for the case machined at 5000 *rpm* is larger, still the temperature at 200 μm below the depth of the case of 200 *rpm* is lower.

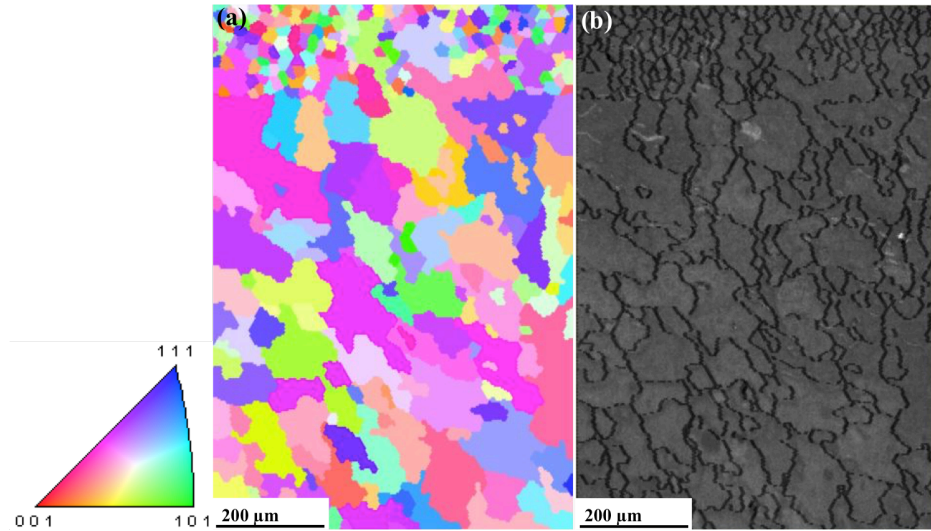
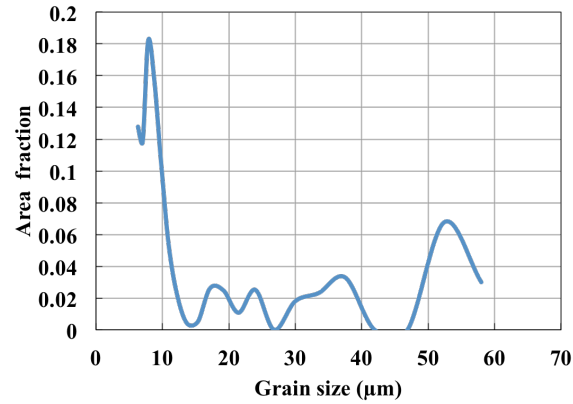


Fig. 5-10 (a) The IPF-overlaid grain map and (b) the image quality map for the sample machined at $D = 3 \text{ mm}$, $F = 0.8 \text{ mm/rev}$ and $V = 200 \text{ rpm}$. The average CI is 0.26.

Fig. 5-10 demonstrates the grain and IQ maps of the sample machined at $D = 3 \text{ mm}$, $F = 0.8 \text{ mm/rev}$ and $V = 200 \text{ rpm}$. A layer of refined grained can be seen below the

machined edge. Compared to the previous recrystallized case (Fig. 5-5), one can see recrystallization at this case was milder. Therefore, fewer new grains have been formed and the subsequent grain growth has led to larger grains.



**Fig. 5-11 Grain size distribution the sample machined at $D=3\text{ mm}$, $F=0.8\text{ mm/rev}$ and $V=200\text{ rpm}$.
The average grain size is $23.8\text{ }\mu\text{m}$ and the standard deviation is $15.8\text{ }\mu\text{m}$**

Fig. 5-11 shows the grain size distribution of the first $200\text{ }\mu\text{m}$ below the machined surface obtained from machining at low spindle speed. Clearly, there is a sharp peak at $\sim 9\text{ }\mu\text{m}$ of size, still due to presence of some larger grains (the second sharp peak is at $52\text{ }\mu\text{m}$) the average grain size and the standard deviation are 23.8 and $15.8\text{ }\mu\text{m}$ respectively.

Fig. 5-12 shows grain and IQ maps when the spindle speed was increased to 5000 rpm (at the high depth of cut and feed rate). Fig. 5-13 exhibits the grain size distribution curve of the machining-affected region. Based on grain map, one concludes that recrystallization has happened in machining. Also, according to discussions of chapter 4, in terms of texture evolution, this sample agrees closely with simulations. The grain size distribution plot, suggest a multi-modal distribution, the high peak at smaller sizes is a sing of dominance of recrystallization. The average grain size and the standard deviation are respectively 24.2 and $22.7\text{ }\mu\text{m}$.

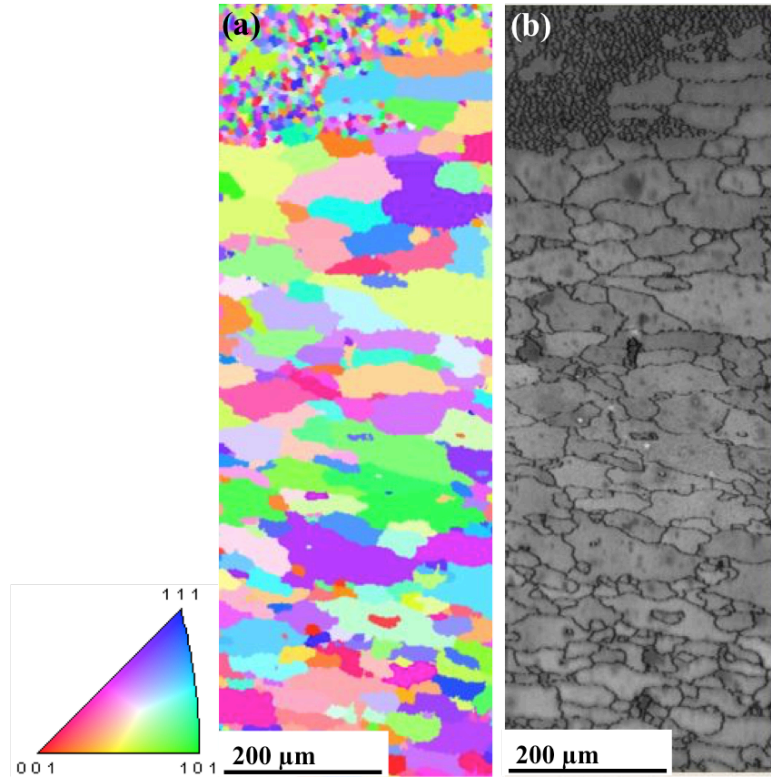


Fig. 5-12 The IPF-overlaid grain map and (b) the image quality map for the sample machined at $D=3\text{ mm}$, $F=0.8\text{ mm/rev}$ and $V=5000\text{ rpm}$. The average CI is 0.25.

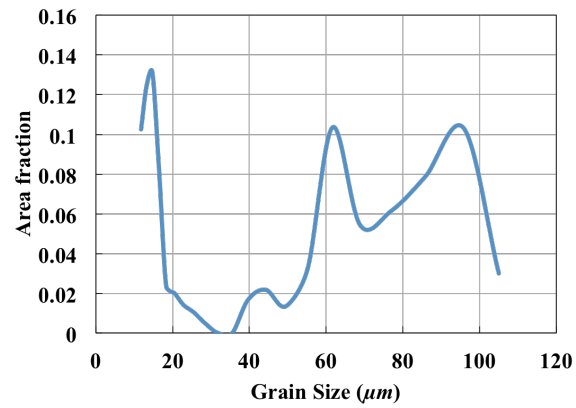


Fig. 5-13 Grain size distribution the sample machined at $D=3\text{ mm}$, $F=0.8\text{ mm/rev}$ and $V=5000\text{ rpm}$. The average grain size is 24.2 μm and the standard deviation is 22.7 μm

5-2 Kinetics of recrystallization and grain growth

Modeling the recrystallization occurring at high temperatures during plastic deformation (AKA dynamic recrystallization) requires a mathematical description of the kinetics of recrystallization. In this regard, Kolmogorov[111], Johnson and Mehl[112] and Avrami[113] carried out the pioneer research. In their works, nucleation and growth of the nuclei were assumed to be thermally activated processes with Arrhenius-type kinetics. Avrami suggested that the recrystallized volume fraction in the material, X_v follows this type of equation:

$$X_v = 1 - \exp(-f\dot{N}^l \dot{G}^m t^n) \quad (5-1)$$

where \dot{N} and \dot{G} are respectively thermally activated rates of nucleation and growth with Arrhenius-type dependence to temperature. f is a shape factor ($4\pi/3$ for spheres) and l , m and n are (possibly crystallography and process-dependent) material parameters. In randomly homogeneous nucleation, these constants are equal to 1, 3 and 4 respectively[23]

Later observations proved that recrystallization doesn't occur unless the material has experienced a minimum level of strain. The role of strain and strain rate is even more outstanding during dynamic recrystallization. Therefore, efforts were directed in modifying the Avrami-type equations with regard to the effects of strain [114-117].

In many works after introduction of the Zener-Hollomon (ZH) parameter [118], the effect of time in mathematical description of dynamic recrystallization is incorporated in the form of strain rate and the ZH parameter ($Z = \dot{\epsilon} \exp(Q/RT)$). According to reports [29], the ZH activation energy, Q , for AA 7075 is 116.7 kJ/mol. In many works, Z or Z^r (r is a material dependent exponent) has been used as the criterion for the onset of (dynamic) recrystallization [23]; specifically because this parameter also incorporates the temperature and activation energy dependence of the process. Some researchers have

tried to use a mixture of Z and factors such as the initial grain size as the criterion of the start of the recrystallization[119].

One of the most widely accepted Avrami-based kinetic equations that is believed to accommodate recrystallization in many metallic systems [22, 120-122], including AA 7075 [29, 39, 40], has the following form:

$$X_V = 1 - \exp\left[-\beta\left(\frac{\epsilon - a\epsilon^*}{\epsilon^*}\right)^k\right] \quad (5-2)$$

where β , a and k are materials constants. ϵ^* is the critical strain parameter of the onset of recrystallization. The functional form of this critical strain with respect to the grain size and the Z parameter is as follows [29, 39, 40, 119]:

$$\epsilon^* = Ad^h Z^m \quad (5-3)$$

where A , h and m are materials constants and d represent the average grain size. The average grain size after dynamic recrystallization, d_{DRX} can be obtained by [29, 39, 40, 119]:

$$d_{DRX} = A_0 \epsilon^n Z^{m^*} \quad (5-4)$$

Again, A_0 , n and m^* are materials constants. The kinetics of grain growth is also believed to be as follows [29, 39, 40]:

$$d_G = \left[d_0^M + Bt \exp\left(-\frac{Q_G}{RT}\right) \right]^{1/M} \quad (5-5)$$

where M and B are materials constants. Q_G is the activation energy for grain growth and was chosen from literature [39], to be 392.9 kJ/mol. d_0 is initial grain size, which in our case can be replaced by d_{DRX} is dynamic recrystallization happens. All the materials constants for AA7075 can be found in [29, 39, 40, 123, 124].

The DEFORM™ 3D package allows the user to introduce equations and calculate desired parameters (at the nodes) in conjunction with field variables (such as strain, strain

rate, temperature, stress and etc.) that the package calculates by default. In order to determine the grain evolution, Eq. (5-2) to (5-5) were coupled with the FE analysis at each time step during the process. In addition to materials constants that were manually introduced, the software was asked to use the values of temperature, equivalent strain and equivalent strain rate at each time interval at each node. The initial grain size of $31.6\ \mu\text{m}$ (obtained from Fig. 400) is used as the starting point of grain evolution modeling. In this approach, the simplifying assumption is that all the grains of the material have the average grain size.

5-3 Modeling recrystallization and growth in machining of AA7075

As explained in previous sections and chapters, kinetic-based modeling of grain evolution was performed in a step-wise manner using the FE code. Fig. 5-14 demonstrates the evolution of the average grain size of the sample machined at $D = 1\ \text{mm}$, $F = 0.01\ \text{mm/rev}$ and $V = 5000\ \text{rpm}$. As Fig. 5-14 shows there is an increase in the average grain size in machining of AA 7075. The average grain size of the machined surface is $\sim 39\ \mu\text{m}$. Obviously, a grain growth is predicted, though the experimental results predict an average grain size of $\sim 44\ \mu\text{m}$, the trend of predication of the grain size is correct and the 11% discrepancy doesn't cast uncertainty on the applied methodology.

According to experimental works, increasing the depth of cut would result in a clear recrystallization and grain refinement. Fig. 5-15 exhibits the FE results for machining at high depth of cut (i.e. $3\ \text{mm}$) with an obvious reduction of the average grain size from 31.6 to $23\ \mu\text{m}$. However, in this case, the FE simulation overestimates the average grain size where the experimental results show $\sim 19.5\ \mu\text{m}$. Nonetheless, the direction of prediction of phenomenon occurring (grain growth or recrystallization and refinement) is correct.

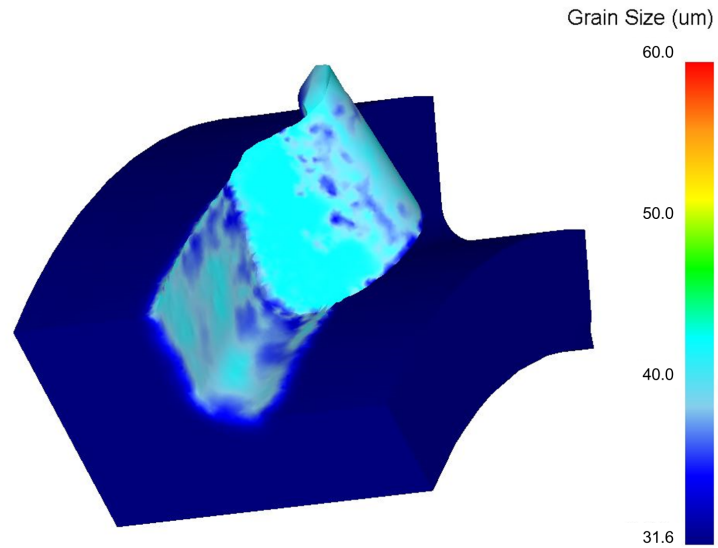


Fig. 5-14. Predicted change in the average grain size in machining at $D= 1\text{ mm}$, $F = 0.01\text{ mm/rev}$ and $V=5000\text{ rpm}$. The average grain size is $39\text{ }\mu\text{m}$.

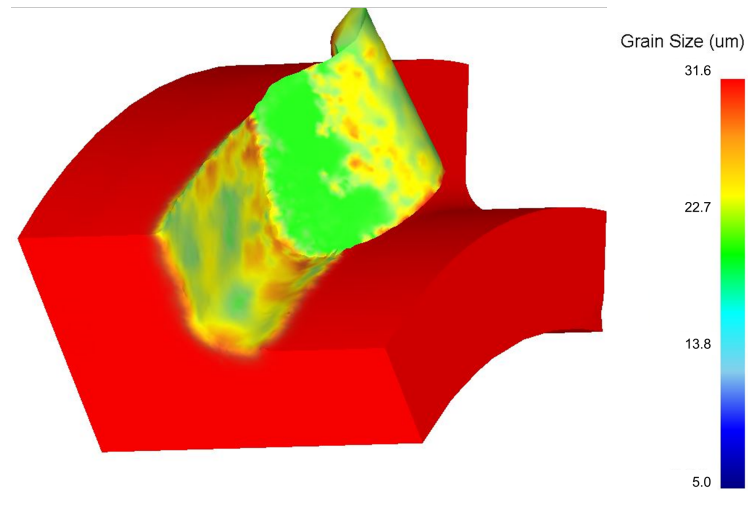


Fig. 5-15 Predicted change in the average grain size in machining at $D= 3\text{ mm}$, $F = 0.01\text{ mm/rev}$ and $V=5000\text{ rpm}$. The average grain size is $23\text{ }\mu\text{m}$.

The effects of increased feed rate are shown in Fig. 5-16 where the simulation predicts machining at 0.8 mm/rev . In this case both experiments and simulation predict a

grain growth with the average grain size being $\sim 38 \mu m$. In this case, the experiments show a $\sim 42 \mu m$ for the average grain size.

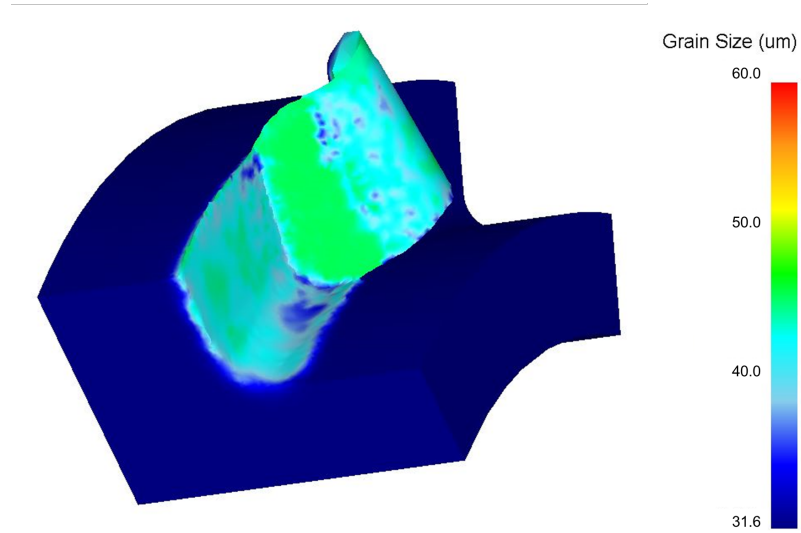


Fig. 5-16 Predicted change in the average grain size in machining at $D=1 \text{ mm}$, $F=0.8 \text{ mm/rev}$ and $V=5000 \text{ rpm}$. The average grain size is $38 \mu m$.

The impact of spindle speed on occurrence of recrystallization or growth is shown in Fig. 5-17 and 5-18. The low spindle speed (i.e. 200 rpm) results shown in Fig. 5-17, suggest a refinement to $\sim 27 \mu m$. The corresponding experiments, provide an average value to be about $\sim 23 \mu m$. The increased spindle speed of 5000 rpm (at high depth of cut and high feed rate), leads to as slight refinement to $\sim 28 \mu m$ along the same lines as the machining works leading to a recrystallized state with the average grain size of $\sim 24 \mu m$.

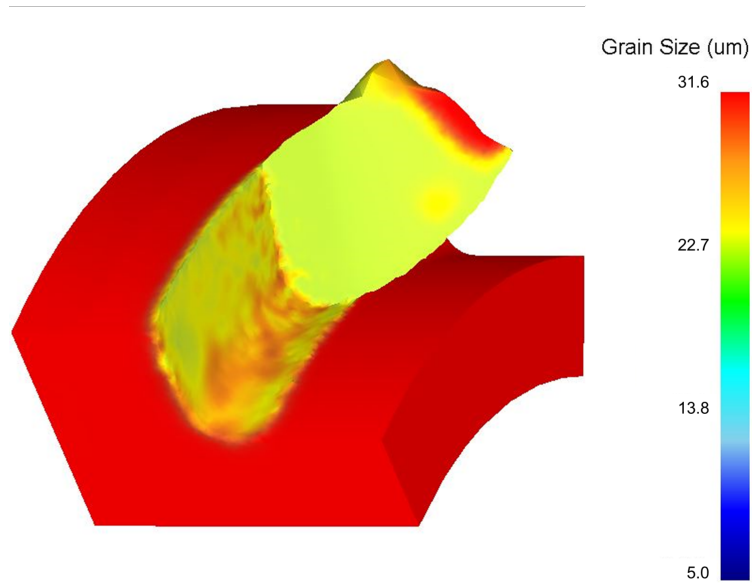


Fig. 5-17 Predicted change in the average grain size in machining at $D=3\text{ mm}$, $F=0.8\text{ mm/rev}$ and $V=200\text{ rpm}$. The average grain size is $27\text{ }\mu\text{m}$.

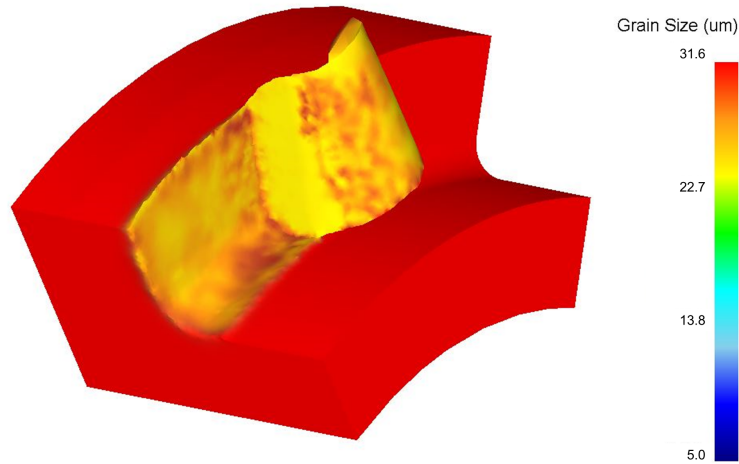


Fig. 5-18 Predicted change in the average grain size in machining at $D=3\text{ mm}$, $F=0.8\text{ mm/rev}$ and $V=5000\text{ rpm}$. The average grain size is $40\text{ }\mu\text{m}$.

5-4 Conclusions and future trends

Experimental observations suggest that remarkable microstructural evolutions occur below the machined surface. FE results indicate that the depth of penetration of strain and strain rate fields is about $\sim 200\text{ }\mu\text{m}$ which is in agreement with the observations. Additionally, for all the cases, the surface temperature is beyond the recrystallization

temperature, which suggests that depending on the level of strains or strains, recrystallization and/or grain growth can occur. As a matter of fact, due to inevitable differences between real machining and FE simulations of an arc, the material might experience different field variables. However the trend of grain evolutions predicted by kinetic-based modeling of recrystallization and grain growth is the same as experimental findings.

As mentioned above, due to the high temperature, dynamic recrystallization can occur in all the samples. However, the samples machined at the lower depth of cut tend to develop a grain growth. Machining at the high feed rate (and still at the low depth of cut and high) leads to a distinctive texture attribute, which is also indicated by the VPSC model.

On the other hand, increasing the depth of cut which according to FEA data, is accompanied by increased strains, promotes a severe recrystallization. Reduced spindle speed alleviates recrystallization resulting in larger grains compared to the intensely recrystallized cases.

The recrystallized grains possess a different texture characteristic compared to grains prior to recrystallization. However, the VPSC model, which was used for capturing texture evolutions, is not capable of incorporating recrystallization. Therefore, the texture that the model predicts for recrystallized cases show a discrepancy compared to experimental results.

The future direction of research should be towards incorporation of recrystallization into crystal plasticity formalisms to fine-tune the computational core used in materials-affected manufacturing. Additionally, application of a different starting microstructure is helpful in testing the soundness and generality of the obtained trends in grain evolutions. Finally, checking the findings with other important engineering material systems is critical in proving the comprehensiveness of the computational toolset of material-affected manufacturing.

6. PROCESS PATH FUNCTIONS

6-1 Generalized spherical harmonic expansion of ODF

As described in chapter 4, it can be proven that the basis vectors of Euler angles form an orthogonal coordinate system in the Euler space[79]. The corresponding basis functions are named generalized spherical harmonics (GSH). GSH functions, T_l^{mn} are product of two complex spherical harmonics with a generalization of associated Legendre's polynomial of degree l with the polar angle argument $\cos(\Phi)$ [79]:

$$T_l^{mn} = e^{im\varphi_1} e^{in\varphi_2} P_l^{mn}(\cos\Phi) \quad (6-1)$$

The generalized associated Legendre polynomials, P_l^{mn} is defined as follows:

$$P_l^{mn}(x) = \frac{(-1)^{l-m} i^{n-m} \sqrt{\frac{(l-m)!(l+n)!}{(l+m)!(l-n)!}}}{2^l (l-m)! \sqrt{(1-x)^{n-m} (1+x)^{n+m}}} \frac{d^{l-n}}{dx^{l-n}} \left[(1-x)^{l-m} (1+x)^{l+m} \right] \quad (6-2)$$

m , n and l are integer indices where $0 \leq l$, $-l \leq m \leq l$ and $-l \leq n \leq l$. It can be shown that a summation of GSH terms (multiplied in complex coefficients to obtain real values), represent probability density functions. Therefore, the orientation distribution function (ODF) f , can also be expanded in GSH terms [79]:

$$f(\varphi_1, \Phi, \varphi_2) = \sum_{l=0}^{\infty} \sum_{m=-l}^l \sum_{n=-l}^l c_l^{mn} T_l^{mn} \quad (6-3)$$

The complex coefficient c_l^{mn} are so-called the microstructure descriptors and are treated as benchmarks to evaluate the specific orientation distribution of a polycrystalline aggregate and compare to other cases [13, 106, 107], since the GSH term T_l^{mn} only consist of angular terms. In other words, these c_l^{mn} coefficients are the terms that make the ODFs of two different materials (e.g. an extruded BCC Iron and rolled FCC copper) different; the T_l^{mn} term is the same in both (and all other) cases. Since the GSH functions are

orthogonal, obtaining c_l^{mn} terms is mathematically straightforward, although can be computationally time-consuming:

$$c_l^{mn} = \frac{2l+1}{8\pi^2} \int_0^{2\pi} \int_0^\pi \int_0^\pi f(\varphi_1, \Phi, \varphi_2) \hat{T}_l^{mn} \sin \Phi d\varphi_1 d\Phi d\varphi_2 \quad (6-4)$$

where \hat{T}_l^{mn} is the complex conjugate of the GHS terms. The $\frac{2l+1}{8\pi^2}$ before the integral comes from the definition of Legendre polynomials in conjugate form and verifies normality. In this work, the ODF used in Eq. (6-4) integrations, is obtained by discrete 5° binning (i.e. $\Delta[\text{Euler angle}] = 5^\circ$) based on the definition of ODF provided in Eq. (4-1). In discrete ODF determination, normality has to be manually imposed to obtain the values of ODF:

$$1 = \frac{1}{8\pi^2} \sum_{\varphi_1} \sum_{\Phi} \sum_{\varphi_2} f(\varphi_1, \Phi, \varphi_2) \Delta\varphi_1 \Delta\varphi_2 \left[\cos\left(\Phi_i - \frac{\Delta\Phi}{2}\right) - \cos\left(\Phi_i + \Phi_i - \frac{\Delta\Phi}{2}\right) \right] \quad (6-5)$$

6-2 ODF coefficients evolution in machining of AA7075

With regard to Eq. (6-4) and (6-5), the c_l^{mn} coefficients of the textures of machined samples as well as the corresponding VPSC model simulations are derived. The calculations were done up to $l_{\max} = 22$ which is the highest limit reported in performing such computations [13, 106, 107, 125-127]. Therefore, the total number of c_l^{mn} coefficients is 42592. Crystallographic symmetries are also important in the above calculations. The crystal symmetry of Al-based materials is cubic. The sample symmetry in machining of rods was assumed triclinic (i.e. no symmetry). Due to crystallographic symmetries and mathematical constraints [79], a great majority of these coefficients are either zero or redundant terms. Assigning cubic crystal symmetry, triclinic sample symmetry and $l_{\max} = 22$ results in 288 non-zero non-redundant c_l^{mn} coefficients. The first three coefficients, namely c_4^{11} , c_4^{12} and c_4^{14} are chosen for the purpose of plotting. It is

important to note that these three coefficients didn't necessarily have the highest numerical values for the all studied cases; but only chosen for the purpose of comparison of different samples and simulation results.

Fig. 6-1 shows positions of the above coefficients in the c_4^{11} - c_4^{12} - c_4^{14} space for the case investigating the depth of cut. The feed rate and spindle speed were respectively 0.01 mm/rev and 5000 rpm. According to this figure, machining introduces a remarkable change in the initial material. However, the simulations predict slightly different points in the space. Nonetheless, increased depth of cut seems to be in a direction that converges the simulations and the experiments. Additionally, the change due to increasing the depth of cut seems to be similar in both the cases.

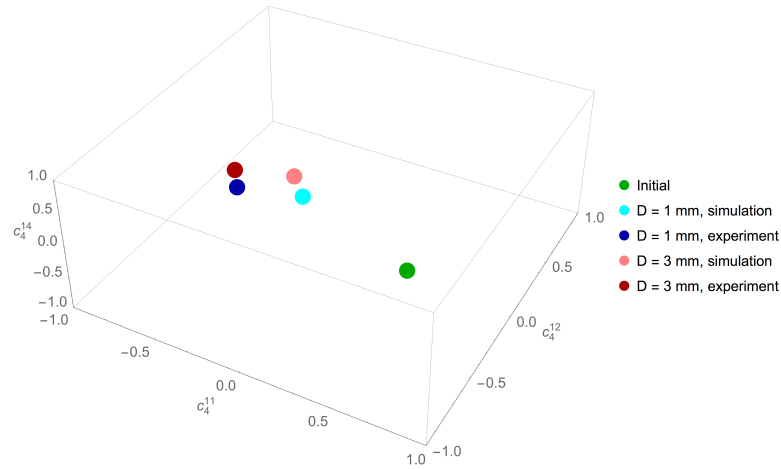


Fig. 6-1 Changes in GSH coefficients of the experimental and computational ODF with imposed by increasing the depth of cut

Fig. 6-2 demonstrates the effects of feed rate on the evolution of microstructural descriptors. Unlike the case of depth of cut; increasing the feed rate generates a remarkable change in the coefficients. The simulation coefficients closely follow the experimental terms, specifically, for the case of high feed rate. This is also in accord with the EBSD grain maps and ODF plots covered in previous chapters. Looking at Fig. 6-2, one can realize there is a path connecting the points in the space. Determining the mathematical attributes of the path is discussed in the next section.

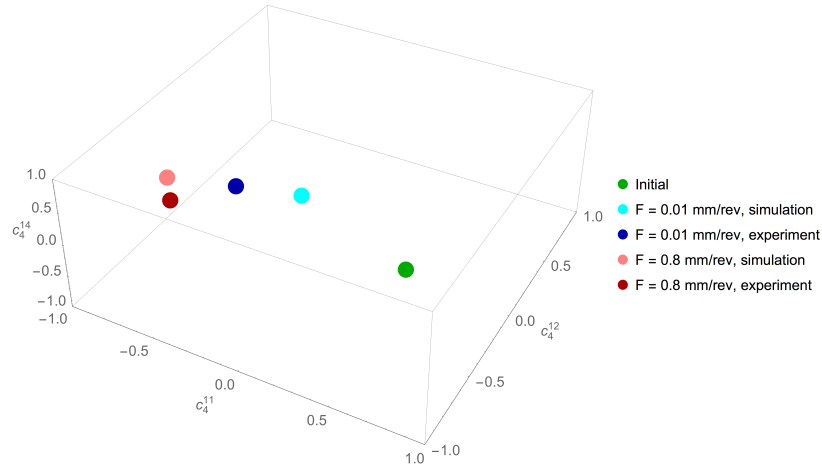


Fig. 6-2 Changes in GSH coefficients of the experimental and computational ODF with respect to the change in feed rate

Finally, the effects of changing the spindle speed on the first three texture coefficients are depicted in Fig. 6-3, which suggests a more pronounced change compared to the effect of depth of cut and feed rate. In this case, the simulation results of the increased spindle speed overestimate the experimental outcomes. Compared to experiment, simulations predict a bigger change in the microstructure descriptors due to increased spindle speed. Similar to the case of depth of cut, the change in the coefficients can be imagined to occur along a certain path. It seems that experimental and computational points converge if both continue the along the current path.

6-3 Determination of process path functions

The previous sections explain the expansion of the ODF into two groups of terms, the GHS terms and microstructure coefficients. As mentioned earlier, the GSH terms only contain angular contribution to the ODF. Therefore, the effect of the change in processing parameter emerges in the c_l^{mn} coefficients. In the other words, these coefficients are functions of process parameter η , i.e. $c_l^{mn}(\eta)$. Here, η can be either depth of cut, feed

rate or spindle speed. Therefore, in order to computationally follow the evolution of microstructure, the GSH expansion of the ODF is written as [128-130]:

$$f(\varphi_1, \Phi, \varphi_2, \eta) = \sum_{l=0}^{\infty} \sum_{m=-l}^l \sum_{n=-l}^l c_l^{mn}(\eta) T_l^{mn}(\varphi_1, \Phi, \varphi_2) \quad (6-6)$$

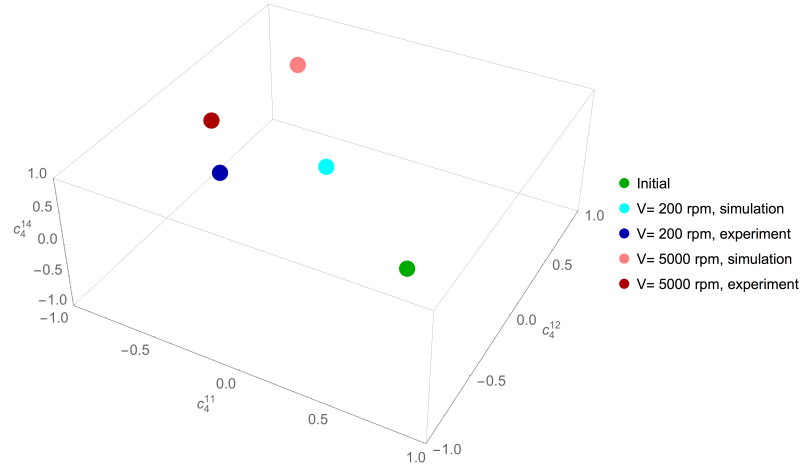


Fig. 6-3 Changes in GSH coefficients of the experimental and computational ODF with increasing the spindle speed

In order to obtain functionality of the c_l^{mn} with respect to η , Garmestani et al. [128, 129] applied the orientation conservation principle [130] which states orientations are neither created nor destroyed. Therefore, the divergence theorem can be applied:

$$\oint_{\sigma} f(\varphi_1, \Phi, \varphi_2, \eta) \cdot \hat{n} ds + \frac{\partial}{\partial \eta} \int_v f(\varphi_1, \Phi, \varphi_2, \eta) dv = 0 \quad (6-7)$$

where dv and σ are respectively the volume and surface area of the ODF element. If $R(\varphi_1, \Phi, \varphi_2)$ is considered as a flow rate function (the discussion is analogous to fluid flow [131]), then Eq. (6-6) can be written as:

$$\frac{\partial f(\varphi_1, \Phi, \varphi_2, \eta)}{\partial \eta} + \text{div}[f(\varphi_1, \Phi, \varphi_2, \eta) R(\varphi_1, \Phi, \varphi_2)] = 0 \quad (6-8)$$

The first term in Eq. (6-8), corresponds to the quantity of orientations and the second term represents the flow of orientations in and out of the infinitesimal volume in the orientation space. Substituting Eq. (6-8) into (6-6) and some mathematical manipulations lead to[129]:

$$\frac{dc_l^{mn}}{d\boldsymbol{\eta}} = \sum_{\lambda\rho\sigma} A_{l\lambda}^{mn\rho\sigma} c_{\lambda}^{\rho\sigma}(\boldsymbol{\eta}) \quad (6-9)$$

where

$$\text{div}\left[T_l^{mn}(\boldsymbol{\varphi}_1, \Phi, \boldsymbol{\varphi}_2) R(\boldsymbol{\varphi}_1, \Phi, \boldsymbol{\varphi}_2)\right] = - \sum_{\lambda\rho\sigma} A_{l\lambda}^{mn\rho\sigma} T_l^{mn}(\boldsymbol{\varphi}_1, \Phi, \boldsymbol{\varphi}_2) \quad (6-10)$$

Integrating Eq. (6-9) leads to the solution of the differential equation [129]:

$$c_l^{mn}(\boldsymbol{\eta}) = c_l^{mn}(\boldsymbol{\eta}_0) e^{A(\boldsymbol{\eta}-\boldsymbol{\eta}_0)} \quad (6-11)$$

Now, in order to obtain the process path functions, four other FE simulations for D , F and V were performed. The FE results were used as inputs of the VPSC code and the texture coefficients were calculated. Therefore, for each parameter a total of 6 computational points (two of which compared to experiments) are used to determine the process path function. For the case of feed rate as the parameter, the depth of cut and the spindle speed were kept constant at respectively 3 mm and 5000 rpm . In addition to 0.01 and 0.8 mm/rev feed rates (which were experimentally verified), 1, 1.2, 1.4 and 1.6 were completely computationally studied. It is important to note that based on the experimental observation, the effects of feed rate were closely followed by the combination and FEA and VPSC model. Fig. 6-4 demonstrates the points in the coefficient space obtained for extended computational analysis for changing the feed rate as the main variable.

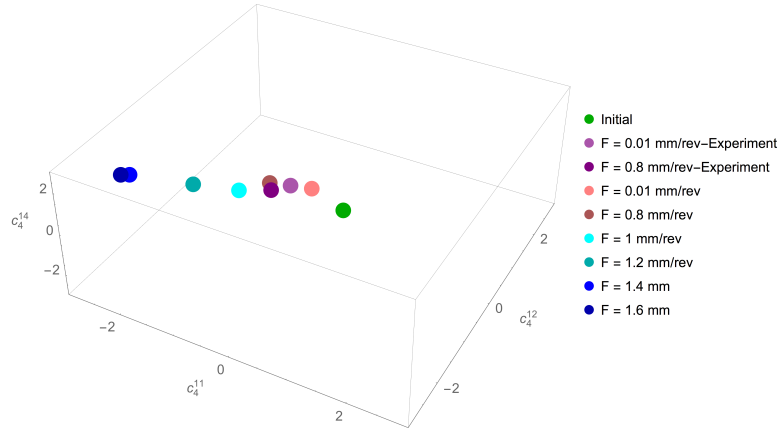


Fig. 6-4 The evolution of AA7075 machined under different feed rates at $D = 1 \text{ mm}$ and $V = 5000 \text{ rpm}$

According to Fig. 6-4, the evolution of the microstructure along a path in the descriptors space is clear. The region bounded by the points (shown in form of a hyper-surface in Fig. 6-5) determines a portion of the microstructure hull, which is achievable by changing the feed rate (keeping other parameters at the constant values).

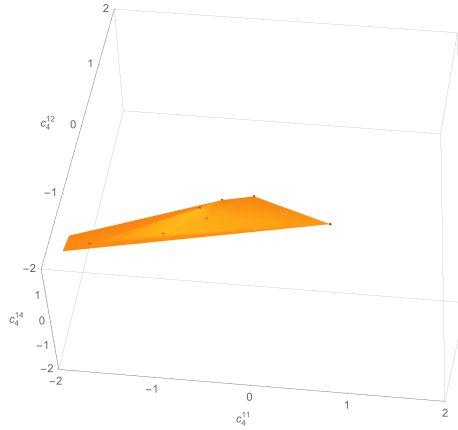


Fig. 6-5 The hyper-surface containing all the possible microstructure achievable by changing the feed rate. Red points show the computationally determined points.

In order to obtain the process path functions, the first approach is to fit the trend of texture coefficients with known functions as Fig. 6-6 demonstrates. Polynomials of different order (for different coefficients) are used by a computer software (Wolfram Mathematica® 10, student version), to exactly pass through the computationally determined solid points.

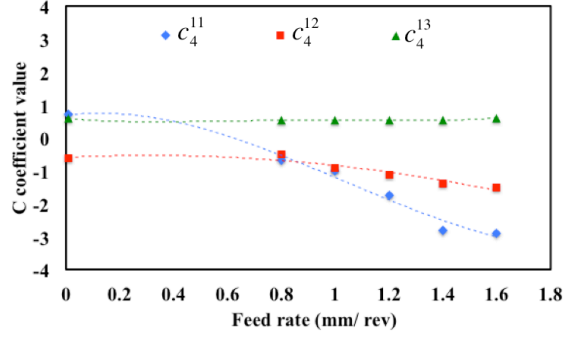


Fig. 6-6 Polynomial fitting of changes in computationally determined microstructure coefficients obtained by varying the feed rate

However such interpolations are possibly not accurate means of determining microstructural modifications; perhaps unless the change in process parameter is very small. Since the interpolation only considers the one coefficient at a time but as implied by Eq. (6-9), the changes in one c_i^{mn} are not independent from other coefficient. Therefore, matrix expansion of Eq. (6-9) leads to determination of the c_i^{mn} coefficients for any change in parameters, if the corresponding A matrices are calculated.

In order to make sure the accuracy of the A matrix is acceptable for a process, at least six non-trivial c_i^{mn} have to be used [129]. These coefficients chosen for this work, are c_4^{11} , c_4^{12} , c_4^{14} , c_6^{11} , c_6^{12} and c_6^{14} . For studying the feed rate F , Eq. (6-12) represents an expansion of Eq. (6-9) for the case of one example coefficient, say c_4^{11} :

$$\frac{dc_4^{11}}{dF} = A_{44}^{1111} c_4^{11} + A_{44}^{1112} c_4^{12} + A_{44}^{1114} c_4^{14} + A_{46}^{1111} c_6^{11} + A_{46}^{1112} c_6^{12} + A_{46}^{1114} c_6^{14} \quad (6-12)$$

Eq. (6-13) shows the matrix representation of the c_i^{mn} coefficients for six different steps of feed rate increase. The first component of each column shows the feed rate.

$$\begin{bmatrix} \text{feed rate} \\ c_4^{11} \\ c_4^{12} \\ c_4^{14} \\ c_6^{11} \\ c_6^{12} \\ c_6^{14} \end{bmatrix} = \begin{bmatrix} 0.01 & 0.8 & 1 & 1.2 & 1.4 & 1.6 \\ -0.15 & -0.69 & -1.02 & -1.75 & -2.8 & -2.9 \\ -0.1 & -0.514 & -0.92 & -1.13 & -1.4 & -1.5 \\ 0.053 & 0.53 & 0.53 & 0.53 & 0.53 & 0.6 \\ -0.06 & 0.36 & 0.42 & -0.2387 & -0.2387 & 1.112 \\ -0.27 & 0.84 & -0.0793 & 0.2128 & 0.2128 & 0.876 \\ 0.11 & 0.18 & -0.4473 & -0.1665 & -0.1665 & -0.234 \end{bmatrix} \quad (6-13)$$

Eq. (6-14) shows $\frac{dc_l^{mn}}{dF}$ where each column represents the changes due to an interval in the feed rate. Again, the first row of the matrix stands for the feed rate change for each column.

$$\frac{dc_l^{mn}}{dF} = \begin{bmatrix} 0 \rightarrow 0.01 & 0.01 \rightarrow 0.8 & 0.8 \rightarrow 1 & 1 \rightarrow 1.2 & 1.2 \rightarrow 1.4 & 1.4 \rightarrow 1.6 \\ -84.7 & -0.68 & -1.65 & -3.65 & -5.25 & -0.5 \\ 52 & -0.5241 & -2.03 & -1.05 & -1.35 & -0.5 \\ -53.11 & 0.61 & 0 & 0 & 0 & 0.35 \\ 17.83 & 0.542 & 0.2513 & -3.28 & -0.3673 & 7.12 \\ -45.08 & 1.4 & -4.6 & 1.46 & 0.8012 & 4.11 \\ 6.47 & 0.09 & -3.13 & -1.4 & 15.21 & -15.55 \end{bmatrix} \quad (6-14)$$

Therefore, according to Eq. (6-9), the matrix coefficient of process path function, $A_{Feed\ rate}$ is:

$$A_{Feed\ rate} = \begin{bmatrix} 50.61 & 12.28 & -10.51 & 4.56 & 30.65 & 81.29 \\ -31.71 & 77.05 & 65.32 & -1.69 & -18.98 & -51.17 \\ 31.89 & -77.53 & -66.06 & 1.33 & 19.34 & 51.47 \\ -11.22 & 27.1 & 22.46 & 6.58 & -66.81 & -17.11 \\ 22.53 & -62.6 & -54.41 & -2.54 & 16.37 & 40.26 \\ -24.94 & 68.8 & 70.65 & -9.2 & -18.96 & 0.8141 \end{bmatrix} \quad (6-15)$$

Similar to the case of feed rate, FE simulations for increasing the depth of cut and spindle speed were done by DEFORM™ 3D. The results were put into VPSC code and

texture coefficients were obtained as functions of changes in the depth of cut or spindle speed. Although, experimental observations showed that, due to recrystallization in the corresponding machined samples, the texture prediction may not be quite accurate. Fig. 6-7(a) shows the change in the microstructure attributes in the c_4^{11} - c_4^{12} - c_4^{14} space as a function of depth of cut. In Fig. 6-7(b), the portion of microstructure hull demarcated by the changes in depth of cut is illustrated.

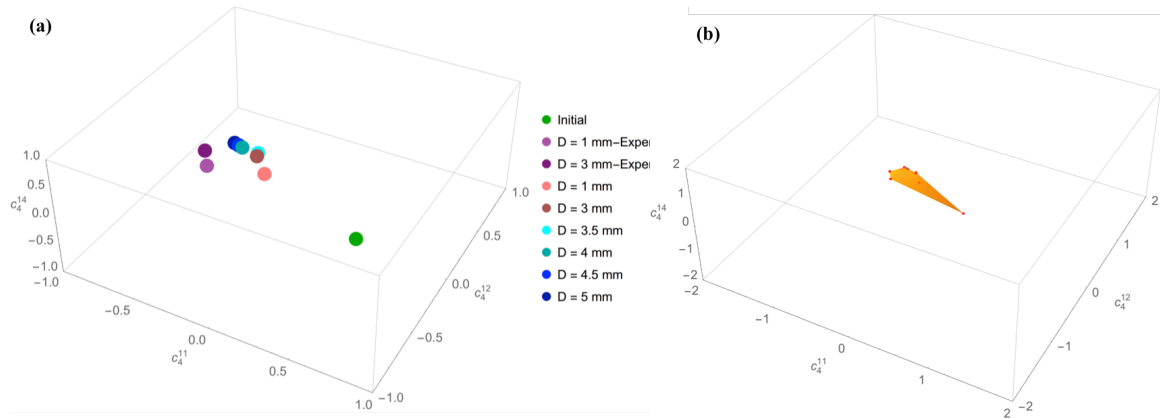


Fig. 6-7 The effects of increasing depth of cut in (a) The evolution of microstructure coefficients in AA7075 (b) a hyper-surface containing the possible processing paths leading to the possible microstructures. The red points show the simulation points.

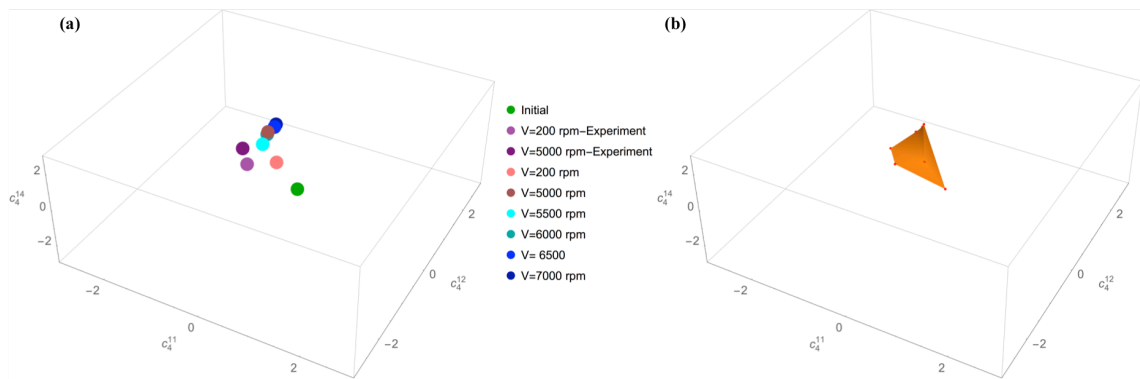


Fig. 6-8 The effects of increasing spindle speed (a) The evolution of microstructure coefficients (b) a hyper-surface containing the possible processing paths leading to the possible microstructures. The red points show the simulation points.

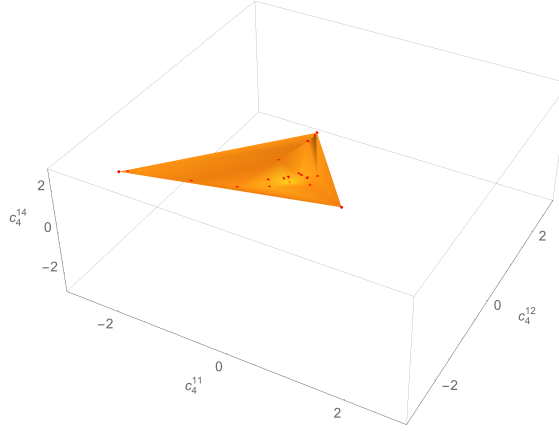


Fig. 6-9 congregation of all the microstructural paths obtained for simulations for the three process parameters. The hyper surface shows the possible microstructures. The red points show the simulation points

Similar to the case of feed rate, the process path function matrices for depth of cut and spindle speed, i.e. $A_{Depth\ of\ cut}$ and $A_{Spindle\ speed}$, can be easily obtained following the same procedure:

$$A_{Depth\ of\ cut} = \begin{bmatrix} 10.818 & 1.0946 & 64.67 & 4.247 & 9.82 & 3.69 \\ 0.7005 & -4.837 & 8.96 & 0.4827 & 1.25 & 0.52 \\ -2.7373 & 7.62 & -27.01 & -2.01 & -4.87 & -2.01 \\ -11.53 & 51.87 & -727.32 & -41.76 & -10.33 & -41.43 \\ -15.91 & 12.53 & -11.841 & -85.35 & -19.8 & -82.69 \\ 48.84 & -33.51 & 34.804 & 23.97 & 56.21 & 23.39 \end{bmatrix} \quad (6-16)$$

$$A_{Spindle\ speed} = \begin{bmatrix} 27.66 & -6.73 & 5.74 & 2.21 & 1.68 & 4.47 \\ 0.496 & -1.19 & -1.02 & 0.08 & 2.97 & 0.07 \\ -1.3388 & 3.255 & 2.77 & -0.04 & -18.13 & -6.14 \\ -32.74 & 79.61 & 67.95 & -0.13 & -9.91 & -5.29 \\ -53.69 & 13.05 & 14.45 & 18.05 & -32.67 & -8.17 \\ 15.74 & -38.27 & -32.67 & 54.1 & 95.78 & 25.47 \end{bmatrix} \quad (6-17)$$

Fig. 6-9 shows the closure containing all the experimental and computational points obtained for machining of AA7075. The closure demarcates all the physical points of the materials texture obtainable by starting from the initial point.

As mentioned in the earlier chapters, the discussed microstructural evolutions (i.e. both grain size and texture) lead to changes in materials properties. Micro-hardness below the machined surface is a suitable candidate for property measurements. Since a considerable refinement is observed in some of the samples, an increase in the hardness based on the Hall-Petch [132, 133] relation is expected. Eq. (6-18) demonstrates the Hall-Petch (HP) type of equations were a mechanical parameter (in this case hardness) is plotted against the average grain size powered to a materials constant M , which is reported to be very close to -0.5 for most known material systems[134, 135].

$$H = H_0 + k_H d^M \quad (6-18)$$

where H is the hardness of a polycrystalline material. k_H is the material's sensitivity to HP type behavior. H_0 is the offset of the plot of measured hardness vs. d^M . d represents the average grain size. Fig. 6-10 shows the HP plot with the assumption of $M=-0.5$. Therefore $H_0=146.69 \text{ HV}$ and $k_H = 247.65 \text{ HV}\sqrt{\mu\text{m}}$.

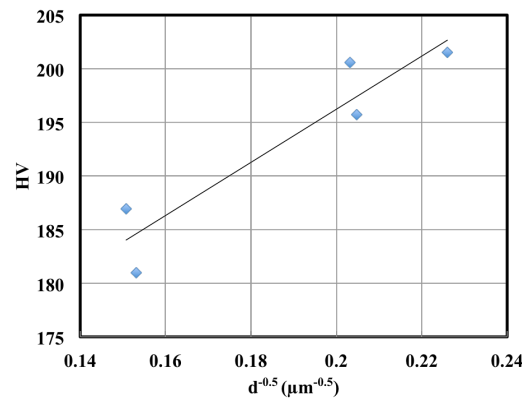


Fig. 6-10 The Hall-Petch plot for the hardness of the machined samples

It is important to note that the initial material is not considered in making the plot in Fig. 6-10. Since, its hardness (174.3 HV) was lower than all the machined cases and therefore violates the HP linear trend vs. $d^{-0.5}$. This phenomena is a good example of limitations of the HP effect in addition to the case of ultra-fine microstructures [136]. The HP-type relationships only consider the effects of grain boundaries on the properties, whereas it is well-established that in AA7075 system, at least four parameters contribute to changes in the hardness (and possibly other properties). According to Zhang et al. [137]:

$$H = H_{SS} + H_{GB} + H_P + H_{Dis} \quad (6-19)$$

where H_{SS} , H_{GB} , H_P and H_{Dis} respectively stand for the change in the hardness of AA 7075 due to the solid solution of Al and the alloying elements, the effects of grain boundaries (captured by HP relation), the effects of precipitations and the contribution of dislocations. The enhanced hardness at the machined surface that is observed regardless of grain refinement or growth, is possibly due to the increased dislocation density as a result of machining. In investigation of other properties (such as elastic moduli or plastic parameters), another important term, which represents the effects of crystallographic texture, should be added to Eq. (6-19).

6-4 Conclusions and future trends

Expansion of texture evolution in spectral form shows that machining remarkably changes the microstructure descriptors. The trend of the change in modeling and experimental results seems to follow paths in the microstructure space. For the case of feed rate, the two paths are completely close. The computational and experimental paths for depth of cut and spindle speed also seem to be converging.

6 additionally FE and VPSC combinations were performed for each process parameter to obtain the process path function. With the methodology explained above,

three different process path matrices for changing the feed rate, depth of cut and spindle speed in machining of AA 7075 were obtained. Determination of the process path matrix, should make the future assessment of texture evolution in the machining process, needless to any FE or VPSC simulations. However since the process paths are approximated without any consideration of recrystallization (which the applied VPSC model lacked), the outcome of the process path modeling is prone to discrepancy compared to the corresponding machining. Nonetheless, for the cases which recrystallization didn't occur or was negligible, the process path outcomes should be quite accurate.

The direction of future research should be towards incorporating the effects of the grain size into the microstructure space. In this regards, first the texture evolution code should accommodate recrystallization. Then the grain size distribution (e.g. the plot shown in Fig. 5-1) can be expanded in spectral form, for instance by Fourier series. The coefficient terms of the expansion can be treated in the same way as texture coefficients. Then, the conservation principle can be applied and the process path function can include both grain and texture evolution.

The next step in the future research is investigating the effects of all the above microstructural evolutions on the modifications in properties of the material. This would form the next section of the work necessary for implementing materials-affected manufacturing concept. In this regard, the preliminary work done by micro-hardness measurements needs to be extended towards other properties and if necessary in smaller scale; such measurement of elastic, plastic and creep properties by nano-indentation. In accurate modeling of properties evolutions, the effects of as many contributing factors (mentioned in Eq. (6-19)) as possible should be considered. In this regard different techniques such FE, analytical or statistical homogenization schemes or combinations of them can be applied[138].

7. MODELING THE EVOLUTION OF SECONDARY PHASES

7-1 The significance of precipitate refinement modeling

Many important engineering materials systems such as AA 7075, Ti64 and all other precipitation-hardened alloys and all types of composites are composed of more than one phase. Texture and grain modifications due to manufacturing, can be fairly assumed to completely represent the evolution of primary phase. Nonetheless, they provide no information about the potential evolution of secondary phases. The secondary phases of all the precipitation-hardened alloys (as well as Ti64) either is a brittle intermetallic or shows negligible inelastic deformation compared to the primary phase. Therefore, the main evolution of the secondary phase aggregates is refinement and redistribution [139-141], which can significantly change the properties and the response of the material[142-144].

Most on the modeling efforts on predicting precipitate refinement and redistribution is done through FEM. As an example, 2D modeling of refinement in multi-particle composites with rigorous finite element analysis is reported. The results showed for the first time that the previous assumption of splitting all the precipitates at their center lines is not valid all the times [145, 146]. The corresponding 3D modeling was reported a several years later [147] where the available computation power was high enough to handle such big models.

In order to address the evolutions of the second phase, a totally new approach, here so-called “the continuum mechanical” (CM) approach, is developed based on an early work on forces acting on solid ellipsoidal particles immersed in Newtonian fluids [148]. The purpose of this effort was to provide a much faster and still reliable technique compared to FEM, which is compatible with the whole scheme of materials-affected manufacturing and doesn’t add a considerable portion to the computational costs of the framework. This novel approach has not been used for inelastic deformation of solids and

is being introduced for the first time. The mathematical details of the proposed formalism is as follows:

7-2 Continuum-Mechanical approach towards determination of stress fields in secondary phase

It is assumed that a power law controls the plastic behavior of matrix. The Jonson-Cook model introduced in Eq. (4-11), can be fitted to a simple power law with the assumption of constant temperature and a maximum strain.

$$\sigma_{eq} = k \dot{\epsilon}_{eq}^n \quad (7-1)$$

where k and n are materials constants and $\dot{\epsilon}_{eq}$ and σ_{eq} respectively represent the equivalent stress and equivalent strain rate. Von-Mises yield criterion is assumed to control the yield behavior of the matrix. The equivalent strain rate is given by:

$$\dot{\epsilon}_{eq} = \sqrt{\frac{2}{3} \dot{\epsilon}_{ij} \dot{\epsilon}_{ij}} \quad (7-2)$$

According to the yield criterion, the equivalent stress is given by:

$$\sigma_{eq} = \sqrt{\frac{3}{2} S_{ij} S_{ij}} \quad (7-3)$$

It is assumed that flow rule of the matrix material can be represented by:

$$\dot{\epsilon}_{ij} = \frac{3 \dot{\epsilon}_{eq}}{2 \sigma_{eq}} S_{ij} \quad (7-4)$$

Where S_{ij} represent the deviatoric stress components. With the assumption of infinitesimal strain regime, the strain rate can be written:

$$\dot{\epsilon}_{ij} = \frac{1}{2} (v_{i,j} + v_{j,i}) \quad (7-5)$$

where v_i represents the velocity component and the comma notation is used for partial differentiation. Substituting eq. (7-1), (7-2), (7-3) and (7-5) into (7-4) and rearranging gives:

$$\sigma_{ij} = \sigma^h \delta_{ij} + \frac{k}{3} \dot{\epsilon}_{eq}^{n-1} (v_{i,j} + v_{j,i}) \quad (7-6)$$

Applying the equation of motion ($\sigma_{ij,i} = 0$) on eq. (7-6) and decomposition the stress tensor into deviatoric and hydrostatic results in:

$$\begin{aligned} \sigma_{ij,i} &= \sigma_{,i}^h + s_{ij,i} \\ &= \sigma_{,i}^h + \frac{\partial}{\partial x_i} \left(\frac{2}{3} k \dot{\epsilon}_{eq}^{n-1} \dot{\epsilon}_{ij} \right) \\ &= \sigma_{,i}^h + \frac{2}{3} k \left\{ (n-1) \dot{\epsilon}_{ij} \dot{\epsilon}_{eq}^{n-2} \frac{d\dot{\epsilon}_{eq}}{dx_i} + \dot{\epsilon}_{eq}^{n-1} \dot{\epsilon}_{ij,i} \right\} \\ &= \sigma_{,i}^h + \frac{2}{3} k \left\{ (n-1) \dot{\epsilon}_{ij} \dot{\epsilon}_{eq}^{n-2} \frac{2\dot{\epsilon}_{ij}}{3\dot{\epsilon}_{eq}} \dot{\epsilon}_{ij,i} + \dot{\epsilon}_{eq}^{n-1} \dot{\epsilon}_{ij,i} \right\} \\ &= \sigma_{,i}^h + \frac{2}{3} k \left\{ (n-1) \dot{\epsilon}_{eq}^{n-1} \dot{\epsilon}_{ij,i} + \dot{\epsilon}_{eq}^{n-1} \dot{\epsilon}_{ij,i} \right\} \\ &= \sigma_{,i}^h + \frac{2nk}{3} \dot{\epsilon}_{eq}^{n-1} \dot{\epsilon}_{ij,i} = \sigma_{,i}^h + \frac{nk}{3} \dot{\epsilon}_{eq}^{n-1} (v_{i,ji} + v_{j,ii}) = \sigma_{,i}^h + \frac{nk}{3} \dot{\epsilon}_{eq}^{n-1} v_{j,ii} = 0 \end{aligned} \quad (7-7)$$

With the assumption of incompressibility ($v_{k,k} = 0$), one can rewrite (7-7):

$$\sigma_{,i}^h + \eta \nabla^2 v_i = 0 \quad (7-8)$$

where:

$$\eta = \frac{nk}{3} \dot{\epsilon}_{eq}^{n-1} = \frac{nk}{3} \left\{ \frac{1}{6} (v_{i,j} + v_{j,i}) (v_{i,j} + v_{j,i}) \right\}^{\frac{n-1}{2}} \quad (7-9)$$

Eq. (7-8) should be solved in an ellipsoidal coordinate for the very specific geometry we are interested in. The PDE initially solved by Oberbeck [149] and the boundary conditions necessary for an ellipsoidal particle immersed in a Newtonian fluid was applied to it by Jeffery [148]. Here for inelastic solids, the viscosity term η ,

depends on the velocity unlike the Newtonian fluids which is a constant. Now, the procedure introduced by Jeffery [148] and explained by others[150, 151] and impose the necessary modifications for a solid is followed.

The boundary conditions are as follows: we assume that at infinity (far from the particle), the applied strain rate (or equivalently velocity) is distributed uniformly in the matrix.

$$v_i \Big|_{x_k=\infty} = v_i^\infty \quad (7-10)$$

Additionally, the hydrostatic stress at far distances from the particle is also known:

$$\sigma^h \Big|_{x_k=\infty} = \sigma^{h\infty} \quad (7-11)$$

If it is assumed that during the inelastic deformation of the particle/matrix interface remains perfect (no debonding occurs), then right at the interface both matrix and particle have to possess the same normal component of velocity. Considering, the elastic small deformation of the particle and comparatively large inelastic deformation of the matrix, the elastic deformation of the particle at its boundary is neglected. In other words, the normal components of the velocity is assumed to be zero. This assumption results in the third boundary condition which requires the velocity right at the interface only be rotational. But this rotational velocity is still position dependent and unknown.

$$v_i \Big|_{\text{interface}} = v_i^0 = \hat{\varepsilon}_{ijk} \omega_k x_j \equiv \omega \times x \quad (7-12)$$

where ω is the vorticity vector and $\hat{\varepsilon}_{ijk}$ represents the permutation tensor. Eq. (7-12) is a direct outcome of decomposition of the velocity gradient into rate of displacement and rate of rotation ($L_{ij} = D_{ij} + W_{ij}$) and assuming that the displacement part (D_{ij}) which corresponds to normal velocity is zero. Obviously, the above assumption is valid in a Cartesian coordinate with the origin at the center of the ellipsoid which means the coordinate moves with the motion of the ellipsoid. Eq. (7-12) can serve as a boundary condition but we need to notice that the vorticity vector, ω is unknown. For the sake of

simplicity, we assume the vorticity vector is uniform. This assumption still yields a position dependent velocity at the interface.

Looking at the PDE presented in eq. (7-8) and the boundary conditions, (7-10) to (7-12), one realizes that the problem is ill-posed. In the sense that there are two unknown functions, $\sigma^h(x_i)$ and $v_i(x_j)$ in one PDE and η depends on $v_i(x_j)$ according to (7-10). In addition, the numerical value of one of the boundary conditions (i.e. (7-12)) is not known yet.

Considering, the geometry of the problem (an ellipsoid in a medium), one realizes that the PDE (7-8) has to be solved for the “exterior of the ellipsoid”. Let’s assumed the equation of the ellipsoid in the aforementioned Cartesian coordinates (origin at the center of the ellipsoid) is given by:

$$\frac{x_1^2}{a_1^2} + \frac{x_2^2}{a_2^2} + \frac{x_3^2}{a_3^2} = 1 \quad (7-13)$$

The solution to the homogenous for the PDE of Eq. (7-9) (i.e. $\nabla^2 v_i(x_j) = 0$) outside the ellipsoid (7-13) is already available [150-152]:

The functions that Ω and χ_i are solutions to the homogenous from of Eq. (7-9), that is:

$$\begin{aligned} \nabla^2 \Omega &= 0 \\ \nabla^2 \chi_i &= 0 \end{aligned} \quad (7-14)$$

Ω and χ_i ($i=1,2,3$) are defined in the confocal ellipsoidal coordinate in the following way. In the ellipsoidal coordinate, λ is the positive root of:

$$\frac{x_1^2}{a_1^2 + \lambda} + \frac{x_2^2}{a_2^2 + \lambda} + \frac{x_3^2}{a_3^2 + \lambda} = 1 \quad (7-15)$$

which means that if $\lambda = 0$ we are at the interface of the ellipsoid and matrix and if $\lambda > 0$ we are in the matrix on an ellipsoidal surface. Ω is defined as:

$$\Omega = \int_{\lambda}^{\infty} \left(\frac{x_1^2}{a_1^2 + \lambda} + \frac{x_2^2}{a_2^2 + \lambda} + \frac{x_3^2}{a_3^2 + \lambda} - 1 \right) \frac{d\lambda}{\Delta} \quad (7-16)$$

where

$$\Delta = \sqrt{(a_1^2 + \lambda)(a_2^2 + \lambda)(a_3^2 + \lambda)} \quad (7-17)$$

Now, if we put:

$$\alpha_1 = \int_{\lambda}^{\infty} \frac{d\lambda}{(a_1^2 + \lambda)} \quad (7-18)$$

$$\alpha'_1 = \int_{\lambda}^{\infty} \frac{d\lambda}{(a_2^2 + \lambda)(a_3^2 + \lambda)\Delta} \quad (7-19)$$

$$\alpha''_1 = \int_{\lambda}^{\infty} \frac{\lambda d\lambda}{(a_2^2 + \lambda)(a_3^2 + \lambda)\Delta} \quad (7-20)$$

Then the χ_i functions can be defined in the following way:

$$\chi_1 = \alpha'_1 x_2 x_3, \quad \chi_2 = \alpha'_2 x_1 x_3, \quad \chi_3 = \alpha'_3 x_2 x_1 \quad (7-21)$$

α'_2, α'_3 and α''_2, α''_3 are evaluated in the same way as (7-20) and (7-21).

Based on the above solutions for the homogenous PDE in the confocal ellipsoidal coordinates, Oberbeck [149] proposed a solution for the original PDE (7-8) in the Cartesian coordinates. The technique was later modified by Jeffery [148] and is fully explained by Lamb [150]. According to Jeffery[148], the solution to (7-8) is “assumed to be possible” to be written in the form of partial derivatives of Ω and χ_i in the following form:

$$v = v^{\infty} + \nabla(R \cdot \chi) + \nabla \times (U \circ \chi) - A \cdot \nabla \Omega + \nabla \cdot (\nabla \Omega \cdot A \cdot x) \quad (7-22)$$

where $R = (R_1, R_2, R_3)$, $U = (U_1, U_2, U_3)$ are constant vector. $\chi = (\chi_1, \chi_2, \chi_3)$ is a

considered as a vector and A is a 2nd rank tensor of constants with the form:

$$A = \begin{bmatrix} A_{11} & A_{12} & A_{13} \\ A_{21} & A_{22} & A_{23} \\ A_{31} & A_{32} & A_{33} \end{bmatrix} \quad (7-23)$$

By $U \circ \chi$, we mean a vector with the form $U \circ \chi = (U_1 \chi_1, U_2 \chi_2, U_3 \chi_3)$.

The above form satisfies the boundary conditions (7-10 to 7-12). It can be verified by inspection that all terms in (7-23) tend to zero as $x \rightarrow \infty$. Jeffery [148] continues to derive the form of hydrostatic pressure which is valid only for the case of Newtonian (constant viscosity) fluids while according to (7-10), the η parameter for the case of inelastic deformation of a solid is not constant. Therefore, here we need to “modify” Jeffery’s solution to accommodate the non-constant “viscosity parameter” for inelastic deformation of solids. For this purpose, if we double differentiate eq. (7-22) and by noting that $\nabla^2 \Omega = \nabla^2 \chi_i = 0$, we have:

$$\nabla^2 v_i = 2 \left\{ \frac{\partial}{\partial x_i} \left(A_{11} \frac{\partial^2 \Omega}{\partial x_1^2} + A_{22} \frac{\partial^2 \Omega}{\partial x_2^2} + A_{33} \frac{\partial^2 \Omega}{\partial x_3^2} + \right. \right. \\ \left. \left. (A_{12} + A_{21}) \frac{\partial^2 \Omega}{\partial x_1 \partial x_2} + (A_{13} + A_{31}) \frac{\partial^2 \Omega}{\partial x_1 \partial x_3} + (A_{23} + A_{32}) \frac{\partial^2 \Omega}{\partial x_2 \partial x_3} \right) \right\} \quad (7-24)$$

If we substitute into (7-24), we have:

$$\eta(v_k) \nabla^2 v_i = \frac{\partial \sigma^h}{\partial x_i} \rightarrow \\ 2\eta \left\{ \frac{\partial}{\partial x_i} \left(A_{11} \frac{\partial^2 \Omega}{\partial x_1^2} + A_{22} \frac{\partial^2 \Omega}{\partial x_2^2} + A_{33} \frac{\partial^2 \Omega}{\partial x_3^2} + \right. \right. \\ \left. \left. (A_{12} + A_{21}) \frac{\partial^2 \Omega}{\partial x_1 \partial x_2} + (A_{13} + A_{31}) \frac{\partial^2 \Omega}{\partial x_1 \partial x_3} + (A_{23} + A_{32}) \frac{\partial^2 \Omega}{\partial x_2 \partial x_3} \right) \right\} = \frac{\partial \sigma^h}{\partial x_i} \quad (7-25)$$

Therefore:

$$\sigma^h = 2 \int \left[\eta \left\{ \frac{\partial}{\partial x_i} \left(A_{11} \frac{\partial^2 \Omega}{\partial x_1^2} + A_{22} \frac{\partial^2 \Omega}{\partial x_2^2} + A_{33} \frac{\partial^2 \Omega}{\partial x_3^2} + \right. \right. \right. \\ \left. \left. \left. (A_{12} + A_{21}) \frac{\partial^2 \Omega}{\partial x_1 \partial x_2} + (A_{13} + A_{31}) \frac{\partial^2 \Omega}{\partial x_1 \partial x_3} + (A_{23} + A_{32}) \frac{\partial^2 \Omega}{\partial x_2 \partial x_3} \right) \right\} \right] dx_i \quad (7-26)$$

Now, noting the fact that we know the function forms of η and v_k (from (7-9) and (7-22)) then we can integrate eq. (7-26) and find $\sigma^h(x_i)$, if we can find the constants defined in (7-24). In order to determine the constants we can follow the procedure explained by Jeffery[148] and Lamb [150] where we impose the boundary condition Eq. (7-11) and compressibility on Eq. (7-22). Using the uniformity assumption of far field velocity Eq. (7-12), will result in a 15-equation 15-unknown system, which yields the constant coefficients and fully identifies the velocity field in the matrix adjacent to the ellipsoidal particle.

Following what is mentioned above, the velocity v and the hydrostatic stress σ^h , in the vicinity of the elastic precipitate, in the inelastic solid is given by Eq. (7-22) and (7-26). Now since we have the velocity of the solid matrix in the neighborhood of a particle, through straightforward continuum mechanical calculations, we can find the traction exerted on the boundary of the ellipsoid:

$$T_i = P \left\{ \sigma^h \frac{x_r}{a_s^2} \delta_{rs} \delta_{ij} + \frac{\eta}{n} (v_{i,j} + v_{j,i}) \frac{x_r}{a_s^2} \delta_{rs} \right\} \quad (7-27)$$

where

$$P = \frac{1}{\sqrt{\frac{x_1^2}{a_1^4} + \frac{x_2^2}{a_2^4} + \frac{x_3^2}{a_3^4}}} \quad (7-28)$$

n is the unit normal to the surface of ellipsoidal precipitate. In order to determine the position dependent stress at any location at the interior of the ellipsoidal particle, we cut an arbitrary section in the ellipsoid as shown schematically by Fig. 7-1. We notice that any cross-section to an ellipsoid always results in an elliptical surface [153]. If $n^* = (n_1^*, n_2^*, n_3^*)$ is the unit normal to the arbitrary elliptical cross-section and A_E its surface area, as depicted in Fig. 7-1 ; then the balance of force results in:

$$A_E \sigma_{n^*} + \int_S T \cdot n^* dS = 0 \quad (7-29)$$

Since, A_E and n^* depend on position and orientation of the sectioning, the normal stress σ_{n^*} can be determined at any position inside the ellipsoid. Now, If n_x and n_y (schematically shown in Fig. 7-2; note that n^* , n_x and n_y are mutually orthogonal) represent the unit normal vectors along the direction of major and minor semi-axes of the intersected ellipse, then similar to the normal stress, the shear stress on the plane of intersection can be obtained:

$$A_E \tau_x + \int_S T \cdot n_x dS = 0 \quad (7-30)$$

$$A_E \tau_y + \int_S T \cdot n_y dS = 0 \quad (7-31)$$

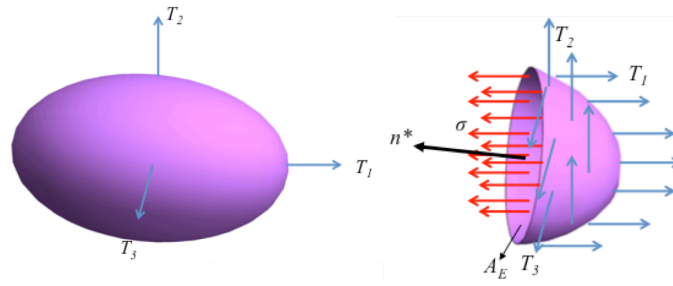


Fig. 7-1 Schematic sectioning of the ellipsoidal particle to determine the stress. Blue arrows represents traction and red arrow represent stress. The black arrow represents the unit normal to the cross-section.

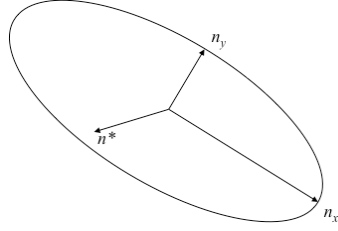


Fig. 7-2. Schematic illustration of the elliptical surface of cross sectioning and ellipsoid

7-3 FEA Verification

For the purpose of validation, the stress fields inside the precipitate will be numerically calculated by FEM (for this purpose, ABAQUS™ version 6.13 was used) to compare and validate the continuum mechanical (CM) results. Here, 2D FEM model results are compared to the 2D continuum mechanical counterpart. In running the FE simulations, properties of AA7075 (i.e. constitutive law Eq. (7-1) and yield stress) were used to serve the purpose. As required by the above formalism, a rate-dependent power law behavior (i.e. creep) and a von-Mises yielding characteristic was applied to the matrix. The particle is assumed a rigid precipitate (stabilized η precipitates - elastic deformation ignored). Verification of the CM model was performed for two simple loading cases, uniaxial tension and pure shear at room temperature. The element sizes were in the range of 0.01 to 0.05 times the side of the cell shown in Fig. 7-3.

Fig. 7-3 compares the results obtained by the CM and FEM for uniaxial tensile loading. The angle θ , represents the orientation of the particle with respect to the vertical axis. According to Fig. 7-3 (a), the maximal value of the first principal stress occurs at the center of the particle when the orientation angle $\theta = 0^\circ$. The same phenomena in addition to a similar level of stress, are predicted by FEM results shown in Fig. 7-3(c). Also, increasing the strain rate increases the level of stress that the precipitate is experiencing. Fig. 7-3(b) illustrates the constant-stress contours of the first principal stress for $\theta = 45^\circ$. In this case, the maximal stress occurs at a distance from the center of

the particle, which is validated by FEM results shown in Fig. 703(d). Similar to the previous case, the magnitude of stress is close in the two cases.

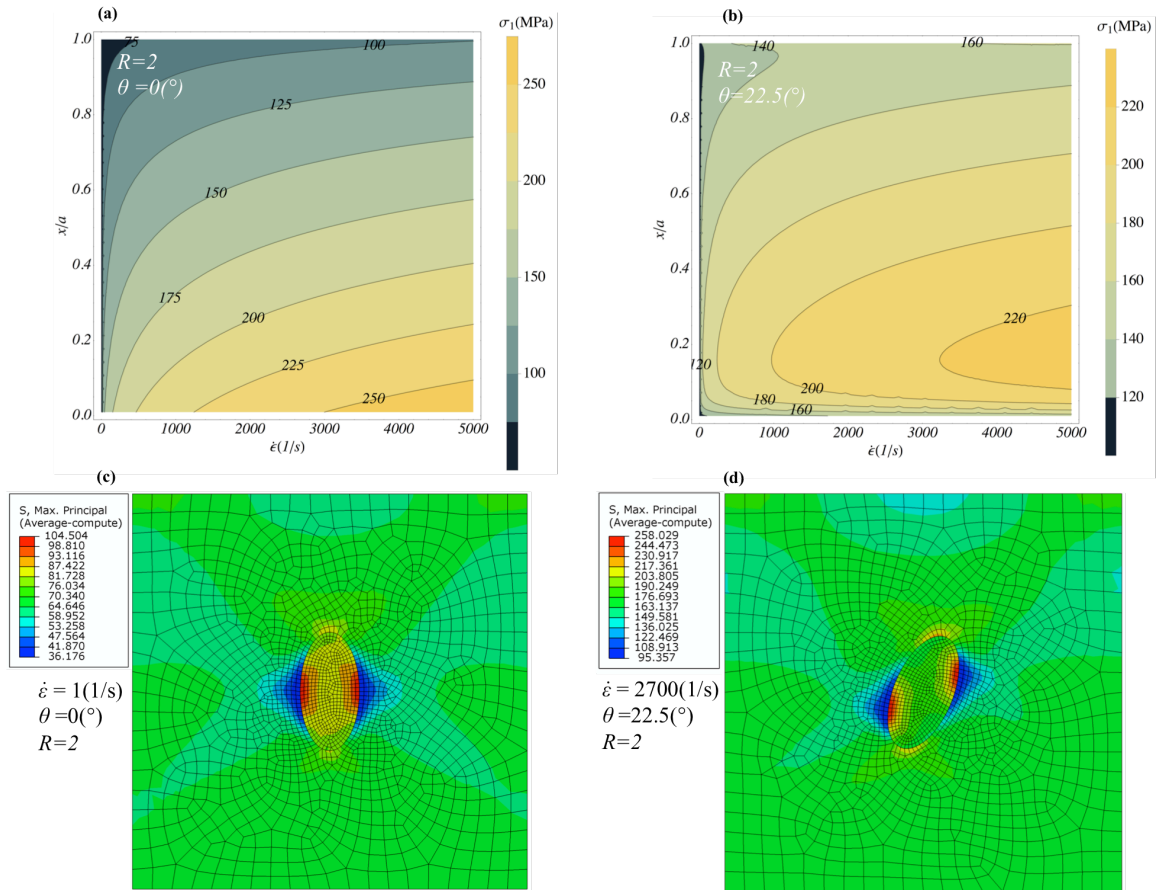


Fig. 7-3 constant stress contours of the first principal stress in uniaxial loading for (a) $\theta = 0^\circ$ and (b) $\theta = 45^\circ$. x represents the position in the particle and a is the major semi-axis of the elliptical particle. (c) and (d) are FEM simulations respectively corresponding to (a) and (b).

Fig. 7-4 compares the results of the continuum mechanical and FEM results for the case of pure shear. Analogous to the case of uniaxial tension, the CM and FEM approaches predict the same position of occurrence of a maximized stress and similar numerical values. It is clear from Fig. 7-3 and 7-4, for any combination of process parameters (here the applied strain rate and orientation of the particle) an independent FE simulation should be done, however the CM method yields results for all the possible cases at once. Therefore, in order to completely validate the CM approach, several FE simulations were run. The results are compared to CM outcomes in Fig. 7-5 and 7-6.

Important to note that FEM yields stress values for each element while the CM method gives a type of “averaged stress” acting on a plane. Therefore, in comparing FEM and CM, the maximal, minimal and average FEM stresses acting on the plane of the maximum first principal stresses are compared. s numerical value in pure shear,. Fig. 7-5 compares the results obtained by CM and FEM in pure shear, which again proves the consistency of the newly developed model with FEM. Fig. 7-6 a comparison for shear. According to Fig. 7-5 and 7-6, the values predicted by the CM mode always falls between the minimum and maximum values predicted by FEM, although not necessarily the average. These results confirm the reliability of the proposed CM technique.

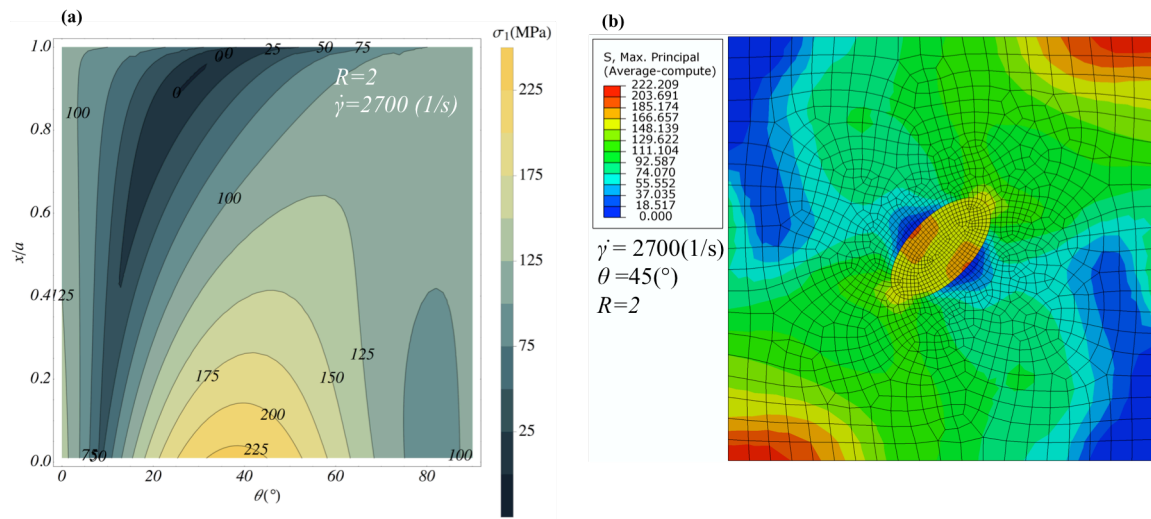


Fig. 7-4 constant stress contours of the first principal stress in pure shear at constant shear strain rate as a function of θ ; x represents the position in the particle and a is the major semi-axis of the elliptical particle. (b) the FEM simulation result for the case pure shear loading at $\theta=45^\circ$ and shear strain rate of 2700 s^{-1} .

7-4 Conclusions and future trends

A novel approach is proposed to determine the position dependent stress fields at the interior of secondary phase precipitates, in loading of the bulk body of the material. The approach is founded on a closed-form solution to the equation motion of the material surrounding the precipitate. Therefore, the computation time is significantly reduced

compared to a conventional technique such as FEM. Since the novel methodology considers the velocity of the material surrounding the precipitates, it can also determine the redistribution of the precipitate due to bulk deformation of the whole body.

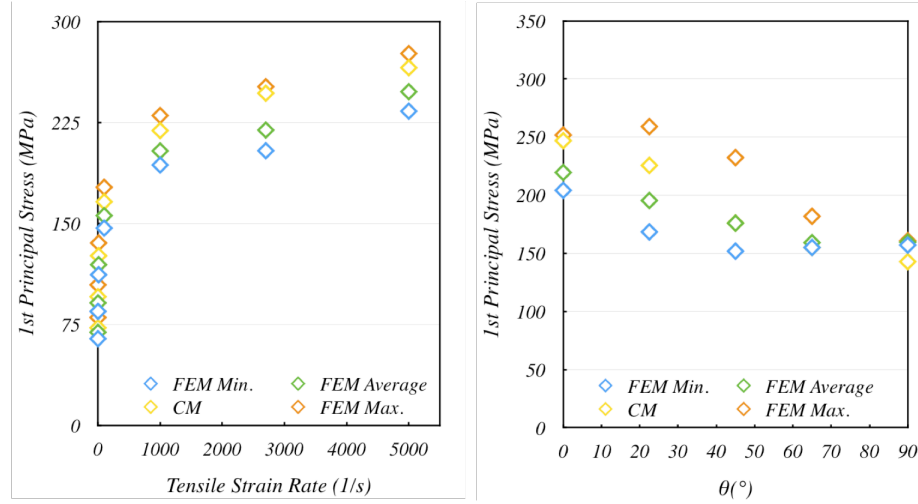


Fig. 7-5 Comparison of CM and FEM approaches in uniaxial tension

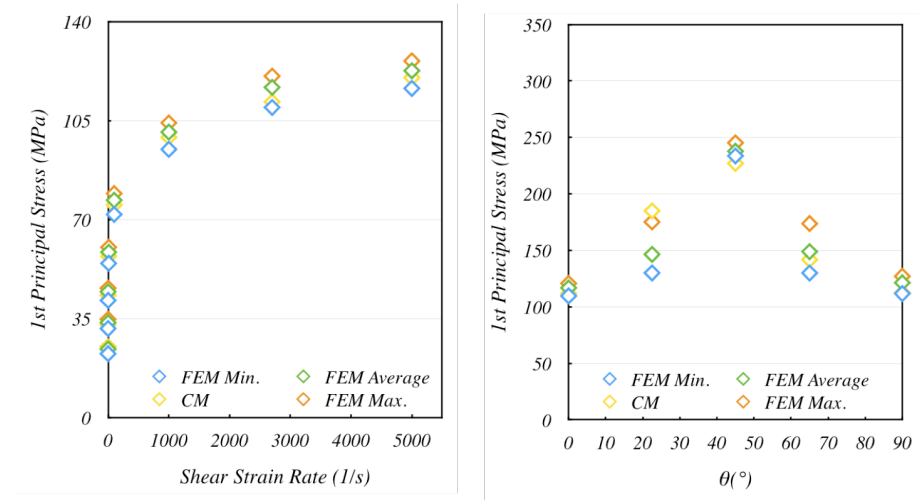


Fig. 7-6 Comparison of CM and FEM approaches in pure shear

Additionally, the reliability of the results is tested with FE simulations in uniaxial tensile and pure shear loading of AA 7075 with the assumption of the presence of a large-enough η precipitate.

The direction of the future research should be first towards applying a macroscopic failure criterion (e.g. Griffith's criterion [154, 155]) to predict the mode of precipitate refinement, after obtaining the position-dependent stress fields inside it. More importantly, this modeling formalism should be incorporated into the computational core of the materials-affected manufacturing framework, while investigating multi-phase materials. The best place to add the model is the crystal plasticity step where strain and strain rates in each crystallite are inevitably calculated. Therefore if the crystallite contains a precipitate, the loading input to the refinement model is the strain rate that the crystallite is experiencing rather than the externally applied strain rate. The precipitates along the grain boundaries can be assumed to experience an average value exerted by the adjacent grains. Therefore, in connection to the future trends suggested for previous chapters; the crystal plasticity model used in materials-affected manufacturing should be modified to at least accommodate two other phenomena, namely recrystallization and precipitate refinement.

8. CONCLUDING REMARKS AND OUTLOOK

This work reports the initial results of obtaining a comprehensive toolset capable of correlating manufacturing process parameters to microstructural characteristics through robust computational modeling validated by solid experimentations. Aluminum alloy 7075 samples were machined by turning process, at different conditions by changing the depth of cut, feed rate and spindle speed. The thermo-mechanical loads (i.e. stresses, strains and strain rates, temperature, etc.) induced to the material by the turning process, are obtained using finite element analysis.

According to the results; depending on the machining conditions, the applied strain and strain rate on the surface are respectively in the range of ~ 4 to ~ 6 and in the order $\sim 10^4 \text{ s}^{-1}$. Based on previous published works in the literature, these values seem reasonable, since machining is an ultra-high strain, ultra-high strain rate process. Increasing the depth of cut seems to affect the strain more than the strain rate, while increasing the feed rate intensifies the strain rate exerted to the material. Increasing the spindle speed magnifies the levels of applied temperature and strain rate. Furthermore, finite element results indicate that the depth of penetration of strain and strain rate fields is about $\sim 200 \text{ }\mu\text{m}$ in most cases. In addition, the temperature induced to the material is well above the recrystallization temperature in many cases.

Experimental texture analysis of the as-received material shows a characteristic close to a randomly oriented microstructure. The initial material shows a high intensity of (112) planes in inverse pole figure plots. Amongst the texture fibers, the β fiber shows the highest intensity around $\varphi_2 \approx 60^\circ$ with an intensity of ~ 8 times random. The average grain size of the as-received material is $\sim 31.6 \text{ }\mu\text{m}$ with a standard deviation of $23.1 \text{ }\mu\text{m}$ which shows a high degree of non-uniformity in the microstructure of the as-received material.

According to experimental results, machining at the low level of depth of cut and feed rate and the high level of speed results in development of a texture component mainly recognized by a hump in the β fiber in the range $80^\circ \leq \varphi_2 \leq 90^\circ$. Computational simulation of texture evolution performed by the viscoplastic self-consistent crystal plasticity scheme also predicts the same texture component.

Increasing the depth of cut to the high level while keeping the feed rate at its low value, increases the discrepancy between simulations and experiments. While in the case of increasing the feed rate to a high level, the prediction of simulation and experimental results are entirely close. The peak values for the α and β fibers are at respectively φ_1 and $\varphi_2 \approx 90^\circ$ and the rest of humps and valleys in texture fibers are the same in computational predictions and experiments.

Experimental observations on the grain evolution due to machining, suggest that remarkable changes occur below the machined surface. Grain growth occurs in the samples machined at the lower depths of cut. On the other hand, promotes a severe recrystallization. Reduced spindle speed alleviates recrystallization resulting in larger grains compared to the intensely recrystallized cases.

The recrystallized grains possess a different texture characteristic compared to grains prior to recrystallization. However, the crystal plasticity model, which was used for capturing texture evolution, is not capable of incorporating recrystallization. Therefore, the texture that the model predicts for recrystallized cases show a discrepancy compared to experimental results.

In order to systematically follow microstructural evolutions, the orientation distribution functions obtained for the samples and their corresponding simulations were expanded in a spectral form. The outcome shows that machining remarkably changes the microstructure descriptor coefficients. The trend of the change in modeling and experimental results seems to follow paths in the microstructure space. For the case of

increasing the feed rate, the two paths are completely close. Additionally, The computational and experimental paths for depth of cut and spindle speed also seem to be converging.

With the aid of complementary finite element simulations combined with crystal plasticity modeling, three different process path functions for changing the feed rate, depth of cut and spindle speed in machining of aluminum alloy 7075 were obtained. Determination of the process path function makes future assessments of texture evolution of aluminum alloy 7075 during machining, needless to any finite element or crystal plasticity simulations.

In order to account for possible evolutions of the secondary phases, a novel approach is proposed to determine the position dependent stress fields at the interior of secondary phase precipitates, during loading of the bulk body of the material. The approach is founded on a closed-form solution to the equation of motion for the material surrounding the precipitate. Therefore, the computation time is significantly reduced compared to a conventional technique such as finite element method. Additionally, the reliability of the results is tested with finite element simulations in uniaxial tensile and pure shear loading of AA 7075 with the assumption of the presence of a large-enough η precipitate.

To fully implement the materials-affected manufacturing framework, which this research work form its first part, several other tasks need to be accomplished. The most important one is to adjust the crystal plasticity model to incorporate any possible recrystallization and grain growth, which was the main source of discrepancy in the current computational and experimental results. Additionally, the grain size distribution of the material should be also expanded in spectral form; to be able to express the evolution of grain size by means of microstructure descriptor coefficients and mathematically derive the complete process path functions. Along the same lines, the second phase evolution framework should be completed (to account for macroscopic

failure of precipitates and their redistribution) and inserted into the crystal plasticity code alongside recrystallization.

The next step in future research is investigating the effects of all the above microstructural evolutions on the material's properties. This section of the work again requires experimental validations. In accurate modeling of properties evolutions, the effects of as many contributing factors as possible should be considered.

Finally, the last step in completing the materials-affected manufacturing scheme should be taken, by incorporating the iteratively updated material properties as inputs to manufacturing models and simultaneously evolving materials microstructure and properties due to manufacturing loads.

REFERENCES

1. Mallock, A., *The action of cutting tools*. Proceedings of the Royal Society of London, 1881. **33**(216-219): p. 127-139.
2. Fergani, O. and S.Y. Liang, *Materials-affected manufacturing*. Manufacturing Letters, 2013. **1**(2): p. 74-77.
3. Marashi, P., M. Pouranvari, S. Amirabdollahian, A. Abedi, and M. Goodarzi, *Microstructure and failure behavior of dissimilar resistance spot welds between low carbon galvanized and austenitic stainless steels*. Materials Science and Engineering: A, 2008. **480**(1): p. 175-180.
4. Zum Gahr, K.-H., *Microstructure and wear of materials*. Vol. 10. 1987: Elsevier.
5. Christ, H.-J. and H. Mughrabi, *Microstructure and fatigue*, in *Low Cycle Fatigue and Elasto-Plastic Behaviour of Materials—3*. 1992, Springer. p. 56-69.
6. Altintas, Y., *Manufacturing automation: metal cutting mechanics, machine tool vibrations, and CNC design*. 2012: Cambridge university press.
7. Shankar, M.R., S. Chandrasekar, A.H. King, and W.D. Compton, *Microstructure and stability of nanocrystalline aluminum 6061 created by large strain machining*. Acta Materialia, 2005. **53**(18): p. 4781-4793.
8. Shivpuri, R., J. Hua, P. Mittal, A. Srivastava, and G. Lahoti, *Microstructure-mechanics interactions in modeling chip segmentation during titanium machining*. CIRP Annals-Manufacturing Technology, 2002. **51**(1): p. 71-74.
9. Bedekar, V., R. Shivpuri, R. Chaudhari, and R.S. Hyde, *Nanostructural evolution of hard turning layers in response to insert geometry, cutting parameters and material microstructure*. CIRP Annals-Manufacturing Technology, 2013. **62**(1): p. 63-66.
10. Lin, J., D. Balint, and M. Pietrzyk, *Microstructure evolution in metal forming processes*. 2012: Elsevier.
11. Bontcheva, N. and G. Petzov, *Microstructure evolution during metal forming processes*. Computational materials science, 2003. **28**(3): p. 563-573.
12. Dieter, G.E. and D. Bacon, *Mechanical metallurgy*. Vol. 3. 1986: McGraw-Hill New York.
13. Li, D., H. Garmestani, and S. Schoenfeld, *Evolution of crystal orientation distribution coefficients during plastic deformation*. Scripta materialia, 2003. **49**(9): p. 867-872.

14. Barnett, M.R., *Influence of deformation conditions and texture on the high temperature flow stress of magnesium AZ31*. Journal of light metals, 2001. **1**(3): p. 167-177.
15. Zhang, S., W. Hu, R. Berghammer, and G. Gottstein, *Microstructure evolution and deformation behavior of ultrafine-grained Al–Zn–Mg alloys with fine η precipitates*. Acta Materialia, 2010. **58**(20): p. 6695-6705.
16. Rhodes, C., M. Mahoney, W. Bingel, R. Spurling, and C. Bampton, *Effects of friction stir welding on microstructure of 7075 aluminum*. Scripta materialia, 1997. **36**(1): p. 69-75.
17. Babu, B. and L.-E. Lindgren, *Dislocation density based model for plastic deformation and globularization of Ti-6Al-4V*. International Journal of Plasticity, 2013. **50**: p. 94-108.
18. Ding, H. and Y.C. Shin. *Dislocation density-based grain refinement modeling of orthogonal cutting of commercially pure titanium*. in *Proceedings of the 2011 ASME International Manufacturing Science and Engineering Conference, MSEC2011-50220, American Society of Mechanical Engineers, Corvallis, OR, USA*. 2011.
19. Gray, B., J. Brocklehurst, and A. McFarlane, *The irradiation induced plasticity in graphite under constant stress*. Carbon, 1967. **5**(2): p. 173-180.
20. Eklund, E.A., R. Bruinsma, J. Rudnick, and R.S. Williams, *Submicron-scale surface roughening induced by ion bombardment*. Physical review letters, 1991. **67**(13): p. 1759.
21. Li, L.-x., G. Wang, J. Liu, and Z.-q. Yao, *Flow softening behavior and microstructure evolution of Al–5Zn–2Mg aluminum alloy during dynamic recovery*. Transactions of Nonferrous Metals Society of China, 2014. **24**(1): p. 42-48.
22. Souza, R., E. Silva, A. Jorge Jr, J. Cabrera, and O. Balancin, *Dynamic recovery and dynamic recrystallization competition on a Nb-and N-bearing austenitic stainless steel biomaterial: Influence of strain rate and temperature*. Materials Science and Engineering: A, 2013. **582**: p. 96-107.
23. Rollett, A., F. Humphreys, G.S. Rohrer, and M. Hatherly, *Recrystallization and related annealing phenomena*. 2004: Elsevier.
24. Courbon, C., T. Mabrouki, J. Rech, D. Mazuyer, F. Perrard, and E. D'Eramo, *Towards a Physical FE Modelling of a Dry Cutting Operation: Influence of Dynamic Recrystallization When Machining AISI 1045*. Procedia CIRP, 2013. **8**: p. 515-520.

25. Ni, H., M. Elmadagli, and A. Alpas, *Mechanical properties and microstructures of 1100 aluminum subjected to dry machining*. Materials Science and Engineering: A, 2004. **385**(1): p. 267-278.
26. M'Saoubi, R., T. Larsson, J. Outeiro, Y. Guo, S. Suslov, C. Saldana, and S. Chandrasekar, *Surface integrity analysis of machined Inconel 718 over multiple length scales*. CIRP Annals-Manufacturing Technology, 2012. **61**(1): p. 99-102.
27. Ghosh, S. and V. Kain, *Microstructural changes in AISI 304L stainless steel due to surface machining: Effect on its susceptibility to chloride stress corrosion cracking*. Journal of nuclear materials, 2010. **403**(1): p. 62-67.
28. Ding, H., N. Shen, and Y.C. Shin, *Modeling of grain refinement in aluminum and copper subjected to cutting*. Computational Materials Science, 2011. **50**(10): p. 3016-3025.
29. Rotella, G., O.W. Dillon Jr, D. Umbrello, L. Settineri, and I.S. Jawahir, *Finite element modeling of microstructural changes in turning of AA7075-T651 Alloy*. Journal of Manufacturing Processes, 2013. **15**(1): p. 87-95.
30. Rotella, G. and D. Umbrello, *Numerical simulation of surface modification in dry and cryogenic machining of AA7075 alloy*. Procedia CIRP, 2014. **13**: p. 327-332.
31. Jafarian, F., M.I. Ciaran, D. Umbrello, P. Arrazola, L. Filice, and H. Amirabadi, *Finite element simulation of machining Inconel 718 alloy including microstructure changes*. International Journal of Mechanical Sciences, 2014. **88**: p. 110-121.
32. Swaminathan, S., M.R. Shankar, S. Lee, J. Hwang, A.H. King, R.F. Kezar, B.C. Rao, T.L. Brown, S. Chandrasekar, and W.D. Compton, *Large strain deformation and ultra-fine grained materials by machining*. Materials Science and Engineering: A, 2005. **410**: p. 358-363.
33. Campbell, C., L. Bendersky, W. Boettinger, and R. Ivester, *Microstructural characterization of Al-7075-T651 chips and work pieces produced by high-speed machining*. Materials Science and Engineering: A, 2006. **430**(1): p. 15-26.
34. Basu, S. and M.R. Shankar, *Crystallographic Textures Resulting from Severe Shear Deformation in Machining*. Metallurgical and Materials Transactions A, 2015. **46**(2): p. 801-812.
35. Arısoy, Y.M. and T. Özel, *Prediction of Machining Induced Microstructure in Ti-6Al-4V Alloy using 3-D FE-Based Simulations: Effects of Tool Micro-geometry, Coating and Cutting Conditions*. Journal of Materials Processing Technology, 2014.
36. Totten, G.E. and D.S. MacKenzie, *Handbook of Aluminum: Vol. 1: Physical Metallurgy and Processes*. Vol. 1. 2003: CRC Press.

37. Epstein, S.G., *Aluminum and Its Alloys*. 1994, Washington D.C.: Aluminum Association.
38. *Aluminum statistics*. Available from: <http://www.world-aluminium.org/statistics/>.
39. Quan, G.-z., Y.-p. Mao, G.-s. Li, W.-q. Lv, Y. Wang, and J. Zhou, *A characterization for the dynamic recrystallization kinetics of as-extruded 7075 aluminum alloy based on true stress–strain curves*. Computational Materials Science, 2012. **55**: p. 65-72.
40. Yang, X., H. Miura, and T. Sakai, *Continuous dynamic recrystallization in a superplastic 7075 aluminum alloy*. Materials Transactions, 2002. **43**(10): p. 2400-2407.
41. Mueller, M., I. Bernstein, and A. Thompson, *Recovery behavior of hydrogen charged 7075-T6 Aluminum*. Scripta metallurgica, 1983. **17**(8): p. 1039-1042.
42. Hidalgo-Manrique, P., C. Cepeda-Jiménez, A. Orozco-Caballero, O. Ruano, and F. Carreño, *Evolution of the microstructure, texture and creep properties of the 7075 aluminium alloy during hot accumulative roll bonding*. Materials Science and Engineering: A, 2014. **606**: p. 434-442.
43. Field, D.P., T.W. Nelson, Y. Hovanski, and D.F. Bahr, *Texture effects on corrosion behavior of friction stir welded 7075 aluminum*. Friction Stir Welding and Processing, 2001: p. 83-91.
44. Tabei, A., O. Fergani, H. Garmestani, and S.Y. Liang. *Analysis of Micro-Texture and Grain Size Distributions in Machined Aluminum Alloy 7075*. in *Advanced Materials Research*. 2014.
45. Fergani, O., A. Tabei, H. Garmestani, and S.Y. Liang, *Prediction of polycrystalline materials texture evolution in machining via Viscoplastic Self-Consistent modeling*. Journal of Manufacturing Processes, 2014. **16**(4): p. 543-550.
46. Chen, J., L. Zhen, S. Yang, W. Shao, and S. Dai, *Investigation of precipitation behavior and related hardening in AA 7055 aluminum alloy*. Materials Science and Engineering: A, 2009. **500**(1): p. 34-42.
47. Palmer, W. and P. Oxley, *Mechanics of orthogonal machining*. Proceedings of the Institution of Mechanical Engineers, 1959. **173**(1): p. 623-654.
48. Lee, E. and B. Shaffer, *The theory of plasticity applied to a problem of machining*. 1949: Division of Applied Mathematics, Brown.
49. Merchant, M.E., *Mechanics of the metal cutting process. I. Orthogonal cutting and a type 2 chip*. Journal of applied physics, 1945. **16**(5): p. 267-275.

50. Wan, M., Y.-T. Wang, W.-H. Zhang, Y. Yang, and J.-W. Dang, *Prediction of chatter stability for multiple-delay milling system under different cutting force models*. International Journal of Machine Tools and Manufacture, 2011. **51**(4): p. 281-295.
51. Annoni, M., G. Biella, L. Rebaioli, and Q. Semeraro, *Microcutting Force Prediction by Means of a Slip-line Field Force Model*. Procedia CIRP, 2013. **8**: p. 558-563.
52. Toropov, A. and S.-L. Ko, *Prediction of shear angle for continuous orthogonal cutting using thermo-mechanical constants of work material and cutting conditions*. Journal of materials processing technology, 2007. **182**(1): p. 167-173.
53. Günay, M., I. Korkut, E. Aslan, and U. Şeker, *Experimental investigation of the effect of cutting tool rake angle on main cutting force*. Journal of materials processing technology, 2005. **166**(1): p. 44-49.
54. Sikder, S. and H. Kishawy, *Analytical model for force prediction when machining metal matrix composite*. International Journal of Mechanical Sciences, 2012. **59**(1): p. 95-103.
55. Komanduri, R. and Z.B. Hou, *Thermal modeling of the metal cutting process: part I—temperature rise distribution due to shear plane heat source*. International Journal of Mechanical Sciences, 2000. **42**(9): p. 1715-1752.
56. Komanduri, R. and Z.B. Hou, *Thermal modeling of the metal cutting process—Part II: temperature rise distribution due to frictional heat source at the tool–chip interface*. International Journal of Mechanical Sciences, 2001. **43**(1): p. 57-88.
57. Karpas, Y. and T. Özel, *Predictive analytical and thermal modeling of orthogonal cutting process—part I: predictions of tool forces, stresses, and temperature distributions*. Journal of manufacturing science and engineering, 2006. **128**(2): p. 435-444.
58. Boothroyd, G. and ey, *Temperatures in orthogonal metal cutting*. Proceedings of the Institution of Mechanical Engineers, 1963. **177**(1): p. 789-810.
59. Jaspers, S., *Temperature in orthogonal metal cutting*. 1996.
60. da Silva, M.B. and J. Wallbank, *Cutting temperature: prediction and measurement methods—a review*. Journal of materials processing technology, 1999. **88**(1): p. 195-202.
61. Cotterell, M., E. Ares, J. Yanes, F. López, P. Hernandez, and G. Peláez, *Temperature and Strain Measurement during Chip Formation in Orthogonal Cutting Conditions Applied to Ti-6Al-4V*. Procedia Engineering, 2013. **63**: p. 922-930.

62. *Turning view*. Available from: <http://www.directindustry.com>.
63. DeVries, W.R., *Analysis of material removal processes*. 1991: Springer Science & Business Media.
64. Armarego, E., *Material Removal Processes: An Intermediate Course*. 1994: Uni. of Melbourne, Department of Mechanical and Manufacturing Engineering, Manufacturing Science Group.
65. Radulescu, R. and S. Kapoor, *An analytical model for prediction of tool temperature fields during continuous and interrupted cutting*. Journal of Manufacturing Science and Engineering, 1994. **116**(2): p. 135-143.
66. Lazard, M. and P. Corvisier, *Modelling of a tool during turning: Analytical prediction of the temperature and of the heat flux at the tool's tip*. Applied thermal engineering, 2004. **24**(5): p. 839-849.
67. Shihab, S.K., Z.A. Khan, A. Mohammad, and A.N. Siddiqueed, *RSM based Study of Cutting Temperature During Hard Turning with Multilayer Coated Carbide Insert*. Procedia Materials Science, 2014. **6**: p. 1233-1242.
68. *Kennametal Machining Products Specifications-*. Available from: <http://www.kennametal.com/en/products/>.
69. *McMaster-Carr Co.* . Available from: <http://www.mcmaster.com/> - standard-aluminum-rods.
70. Brar, N., V. Joshi, and B. Harris. *CONSTITUTIVE MODEL CONSTANTS FOR Al7075-T651 and Al7075-T6*. in *SHOCK COMPRESSION OF CONDENSED MATTER 2009: Proceedings of the American Physical Society Topical Group on Shock Compression of Condensed Matter*. 2009. AIP Publishing.
71. *DEFORM 3D Help* S.F.T. Corp., Editor.
72. Kocks, U.F., C.N. Tomé, and H.-R. Wenk, *Texture and anisotropy: preferred orientations in polycrystals and their effect on materials properties*. 2000: Cambridge university press.
73. Randle, V. and O. Engler, *Introduction to texture analysis: microtexture, microtexture and orientation mapping*. 2000: CRC Press.
74. Nye, J.F., *Physical properties of crystals*. 1985: Clarendon press.
75. Choudhuri, D. and Y. Gupta, *Shock compression of aluminum single crystals to 70 GPa: Role of crystalline anisotropy*. Journal of Applied Physics, 2013. **114**(15): p. 153504.
76. AluMatter. Available from: aluminum.matter.org.uk.

77. Hosford, W.F., *The anisotropy of aluminum and aluminum alloys*. JOM, 2006. **58**(5): p. 70-74.
78. Schwartz, A.J., M. Kumar, B.L. Adams, and D.P. Field, *Electron backscatter diffraction in materials science*. 2009: Springer.
79. Bunge, H.J. and P.R. Morris, *Texture analysis in materials science: mathematical methods*. 1982: Butterworths London.
80. Corp., H.P.; Available from: <http://www.hindawi.com>.
81. Ramesh Narayanan, P., S. Suwas, K. Sreekumar, P.P. Sinha, and S. Ranganathan. *Evolution of Crystallographic Texture in Cold Rolled Al-Zn-Mg Alloys Used in Space Applications*. in *Materials Science Forum*. 2012. Trans Tech Publ.
82. *Applied Mechanics of Solids*. Available from: <http://www.solidmechanics.org>.
83. Rollett, A.D.; Available from: <http://rollett.org/anthony/>.
84. Hansen, J., J. Pospiech, and K. Lücke, *Tables for texture analysis of cubic crystals*. 1978: Springer.
85. Van Houtte, P., *Simulation of the rolling and shear texture of brass by the Taylor theory adapted for mechanical twinning*. Acta Metallurgica, 1978. **26**(4): p. 591-604.
86. Pospiech, J. and K. Lücke, *The rolling textures of copper and α -brasses discussed in terms of the orientation distribution function*. Acta Metallurgica, 1975. **23**(8): p. 997-1007.
87. Hirsch, J. and K. Lücke, *Overview no. 76: Mechanism of deformation and development of rolling textures in polycrystalline fcc metals—I. Description of rolling texture development in homogeneous CuZn alloys*. Acta Metallurgica, 1988. **36**(11): p. 2863-2882.
88. Kallend, J., U. Kocks, A. Rollett, and H.-R. Wenk, *Operational texture analysis*. Materials Science and Engineering: A, 1991. **132**: p. 1-11.
89. Bronkhorst, C., S. Kalidindi, and L. Anand, *Polycrystalline plasticity and the evolution of crystallographic texture in FCC metals*. Philosophical Transactions of the Royal Society of London. Series A: Physical and Engineering Sciences, 1992. **341**(1662): p. 443-477.
90. Barlat, F., R. Becker, Y. Hayashida, Y. Maeda, M. Yanagawa, K. Chung, J. Brem, D. Lege, K. Matsui, and S. Murtha, *Yielding description for solution strengthened aluminum alloys*. International Journal of Plasticity, 1997. **13**(4): p. 385-401.

91. Barlat, F., Y. Maeda, K. Chung, M. Yanagawa, J. Brem, Y. Hayashida, D. Lege, K. Matsui, S. Murtha, and S. Hattori, *Yield function development for aluminum alloy sheets*. Journal of the Mechanics and Physics of Solids, 1997. **45**(11): p. 1727-1763.
92. Burgers, J.M., *Some considerations on the fields of stress connected with dislocations in a regular crystal lattice. I.* 1939: Koninklijke Nederlandse Akademie van Wetenschappen.
93. Huang, S., *Continuum theory of plasticity*. 1995: John Wiley & Sons.
94. Schmid, E. and W. Boas, *Plasticity of crystals*. 1950.
95. Sachs, G., *Plasticity problems in metals*. Trans. Faraday Soc., 1928. **24**: p. 84-92.
96. Taylor, G.I., *Analysis of plastic strain in a cubic crystal*. Stephen Timoshenko 60th Anniversary Volume, 1938: p. 218-224.
97. Kröner, E., *On the plastic deformation of polycrystals*. Acta Metall, 1961. **9**: p. 155-161.
98. Molinari, A., S. Ahzi, and R. Kouddane, *On the self-consistent modeling of elastic-plastic behavior of polycrystals*. Mechanics of materials, 1997. **26**(1): p. 43-62.
99. Molinari, A., G. Canova, and S. Ahzi, *A self consistent approach of the large deformation polycrystal viscoplasticity*. Acta Metallurgica, 1987. **35**(12): p. 2983-2994.
100. Hill, R., *The Mathematical Theory of Plasticity*. 1950, Oxford Univ. Press, Oxford.
101. Bishop, J. and R. Hill, *CXXVIII. A theoretical derivation of the plastic properties of a polycrystalline face-centred metal*. The London, Edinburgh, and Dublin Philosophical Magazine and Journal of Science, 1951. **42**(334): p. 1298-1307.
102. Eshelby, J.D., *The determination of the elastic field of an ellipsoidal inclusion, and related problems*. Proceedings of the Royal Society of London. Series A. Mathematical and Physical Sciences, 1957. **241**(1226): p. 376-396.
103. Hutchinson, J.W., *Elastic-plastic behaviour of polycrystalline metals and composites*. Proceedings of the Royal Society of London. A. Mathematical and Physical Sciences, 1970. **319**(1537): p. 247-272.
104. Mura, T., *Micro-mechanics of Defects in Solids*. Vol. 3. 1987: Springer.
105. Lebensohn, R. and C. Tomé, *A self-consistent anisotropic approach for the simulation of plastic deformation and texture development of polycrystals*:

- application to zirconium alloys*. Acta Metallurgica et Materialia, 1993. **41**(9): p. 2611-2624.
106. Lin, S., H. Garmestani, and B. Adams, *The evolution of probability functions in an inelastically deforming two-phase medium*. International journal of solids and structures, 2000. **37**(3): p. 423-434.
 107. Garmestani, H., S. Lin, B.L. Adams, and S. Ahzi, *Statistical continuum theory for large plastic deformation of polycrystalline materials*. Journal of the Mechanics and Physics of Solids, 2001. **49**(3): p. 589-607.
 108. Voce, E., *A practical strain-hardening function*. Metallurgia, 1955. **51**(307): p. 219-226.
 109. Gilman, J.J., *Dislocation sources in crystals*. Journal of Applied Physics, 1959. **30**(10): p. 1584-1594.
 110. Embury, J. and R. Nicholson, *Dislocation sources in an aluminium alloy*. Acta metallurgica, 1963. **11**(5): p. 347-354.
 111. Kolmogorov, A.N., *On the statistical theory of the crystallization of metals*. Bull. Acad. Sci. USSR, Math. Ser, 1937. **1**: p. 355-359.
 112. Johnson, W.A. and R.F. Mehl, *Reaction kinetics in processes of nucleation and growth*. Trans. Metall. Soc. A.I.M.E, 1939. **135**(8): p. 396-415.
 113. Avrami, M., *Kinetics of phase change. I General theory*. The Journal of Chemical Physics, 1939. **7**(12): p. 1103-1112.
 114. Jonas, J.J., X. Quelenec, L. Jiang, and É. Martin, *The Avrami kinetics of dynamic recrystallization*. Acta Materialia, 2009. **57**(9): p. 2748-2756.
 115. Roberts, W., H. Boden, and B. Ahlblom, *Dynamic recrystallization kinetics*. Metal Science, 1979. **13**(3-4): p. 195-205.
 116. Deschamps, A. and Y. Brechet, *Influence of predeformation and ageing of an Al–Zn–Mg alloy—II. Modeling of precipitation kinetics and yield stress*. Acta Materialia, 1998. **47**(1): p. 293-305.
 117. Hines, J. and K. Vecchio, *Recrystallization kinetics within adiabatic shear bands*. Acta materialia, 1997. **45**(2): p. 635-649.
 118. Zener, C. and J. Hollomon, *Effect of strain rate upon plastic flow of steel*. Journal of Applied physics, 1944. **15**(1): p. 22-32.
 119. Gholinia, A., F. Humphreys, and P. Prangnell, *Production of ultra-fine grain microstructures in Al–Mg alloys by coventional rolling*. Acta materialia, 2002. **50**(18): p. 4461-4476.

120. Medina, S.F. and C.A. Hernandez, *Modelling of the dynamic recrystallization of austenite in low alloy and microalloyed steels*. Acta materialia, 1996. **44**(1): p. 165-171.
121. Kugler, G. and R. Turk, *Modeling the dynamic recrystallization under multi-stage hot deformation*. Acta Materialia, 2004. **52**(15): p. 4659-4668.
122. Yeom, J.T., C.S. Lee, J.H. Kim, and N.-K. Park, *Finite-element analysis of microstructure evolution in the cogging of an Alloy 718 ingot*. Materials Science and Engineering: A, 2007. **449**: p. 722-726.
123. Bolouri, A., M. Shahmiri, and C.G. Kang, *Coarsening of equiaxed microstructure in the semisolid state of aluminum 7075 alloy through SIMA processing*. Journal of Materials Science, 2012. **47**(8): p. 3544-3553.
124. Asgharzadeh, H. and H. McQueen, *Grain growth and stabilisation of nanostructured aluminium at high temperatures: review*. Materials Science and Technology, 2014.
125. Adams, B.L., A. Henrie, B. Henrie, M. Lyon, S. Kalidindi, and H. Garmestani, *Microstructure-sensitive design of a compliant beam*. Journal of the Mechanics and Physics of Solids, 2001. **49**(8): p. 1639-1663.
126. Adams, B.L., M. Lyon, B. Henrie, S.R. Kalidindi, and H. Garmestani. *Spectral integration of microstructure and design*. in *Materials Science Forum*. 2002. Trans Tech Publ.
127. Adams, B.L., S.R. Kalidindi, and D.T. Fullwood, *Microstructure sensitive design for performance optimization*. 2012: Butterworth-Heinemann.
128. Bouhattate, J., D. Li, H. Garmestani, S. Ahzi, and M. Khaleel, *On Improving Predictions of Texture Evolution Using Processing Path Model*. Materialwissenschaft und Werkstofftechnik, 2005. **36**(10): p. 538-540.
129. Li, D., H. Garmestani, and S. Ahzi, *Processing path optimization to achieve desired texture in polycrystalline materials*. Acta materialia, 2007. **55**(2): p. 647-654.
130. Clement, A., *Prediction of deformation texture using a physical principle of conservatiol*. Materials Science and Engineering, 1982. **55**(2): p. 203-210.
131. Ahmadi, S., B. Adams, and D. Fullwood, *An Eulerian-Based Formulation for Studying the Evolution of the Microstructure under Plastic Deformations*. Computers, Materials, & Continua, 2010. **14**(2): p. 141-170.
132. Hall, E., *The deformation and ageing of mild steel: III discussion of results*. Proceedings of the Physical Society. Section B, 1951. **64**(9): p. 747.

133. Petch, N., *The cleavage strength of polycrystals*. J. Iron Steel Inst., 1953. **174**: p. 25-28.
134. Lehto, P., H. Remes, T. Saukkonen, H. Hänninen, and J. Romanoff, *Influence of grain size distribution on the Hall–Petch relationship of welded structural steel*. Materials Science and Engineering: A, 2014. **592**: p. 28-39.
135. Hansen, N., *Hall–Petch relation and boundary strengthening*. Scripta Materialia, 2004. **51**(8): p. 801-806.
136. Malygin, G., *Breakdown of the Hall-Petch law in micro-and nanocrystalline materials*. Physics of the Solid State, 1995. **37**: p. 1248-1253.
137. Zhang, S., W. Hu, R. Berghammer, and G. Gottstein, *Microstructure evolution and deformation behavior of ultrafine-grained Al–Zn–Mg alloys with fine η' precipitates*. Acta Materialia, 2010. **58**(20): p. 6695-6705.
138. Tabei, S., A. Sheidaei, M. Baniassadi, F. Pourboghrat, and H. Garmestani, *Microstructure Reconstruction and Homogenization of Porous Ni-YSZ Composites for Temperature Dependent Properties*. Journal of Power Sources, 2013.
139. Bao, G., *Damage due to fracture of brittle reinforcements in a ductile matrix*. Acta metallurgica et materialia, 1992. **40**(10): p. 2547-2555.
140. Finot, M., Y. Shen, A. Needleman, and S. Suresh, *Micromechanical modeling of reinforcement fracture in particle-reinforced metal-matrix composites*. Metallurgical and Materials Transactions A, 1994. **25**(11): p. 2403-2420.
141. Wallin, K., T. Saario, and K. Törrönen, *Fracture of brittle particles in a ductile matrix*. International journal of fracture, 1986. **32**(3): p. 201-209.
142. Gv Boittin, D.L., A. Rafrayl, P. Caron, P. Kanoutél, F. Gallerneaul, and G. CailletaudZ, *INFLUENCE OF Y'PRECIPITATE SIZE AND DISTRIBUTION ON LCF BEHAVIOR OF A PM DISK SUPERALLOY*. Superalloys 2012, 2012: p. 167.
143. Glazer, J. and J.W. Morris, *The effect of the precipitate size distribution on the aging curve of order hardening alloys*. Acta Metallurgica, 1988. **36**(4): p. 907-915.
144. El-Magd, E. and M. Brodmann, *Influence of precipitates on ductile fracture of aluminium alloy AA7075 at high strain rates*. Materials Science and Engineering: A, 2001. **307**(1): p. 143-150.
145. Ghosh, S. and S. Moorthy, *Particle fracture simulation in non-uniform microstructures of metal-matrix composites*. Acta Materialia, 1998. **46**(3): p. 965-982.

146. Moorthy, S. and S. Ghosh, *A Voronoi cell finite element model for particle cracking in elastic-plastic composite materials*. Computer methods in applied mechanics and engineering, 1998. **151**(3): p. 377-400.
147. Ghosh, S. and S. Moorthy, *Three dimensional Voronoi cell finite element model for microstructures with ellipsoidal heterogeneties*. Computational Mechanics, 2004. **34**(6): p. 510-531.
148. Jeffery, G.B., *The motion of ellipsoidal particles immersed in a viscous fluid*. Proceedings of the Royal Society of London. Series A, Containing Papers of a Mathematical and Physical Character, 1922. **102**(715): p. 161-179.
149. Oberbeck, A., *Ueber stationäre Flüssigkeitsbewegungen mit Berücksichtigung der inneren Reibung*. Journal für die reine und angewandte Mathematik, 1876. **81**: p. 62-80.
150. Lamb, H., *Hydrodynamics*. 1993: Cambridge University Press.
151. Byerly, W.E., *An Elemenatary Treatise on Fourier's Series, and Spherical, Cylindrical, and Ellipsoidal Harmonics, with Applications to Problems in Mathematical Physics*. 1959: Dover Publicatiions.
152. Kellogg, O.D., *Foundations of potential theory*. 1929: DoverPublications. com.
153. Klein, P.P., *On the Ellipsoid and Plane Intersection Equation*. Applied Mathematics, 2012. **3**(11): p. 1634-1640.
154. Jaeger, J.C., *Elasticity, fracture and flow: with engineering and geological applications*. 1970: Barnes & Noble.
155. Lawn, B.R., *Fracture of brittle solids*. 1993: Cambridge university press.